Properties of materials at interfaces

Thesis Submitted for the Degree of

Doctor of Philosophy (Science)

In

Physics (Theoretical)

By

Edwine Tendong

Department of Physics
University of Calcutta

JULY 2022

To my daughter
Miriam

Acknowledgements

I would like to express my immense and sincere gratitude to my supervisors, Professor Tanusri Saha-Dasgupta and Professor Jaydeb Chakrabarti. I count myself extremely fortunate to have worked under the supervision of such giants. Their passion, immense knowledge, and patience have been critical for overcoming the difficulties I faced during this research. Professor Tanusri Saha-Dasgupta accepted my PhD application and offered me this unique opportunity to carry out my work at the S. N. Bose National Centre for Basic Sciences, and for this I remain highly indebted. I have learnt from them very invaluable science as well as life lessons which I will cherish always. I could not have imagined having better advisors. I thank the members of my PhD research committee, Professor Manoranjan Kumar and Professor Suman Chakrabarty, for their insightful comments throughout my past evaluations. My humble thanks to the reviewers who have taken time out to review this thesis. I am confident I will benefit immensely from the valuable comments.

I acknowledge financial support from The World Academy of Sciences (TWAS) and S. N. Bose National Centre for Basic Sciences, through the TWAS-BOSE PhD fellowship. My thanks to S. N. Bose National Centre of Basic Sciences for hosting me and providing me with a very comfortable stay throughout my Ph.D.

My humble gratitude to the administration and staff of S.N. Bose National Center for Basic Sciences, for the timely issuance of all official papers that I needed. My special thanks to Mme Nibedita Konar for always going out of her way to help me with various complicated visa procedures. My special thanks to the S.N. Bose Centre support personnel, whose wonderful assistance and smiles have made my stay a memorable one. I remain forever in your debt.

My immense thanks to my seniors, Dr Dhani Nafday, Dr Hrishit Banerjee, Dr Anita Halder, Dr Piya Manas, Dr Sutapa Dutta, and Dr Uttam Pal, for helping me take my first steps in molecular simulations and for the many stimulating discussions. The course of my Ph.D has been marked by many extreme events, including a worldwide pandemic and two major surgical interventions. I could not have survived these without the immense love and support from my fellow graduate students and group members: Sasthi Charan Mandal, Abhik Ghosh Moulick, Rahul Karmakar, Anirban Paul, Suravi Pal, Kanika

Kole, Avik Sasmal, Shreya Das, Shiladitya Karmakar, Samir Rom, Aishwaryo Ghosh, Rajdeep Biswas, Kushik Pradhan, and Manoj Gupta. The support and friendship of each one of you will remain in my heart. I heartily wish all the best.

My time at S. N. Bose National Centre for Basic Sciences has been made memorable by a great circle of friends who have shared in my daily ups and downs. I'd like to thank Dr Sk Imadul Islam in particular, who has been an invaluable friend since my first day at the S.N. Bose National Centre for Basic Sciences. Thanks for taking the time to show me different wonderful sites around West Bengal and for introducing me to your wonderful family. Thanks to fellow TWAS-BOSE scholar Dr. Md. Sarowar Hossain for invaluable advice. Thanks to the wonderful members of the S.N. Bose football club, with whom I shared many exciting games. Thank you to my friends Parushottam Majhi, Ruchi Pandey, Saikat Pal, Didhitti Bhattacharya, Vishal Agarwal and Anupam Goria, for being a part of this wonderful journey. A special thank you to my fellow AIMS and TWAS-Bose PhD fellow, Gesesew Reta. You have been a great shoulder to lean on and I am immensely grateful.

To my mother Azicha Getrude Tendong, and father, Menjua Francis Asaba; receive my deepest gratitude and love for the prayers, care, love, sacrifices and dedications for educating and preparing me for my future. Special thanks to my siblings; your encouragement always hits me when I need it most.

Finally, and most importantly to my beloved wife, Nkengateh Jorceline Tendong (DDS), there is not a word, strong enough to describe how honoured and proud I am. Your support, encouragement, quiet patience, and unwavering love have been undeniably the bedrock upon which the past five years of my life have been built. I know how difficult it was to take care of our daughter, Azicha Miriam Tendong, in my absence. I remain forever grateful. I thank God almighty for putting you in my life, for guiding our journey this far, for all that has been and for all that will be.

Edwine Tendong
Kolkata, India
July 2022

Abstract

In the present thesis, motivated by recent advances in the fabrication of nanoscale heterostructures with atomically sharp interfaces, we explore microscopic interactions at two kinds of nano interfaces, namely: interfaces between nanoconfined fluids and the confining surfaces, and interfaces between colloidal nanoparticles and ligands in presence of different solvents. Understanding microscopic interactions is key to manipulating these nanoscale systems for novel applications.

Our first study, employs grand canonical Monte-Carlo and molecular dynamics simulations to investigate the phase behavior and viscoelastic properties of a simple liquid asymmetrically confined by two structureless walls. Confinement asymmetry drives a rich phase behavior and a two regime viscoelastic response which is found to be universal for strongly confined fluids. The fluid exhibits a gel-like mechanical response vicinity of the ordering transition, before elastic behavior becomes dominant.

In our second investigation, we examine the dynamics of of water nanoconfined between a metal-oxide surface and a graphene layer, using molecular dynamics simulations. We find that the confined water exhibits heterogeneous dynamics, due competing interactions at the hydrophobic graphene and the hydrophilic metal oxide surface. Guest molecules in the channel show enhanced diffusion driven by the dynamics heterogeneity of the confined water. The observed behavior is shown to be valid for any hydrophobic-hydrophilic nanoslit, with implications for design of implantable nanodevices for drug delivery.

In our third investigation, molecular dynamics simulations assisted by inputs from density functional theory, are used to probe microscopic interactions between lead-halide perovskite nanoparticles, and organic surface ligands in the presence of different solvents. We observe that ligands show surface specificity in adsorption at the nanoparticle interface. This leads to anisotropic interactions between nanoparticles which may assist in directed self-assembly.

Our computational results are expected to provide understanding of microscopic interactions in asymmetrically nanoconfined fluids as well as colloidal nanoparticle suspensions. This will serve as a useful guide for applications ranging from fluid transport in van der Waal heterostructures, to self-assembly of nanoparticles.

Contents

List of Publications

1. Dynamics of water trapped in transition metal oxide-graphene nano-confinement. Edwine Tendong, Tanusri-Saha Dasgupta and Jaydeb Chakrabarti. Journal of Physics: Condensed Matter 32.32 (2020): 325101.

2. Viscoelastic response of fluid trapped between two dissimilar van der Waals surfaces. Edwine Tendong, Tanusri-Saha Dasgupta and Jaydeb Chakrabarti. Journal of Physics: Condensed Matter 34.19 (2022): 195101.

3. Solvent polarity effects on ligand adsorption and interaction of colloidal CsPbBr3 nano-particles. Edwine Tendong, Avik Sasmal, Tanusri-Saha Dasgupta and Jaydeb Chakrabarti. (Manuscript in preparation)

List of Figures

List of Tables

Chapter 1 Introduction

Over the past few decades the ability to synthesize and manipulate materials whose dimensions along one or more spatial directions are of the order of a few nanometers, has witnessed incredible progress [1]. It has now become possible to fabricate systems with atomically sharp interfaces [2] such as van der Waals heterostructures obtained by stacking two-dimensional (2-D) material layers on other 2-D materials or on bulk substrates. These materials offer unprecedented possibilities for novel mechanical, electrical, chemical and rheological applications. The synthesis of nano size particles and their self-assembly into one-dimesional (1-D) and 2-D super-lattices with enhanced optoelectronic properties, has also been achieved [3]. In designing new applications with such nano materials, interfaces inevitably occur, and play a central role in determining properties of the composite systems. The overarching importance of interfaces emerges from the fact that such 1-D or 2-D nano-materials are characterized by a large surface-area to volume ratio. This makes the majority of atoms to lie at the interface being subject to forces and interactions which are absent in the bulk. Understanding molecular level interactions at nano-material interfaces, remains a major step towards realizing various applications.

1.1 What are interfaces?

Interfaces are the boundaries between different materials in contact, or between different phases of matter. A phase of a material is characterized by a uniform chemical composition and physical state. In reality, every material terminates at an interface since every single phase is in contact with another phase. Interfaces can involve similar phases such as solid–solid and liquid–liquid interfaces or dissimilar phases such as solid–liquid and solid–gas interfaces, etc. The term surface is sometimes used in place of interface, when the boundary formed involves a gas or vacuum. Interfaces can be sharp when there is a clear boundary dividing two phases, or diffuse when one phase morphs continuously into another. The interfacial layer is usually considered to be the top most atomic layer for solids, or for the case of liquids it can be a film of a few angstroms to several nanometers thick in contact with another phase.

Among various types of interfaces, fluid-solid interfaces have received significant research attention [4, 5], owing to the wide range of interesting physical phenomena that take place at these interfaces, such as wetting, adhesion surface tension, capillary action, slippage [6, 7, 8], to name only a few. Fluid–solid interfaces are ubiquitous in nano-systems, for example when fluids are confined in nano-size gaps in van der Waal heterostructures [4, 5], or when colloidal nanoparticles are suspended in solvent. Theoretical modeling approaches such as molecular dynamics simulations offer the possibility of probing the properties of such interfaces with atomically sharp resolutions. Nano-confined fluids exhibiting unique properties at fluid-surface interfaces, and colloidal nanoparticles ligand - solvent interfaces form the central theme of this thesis.

1.2 Interfaces in nanomaterials

1.2.1 Nanoconfined fluid - confining wall interfaces

Interfaces created by fluids confined in nano-size gaps between solid surfaces such as nano-pores and slits in van der Waals heterostructures, have attracted significant research interest owing to their possible applications in diverse domains including nano filtration [9, 10, 11, 12], energy storage [13, 14], drug delivery [15, 16, 17] and nanofluidic applications [18]. Nanoconfined fluids exhibit properties that are distinct from those of their bulk counterparts [19, 20]. At the interface, competing fluid-surface and fluid-fluid interactions significantly alter molecular configuration and correlations in the confined fluid. This results in new properties and phenomena such as freezing above bulk melting point [21], hexatic phases [22], phase coexistence [23], anomalous dynamics [17], and viscoelasticity [24].

Fluids under nano-confinement by two identical solid walls, such as between two graphene sheets or silica nano-slits, have been widely studied both theoretically and experimentally. For example, the structure of water confined by two identical graphene layers, has been studied using transmission electron microscopy and molecular dynamics simulations [25]. As a representative case, Figure 1.1(a) and (b) show respectively, transmission electron microscopy image and MD simulation snapshot of graphene confined monolayer water. Water is observed to form a highly ordered square ice-like monolayer even at ambient conditions. It has been shown that formation of such ordered water layer is independent of the atomic structure of the confining surfaces [25]. Neutron diffraction [26], high-resolution in situ x-ray studies [27] and atomic force microscopy experiments [28] have also been employed in probing fluid structure under symmetric confinement, revealing that fluids adopt a layered structure

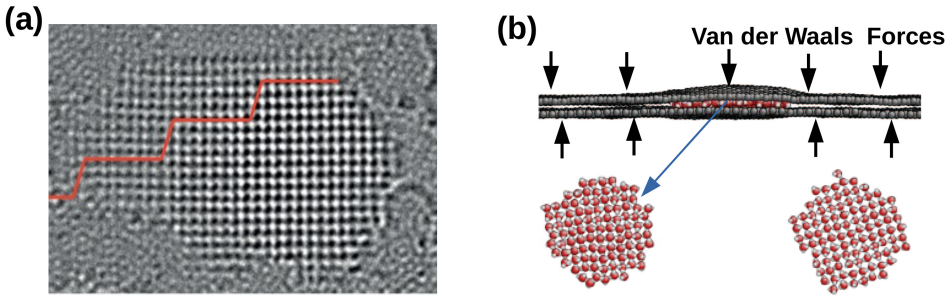

Figure 1.1: (a) Transmission Electron Micrograph showing square ice-like ordering of water trapped between two graphene sheets. (b) Molecular dynamics simulation snapshot of monolayer water confined by two graphene sheets. The sheets are pushed together by van der Waals attractive forces. Similar square ice like ordering is observed in the confined water layer. (Figure adapted from [25])

close to the confining surfaces, as well as lateral ordering within the fluid layers, with triangular or square symmetry depending on the size of the confinement and the strength of wall-fluid interactions. At the contact layer of confined fluid and solvophobic surface, a depletion zone with no fluid, has been reported [29, 30], while a strongly adsorbed ordered fluid layer has been observed for solvophilic confinement [31, 32, 33]. Capillary flow [34, 35] and isotope labeling experiments [36] have reported ultra-fast flow rates and viscosity lower than the bulk value, for water in hydrophobic nano channels such as carbon nanotubes, meanwhile, significant increase in viscosity and decrease in the diffusion constant have been reported for water confined between two hydrophilic surfaces [37, 38].

The experimental results on the behavior of fluids under nano-confinement by two identical walls, have been complemented by numerous molecular simulation and theoretical studies. Molecular simulations offer unique advantages for studying such systems, as they probe microscopic interactions with a resolution not yet attainable by current experimental approaches. Simulations have shown that fast transport of water through hydrophobic nano channels can be attributed to ordering and curvature-dependent interfacial friction of water in carbon nanotubes [39]. The slowdown in dynamics and ordering of water in hydrophilic confinement has been attributed to formation of strong hydrogen bonds between

water molecules and cations at the confining surfaces [40]. Likewise simulations have shown that viscosity and other transport properties of fluids under nano confinement by identical walls, depend strongly on the micro-structure of the fluid, size of confinement as well as the strength of the interaction of the fluid with the confining surfaces[41].

The scenario becomes more interesting when the confining surfaces are dissimilar, resulting in wall-fluid interactions which are different at each boundary. Such confinements are envisaged in heterostructure devices [42] such as graphene – $SrTiO_3$ (STO) heterostructures which have been considered for various electronic applications [43, 44]. Unlike symmetric channels [35, 45, 37, 38, 46], the unequal interaction strengths of confining walls with the fluid, result in competing wetting-dewetting tendencies which modify phase behavior [47] and transport properties [48]. Detailed knowledge of the microscopic behavior of fluids under such scenario is important for various applications such as liquid phase exfoliation [49], water treatment [50] and energy production [51]. The structure and dynamics of fluids at nano interfaces formed by materials with dissimilar wetability remains largely unexplored. In the present thesis we intend to venture into this unexplored area.

1.2.2 Nanoparticle - ligand - solvent interfaces

Equally important are microscopic interactions at the interface of colloidal nanoparticle dispersions. Competing interactions between passivating ligands and solvent as well as ligand-ligand interactions at nanoparticle surface can lead to aggregation and formation of ordered superlatices via self-assembly, with the nanoparticle building blocks inter-linked not by covalent bonds, but through weak forces such as van der Waals attraction, hydrogen bonds or hard-particle excluded volume interactions [52]. Nanoparticle self-assembly provides a rapid

and scalable route towards realization of complex and robust materials with nanometre precision [3]. It has recently been applied in synthesis of a wide variety materials ranging from periodic mesoporous silicas, to nano-plates and nanowires [53, 54, 55].

Self-assembly of colloidal nanoparticles involves an interplay of a wide range of factors including nanoparticle shape, size, dipole moments, ligands, solvent, external electric and magnetic fields etc, with surface ligands playing a central role [56, 57]. Ligands provide an effective means of manipulating forces between nanoparticles and dictating inter-particle distances, all of which are key parameters governing superlattice properties [58]. It has been shown that surface ligands can influence the shape of nanostructures formed [59]. However precise manipulation of ligands to dictate the details of nanoparticle self-assembly has remained challenging [60].

Experimentally, self-assembly has been observed in a wide variety of nanoparticle systems including gold nanoparticles [61, 62, 63], hybrid organic [64, 65] and inorganic perovskites [66], and colloidal nanocrystals of rare earth metals [56], to name only a few. In particular, ligand-covered lead-halide perovskite nanoparticles with general formula $CsPbX_3$, X = (Br, Cl,I), have been widely investigated owing to their unique photovoltaic properties and ability to self-aggregation into different super-lattices [67, 68].

It has been observed that by manipulating the ratio of oleylamine to oleic acid ligands as shown in Figure 1.2, the synthesis of $CsPbX_3$ nanocubes to nanorods to nanowires [69] can be realized. Using short chain acid and long chain amine ligands, the formation of nanocubes is observed, while a combination of short chain amine and long chain acid ligands results in the formation of nanoplates [70]. It has been shown that polar solvents act on $CsPbX_3$ nanoparticles through the ligands, partially or completely removing the ligand coating of nanoparticles, causing them to coalesce and loose their photo-luminescent properties [71].

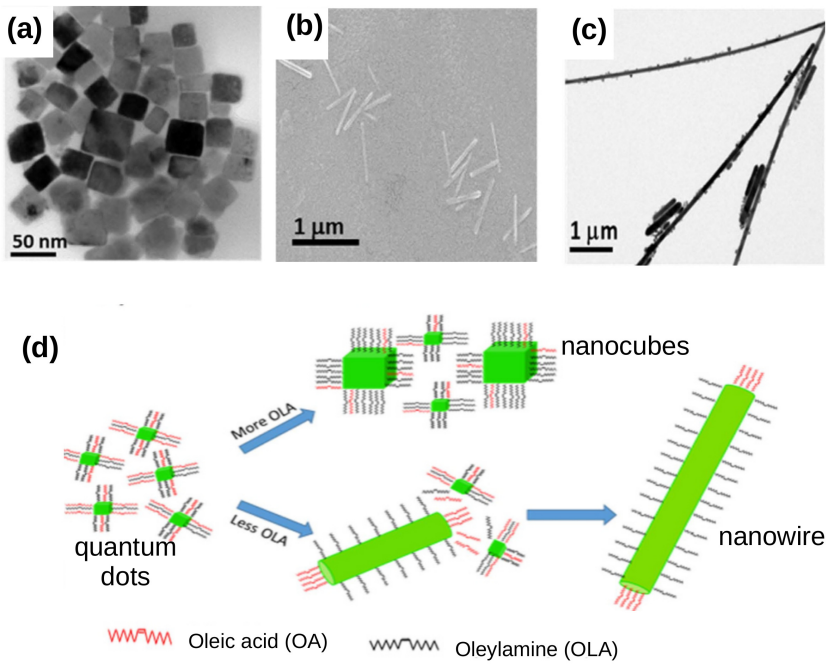

Figure 1.2: HR-TEM images of $CsPbBr_3$ (a) nanocubes, (b) nanorods and (c) nanowires, in formed in toluene solvent. (d) shows a schematic of a proposed mechanism of formation of formation of nanocubes and nanowires from $CsPbBr_3$ quantum dots (Figure adapted from [69])

Tuning of nanoparticle interactions to drive self-assembly into desired 1-D and 2-D superlattices, requires understanding microscopic details of surface, ligand and solvent interactions, as is attempted in this thesis.

1.3 Outline of the thesis

The goal of this thesis is to investigate the microscopic processes at the interfaces of two types of systems: (i) asymmetrically nano-confined fluids, and (ii) Colloidal lead-halide perovskite nanoparticle $CsPbX_3$, X = (Br, Cl,I) suspensions . We explore their structural properties, and dynamics. We discuss our findings and their implications within the context of various applications ranging from water purification and drug delivery to lubrication and nano-fabrication. The thesis is divided into six chapters as listed below:

- **Chapter 1** gives the background of the work carried out in this thesis as

well as an elaborate summary of the main findings.

- **Chapter 2** discusses the the methodology and molecular simulation techniques that we have employed in our investigations. In particular we discuss in detail the two classical simulation approaches, viz Grand Canonical Monte-Carlo (GCMC) and Molecular Dynamics (MD) simulations. We further discuss details of the statistical physics tools used in analysis of the output of our classical simulations. We briefly explore advanced sampling methods, specifically the metadynamics approach which is used in our work for obtaining free energy profiles. The chapter closes with discussion of the quantum mechanical Density Functional Theory which we use in the last part of our work for deriving the nanoparticle model.

- **Chapter 3** presents our finding on the structure, phase behavior and viscoelastic response of a simple liquid confined in slit-like geometry by two soft idealized walls where details of wall structure are not considered. The strength of interaction between the fluid and the confining walls as well as the wall separation are varied. We consider in particular the case of an asymmetric slit, when the interaction strength of fluid with one of the confining surfaces is greater than that with the second surface. The ratio of the strong(ε_S)/weak(ε_W) interaction strengths defines the channel asymmetry denoted by ξ. To vary ξ, we change ε_S, keeping ε_W fixed. We perform GCMC simulations to obtain the structure of fluid for different values of asymmetry and slit width. Using equilibrated configurations obtained from the GCMC simulations, we then carry out MD simulations to study the viscoelastic response. An outline of this investigation is shown in Figure 1.3.

  We find that for a given asymmetry ξ, the mean density of fluid shows an oscillatory behavior as the slit width increases. This is attributed to the com-

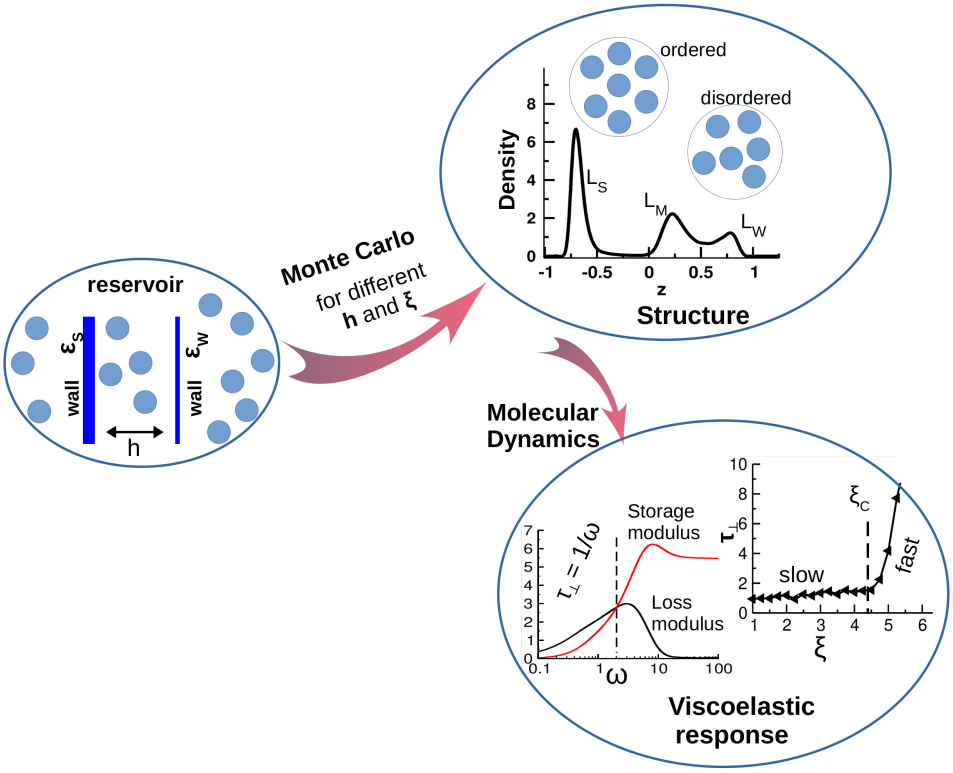

Figure 1.3: Outline of investigation of structure and viscoelastic response of asymmetrically confined fluid. Structural properties of the fluid are determined from GCMC simulations for different slit widths and asymmetry values. The viscoelastic response is obtained via MD simulations on equilibrated configurations from the GCMC.

mensurability of the slit to accommodate the fluid layers. The mean density is higher for commensurate slit widths compared to incommensurate ones. For a given slit width, as the asymmetry ξ is increased the density of fluid in the slit crosses over from a phase R with density rarer than the bulk density to a phase D with density grater than bulk density. The asymmetry value at which this crossover takes place is denoted by ξ_{RD}. It is observed that the fluid shows a layered structure along the confinement direction, with the fluid layers adjacent to the strongly attracting wall having higher density compared to the the fluid layer adjacent to the weakly attracting wall. As slit asymmetry increases the particles in each layer transition from fluid like disordered phase F to a solid-like phase S with long range bond orientational order. This $F \rightarrow S$ transition shows an intermediate

coexistence region having both ordered and disordered fluid patches in the layer, for slits with more than one fluid layer.

The dependence of viscoelastic relaxation time on ξ, for ξ values in the fluid-like region, is observed to show two distinct regimes, a slow changing and a fast changing regime. We denote by ξ_c the asymmetry value for which the dependence of the viscoelastic relaxation time changes. ξ_c is found to correspond with ξ_{RD}, indicating that the change in dependence of viscoelastic relaxation time on asymmetry, is driven by the $R \rightarrow D$ density crossover. By scaling asymmetry ξ with the value of ξ_c, the dependence of the viscoelastic relaxation time for different slits is observed to collapse unto a single curve, indicating that the two regime behavior is universal for all slit widths and independent of the slit size provided one stays in the strong confinement regime. We further show that in the slow changing regime, the viscoelastic response is driven by contributions from the fluid layers adjacent to the weakly interacting wall, while in the fast changing regime the viscoelastic response is dominated by contributions from the fluid layer adjacent to the strongly attracting wall. Finally in vicinity of the $F \rightarrow S$ transition the fluid is observed to show gel-like viscoelastic response just before elastic behavior becomes dominant in the solid-like phase.

The chapter concludes with a discussion of the implications of our findings for interpreting results of nano-rheological measurements for a variety of systems ranging from molecular fluids under strong confinement, to macromolecular dispersions in micrometer channels.

- **Chapter 4** explores the structure and dynamics of water confined between two atomically detailed walls, namely, a graphene layer and the TiO_2 terminated surface of $SrTiO_3$ (STO). The choice of confining surfaces is motivated by recent experiments probing graphene-STO interface dipoles [72] and the

photo catalytic water splitting properties [73] of the TiO_2 terminated STO surface. Graphene is hydrophobic while the TiO_2 terminated surface of STO is hydrophilic resulting in an asymmetric confinement. We examine the influence of competing hydrophobic and hydrophilic interactions on the structure and dynamics of water, and discuss some possible implications for the design of implantable drug delivery nano-devices.

We find that water, trapped between an oxide surface like TiO_2 surface of STO and a graphene cover gets strongly modified compared to bulk water. Density oscillations due to the confining walls extend up 1 nm away from each of the surfaces. For a slit of width 1 nm, the confined water molecules experience the effects of both surfaces and the density profile reveals a strongly adsorbed water layer L_S adjacent to the STO surface, a weakly adsorbed layer L_G adjacent to the graphene surface and an intervening middle layer L_M. Figure 1.4 shows snapshots of water adjacent to the STO and graphene surface from MD simulations. The layer L_S is observed to have square ice-like crystalite patches formed by pining of water molecules to the STO surface. Imprints of the square ice-like patches extend to the layer L_M, and both L_M and L_G also show in-homogeneous in-plane density.

Analysis of the dynamics of water molecules reveals ultra-slow dynamics and large residence times for water molecules in L_S and faster dynamics for L_M and L_G. Coupling of slow dynamics of hydrating water layer at the STO surface with faster moving over-layers introduces dynamic heterogeneity throughout the slit. This heterogeneity is evidenced in the profile free energy landscape experience by the water molecules in each layer.

We explore the implications of the heterogeneous water dynamics in asymmetric channels to design drug delivery devices by considering the diffusion of a bio-molecule namely oleic acid, through such an asymmetric slit.

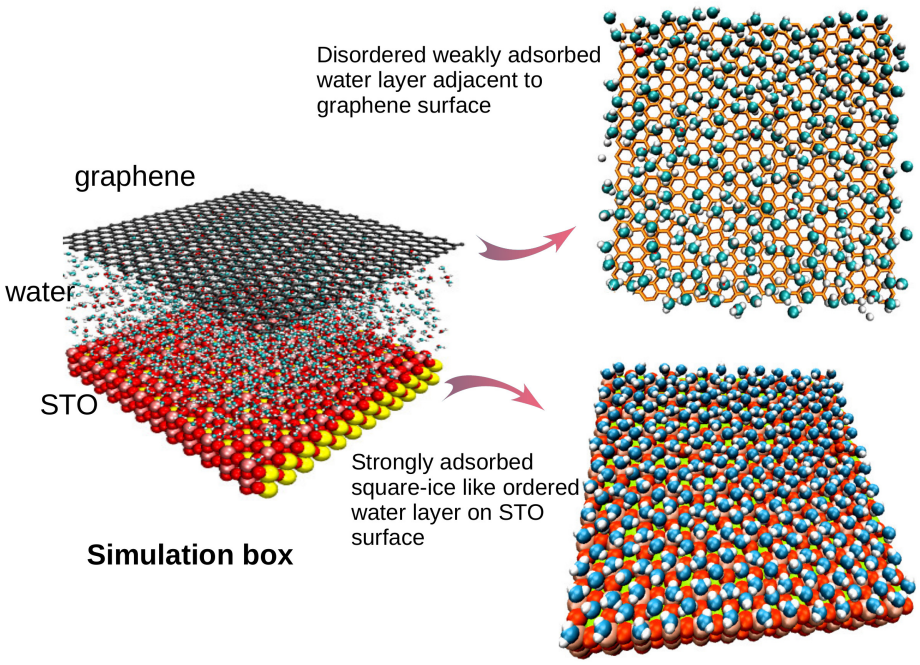

Figure 1.4: Snapshots of MD simulation box of water in graphene-STO confinement. Square ice-like water layer water is observed adjacent to STO surface and disordered water layer adjacent to graphene surface.

Our investigations show that in the asymmetric slit, the mean square displacement of oleic acid is orders of magnitude greater than its mean squares displacement in a symmetric slit. This increase in mobility can be exploited for faster drug release from implantable drug delivery devices.

- **Chapter 5** considers the microscopic interactions of organic ligands at nanoparticle surfaces in the presence of solvents with varying degrees of polarity. This is a step to understand how microscopic ligand interactions and adsorption at different nanoparticle facets may affect self-aggregation process of nanoparticles.

  Specifically we consider $CsPbBr_3$ nano particles owing to their well known ability to aggregate into different kinds of nano-structures such as nanorods, nanowires [54], and nanoplates [74], and their wide range of application in optoelectronic and photovoltaic devices such as LEDs, [75], solar cells,[76],

photo detectors and lasers.

We construct a nanoparticle model by cutting a 3×3×2 super-cell from an orthorhombic $CsPbBr_3$ bulk lattice. The resultant nanoparticle is terminated at a CsBr layer along the (001) direction and at a $PbBr_2$ layer along the $(00\bar{1})$ direction, with the rest of the facets having mixed $CsPbBr_2$ terminations. From quantum mechanical calculations of vacancy formation energies we find that the formation of Br vacancies is favorable, with the energy cost being comparable for all facets. We thus employ two nanoparticle models in our investigations; one having Br vacancies and another without Br vacancies. The nanoparticle surface is passivated with oleylamine and oleic acid ligands in equal ratio. Two combinations of protonation states of the ligands are considered; (i) oleic acid anions and neutral oleylamine and (ii) neutral oleic acid and oleylamine cations.

Figure 1.5 shows an outline of our investigations of ligand adsorption and dynamics in presence of different solvents, and its influence on nanoparticle interactions. Using extensive molecular dynamics simulations, we examine the adsorption of ligands at different facets of the nanoparticle in the presence of hexane, toluene, chloroform, ethanol and water as solvents. In hexane solvent it is observed that the largest fraction of ligand is adsorbed at the $PbBr_2$ terminated facet, followed by the CsBr facet and lowest for the facets with mixed termination, following the expectation of electrostatics. For solvents with higher polarity the overall amount of adsorbed ligand reduces with increasing solvent polarity. This decrease follows a power law with exponent close 1, and is attributed to increase in shielding of electrostatic interactions between ligands and the nanoparticle surface by the solvent. Preference of ligand for the $PbBr_2$ surface is maintained. In presence of water, all ligands are desorbed from the nanoparticle surface.

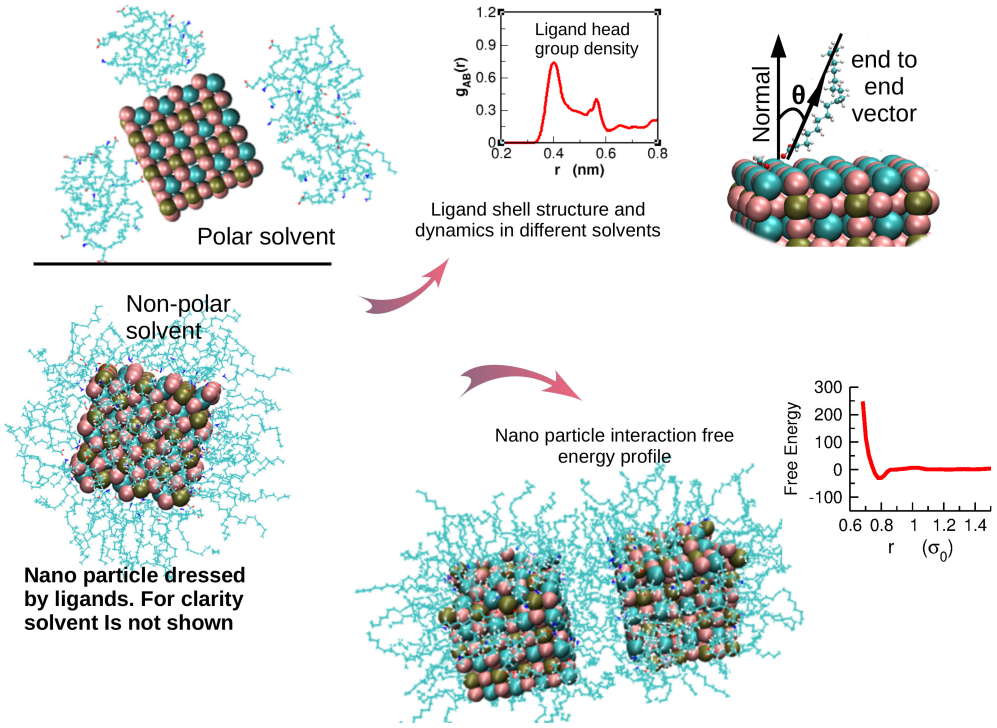

Figure 1.5: Outline of investigation of ligand adsorption and nanoparticle interaction in presence of different solvents. The structure and dynamics of the ligand shell are studied via MD simulations, and the interaction free energy between different facets of nanoparticle in different solvents is calculated using the metadynamics approach.

We further investigate the interaction between two nanoparticles in the presence of different solvents, by calculating the effective free energy profile, using the metadynamics approach. For simplicity we consider only the cases where the nanoparticle facets are facing each other, since experimental observations suggest that self-assembly occurs via facet attachment [77, 78]. We find that facets with higher amount of adsorbed ligand tend show attractive interactions at short separation, while facets with small amounts of adsorbed ligands show repulsive interactions. We show that the observed attractive interactions between nanoparticle facets are mainly mediated by ligand interdigitation. Finally we argue that the facets with attractive interactions can drive directed self-aggregation of the nanoparticles.

- **Chapter 6** presents an outlook of our work.

References

[1] J. Youtie, P. Shapira, A. L. Porter, *Journal of Nanoparticle Research* **10**, 981 (2008).

[2] L. Wu, *et al.*, *Nature Nanotechnology* **16**, 882 (2021).

[3] M. A. Boles, M. Engel, D. V. Talapin, *Chemical reviews* **116**, 11220 (2016).

[4] M.-P. Gaigeot, M. Sulpizi, *Journal of Physics: Condensed Matter* **24**, 120301 (2012).

[5] S. Lin, X. Chen, Z. L. Wang, *Chemical Reviews* (2021).

[6] A. Olanrewaju, M. Beaugrand, M. Yafia, D. Juncker, *Lab on a Chip* **18**, 2323 (2018).

[7] G. Tocci, L. Joly, A. Michaelides, *Nano letters* **14**, 6872 (2014).

[8] G. J. Wang, N. G. Hadjiconstantinou, *Physical Review Fluids* **2**, 094201 (2017).

[9] X. Wu, X. Xu, C. Guo, H. Zeng, Metal oxide heterostructures for water purification (2014).

[10] T. Liu, X. Liu, N. Graham, W. Yu, K. Sun, *Journal of Membrane Science* **593**, 117431 (2020).

[11] M. Nazari, A. Davoodabadi, D. Huang, T. Luo, H. Ghasemi, *ACS nano* **14**, 16348 (2020).

[12] M. K. Borg, J. M. Reese, *Mrs bulletin* **42**, 294 (2017).

[13] S. Sun, C. Liao, A. M. Hafez, H. Zhu, S. Wu, *Chemical Engineering Journal* **338**, 27 (2018).

[14] V. Augustyn, Y. Gogotsi, *Joule* **1**, 443 (2017).

[15] Zhang, *et al.*, *Bioactive Materials* **5(4)**, 1071 (2020).

[16] J. K. Patra, *et al.*, *Journal of nanobiotechnology* **16**, 71 (2018).

[17] E. Tendong, T. S. Dasgupta, J. Chakrabarti, *Journal of Physics: Condensed Matter* **32**, 325101 (2020).

[18] K. Yamamoto, N. Ota, Y. Tanaka, *Analytical Chemistry* **93**, 332 (2020).

[19] Q. Li, J. Song, F. Besenbacher, M. Dong, *Accounts of chemical research* **48**, 119 (2014).

[20] J. L. Streator, *Surface Energy* (IntechOpen, 2015).

[21] B. Coasne, S. Jain, K. Gubbins, *Physical review letters* **97**, 105702 (2006).

[22] J. Zubeltzu, F. Corsetti, M. Fernández-Serra, E. Artacho, *Physical Review E* **93**, 062137 (2016).

[23] X. Qiu, S. P. Tan, M. Dejam, H. Adidharma, *Chemical Engineering Journal* **405**, 127021 (2021).

[24] E. Tendong, T. Saha-Dasgupta, J. Chakrabarti, *Journal of Physics: Condensed Matter* **34**, 195101 (2022).

[25] G. Algara-Siller, *et al.*, *Nature* **519**, 443 (2015).

[26] M.-C. Bellissent-Funel, R. Sridi-Dorbez, L. Bosio, *The Journal of chemical physics* **104**, 10023 (1996).

[27] W. J. Huisman, *et al.*, *Nature* **390**, 379 (1997).

[28] H. Weiss, *et al.*, *Langmuir* **35**, 16679 (2019).

[29] M. Mezger, *et al.*, *Journal of the American Chemical Society* **132**, 6735 (2010).

[30] M. Mezger, *et al.*, *Proceedings of the National Academy of Sciences* **103**, 18401 (2006).

[31] M. Odelius, M. Bernasconi, M. Parrinello, *Physical Review Letters* **78**, 2855 (1997).

[32] S. Benkoula, *et al.*, *Scientific reports* **5**, 1 (2015).

[33] G. S. Herman, Z. Dohnalek, N. Ruzycki, U. Diebold, *The Journal of Physical Chemistry B* **107**, 2788 (2003).

[34] Q. Xie, *et al.*, *Nature nanotechnology* **13**, 238 (2018).

[35] J. K. Holt, *et al.*, *Science* **312**, 1034 (2006).

[36] P. Sun, *et al.*, *Chemical Communications* **51**, 3251 (2015).

[37] M. P. Goertz, J. Houston, X.-Y. Zhu, *Langmuir* **23**, 5491 (2007).

[38] C. Sendner, D. Horinek, L. Bocquet, R. R. Netz, *Langmuir* **25**, 10768 (2009).

[39] K. Falk, F. Sedlmeier, L. Joly, R. R. Netz, L. Bocquet, *Nano letters* **10**, 4067 (2010).

[40] A. A. Milischuk, B. M. Ladanyi, *The Journal of chemical physics* **135**, 174709 (2011).

[41] R. Lakes, R. S. Lakes, *Viscoelastic materials* (Cambridge university press, 2009).

[42] E. Dollekamp, P. Bampoulis, D. P. Faasen, H. J. Zandvliet, E. S. Kooij, *Langmuir* **33**, 11977 (2017).

[43] S. Saha, *et al.*, *Scientific reports* **4**, 6173 (2014).

[44] J. Azadmanjiri, V. K. Srivastava, P. Kumar, J. Wang, A. Yu, *Journal of Materials Chemistry A* **6**, 13509 (2018).

[45] K. Umeda, K. Kobayashi, T. Minato, H. Yamada, *Physical Review Letters* **122**, 116001 (2019).

[46] D. Ortiz-Young, H.-C. Chiu, S. Kim, K. Voïtchovsky, E. Riedo, *Nature communications* **4**, 1 (2013).

[47] A. Malani, K. Ayappa, *Molecular Simulation* **38**, 1114 (2012).

[48] X. Zhang, Y. Zhu, S. Granick, *Science* **295**, 663 (2002).

[49] G. F. Schneider, V. E. Calado, H. Zandbergen, L. M. Vandersypen, C. Dekker, *Nano letters* **10**, 1912 (2010).

[50] S. P. Surwade, *et al.*, *Nature nanotechnology* **10**, 459 (2015).

[51] A. Siria, M.-L. Bocquet, L. Bocquet, *Nature Reviews Chemistry* **1**, 1 (2017).

[52] Y. Min, M. Akbulut, K. Kristiansen, Y. Golan, J. Israelachvili, *Nanoscience And Technology: A collection of reviews from Nature journals* (World Scientific, 2010), pp. 38–49.

[53] S.-C. Chien, *et al.*, *The Journal of Physical Chemistry C* **121**, 4564 (2017).

[54] M. Imran, *et al.*, *Chemistry of Materials* **28**, 6450 (2016).

[55] R. Qu, *et al.*, *CrystEngComm* **22**, 1853 (2020).

[56] W. Feng, L.-D. Sun, C.-H. Yan, *Langmuir* **27**, 3343 (2011).

[57] A. Castelli, *et al.*, *Nature communications* **9**, 1 (2018).

[58] K. J. Si, Y. Chen, Q. Shi, W. Cheng, *Advanced Science* **5**, 1700179 (2018).

[59] D. Ling, M. J. Hackett, T. Hyeon, *Nano Today* **9**, 457 (2014).

[60] Y. Liu, *et al.*, *Journal of the American Chemical Society* **143**, 16163 (2021).

[61] B. Nikoobakht, Z. Wang, M. El-Sayed, *The Journal of Physical Chemistry B* **104**, 8635 (2000).

[62] Y. Ofir, B. Samanta, V. M. Rotello, *Chemical Society Reviews* **37**, 1814 (2008).

[63] S. Liu, T. Zhu, R. Hu, Z. Liu, *Physical Chemistry Chemical Physics* **4**, 6059 (2002).

[64] Z. Yuan, *et al.*, *Nature communications* **8**, 1 (2017).

[65] P.-X. Wang, *Chemical Communications* **57**, 5051 (2021).

[66] T. Udayabhaskararao, M. Kazes, L. Houben, H. Lin, D. Oron, *Chemistry of Materials* **29**, 1302 (2017).

[67] D. Amgar, A. Stern, D. Rotem, D. Porath, L. Etgar, *Nano letters* **17**, 1007 (2017).

[68] Y. Gao, *et al.*, *Advanced Materials* **30**, 1801805 (2018).

[69] S. Seth, A. Samanta, *Scientific reports* **6**, 1 (2016).

[70] A. Pan, *et al.*, *Acs Nano* **10**, 7943 (2016).

[71] Y. Sun, *et al.*, *RSC Advances* **11**, 27333 (2021).

[72] H. Coy-Diaz, R. Addou, M. Batzill, *The Journal of Physical Chemistry C* **117**, 21006 (2013).

[73] C. Daulbayev, *et al.*, *Applied Surface Science* **549**, 149176 (2021).

[74] Y. Bekenstein, B. A. Koscher, S. W. Eaton, P. Yang, A. P. Alivisatos, *Journal of the American Chemical Society* **137**, 16008 (2015).

[75] X. Zhang, *et al.*, *Nano letters* **16**, 1415 (2016).

[76] S. Ullah, *et al.*, *Materials Advances* **2**, 646 (2021).

[77] Y. Tong, *et al.*, *Angewandte Chemie International Edition* **56**, 13887 (2017).

[78] H. Li, *et al.*, *ACS Applied Nano Materials* **5**, 5527 (2022).

Chapter 2 Methodology

2.1 Introduction:

Experiments are a valuable tool for understanding the behavior of nano-confined fluids and colloidal nanoparticle suspensions, but are yet not suited for studying what happens on a microscopic level at fluid-solid interfaces. Complementary to the experiments, computational modeling and simulation approaches provide insights that are sometimes not extractable from experimental measurements [1]. Continuum simulation methods use macroscopic conservation laws and corresponding constitutive relations to study the behavior of fluids. Validity of constitutive relations relies on the assumption that fluid properties are isotropic and approximately constant across macroscopically small volume elements[2, 3]. This assumption breaks down when variations in macroscopic quantities are large over atomic length scales. The limitations of continuum approaches are avoided by microscopic molecular simulations approaches, such as Monte Carlo (MC) and Molecular Dynamics (MD) simulations. MC and MD simulations deal directly with discrete atoms or molecules, and allow probing individual microscopic interactions at the interfaces, with resolutions which are not attainable by current experimental techniques [4].

In this chapter, we present an overview of the computational methods used in our investigations. We discuss the statistical physics ensembles and common empirical interaction potentials used for molecular simulations in section (1). An outline of MD simulations with a discussion of the most common time integration schemes used in solving the equations of motion for interacting particles, as well as methods for temperature and pressure control, are given in section (2). In section (3) the MC method is discussed with particular attention to the Widom method for determination of chemical potential of a system and Grand Canonical Monte Carlo (GCMC) simulations. We present a brief discussion on how different physical observables relevant to our investigations are obtained from MC and MD simulation data in section (4). A discussion of the metadynamics approach for determining free energy profiles, is given in section (5). We end this chapter with a brief discussion of Quantum mechanical density functional theory, and its use for constructing some of the model structures that are studied in our work, in section (6).

2.1.1 Statistical mechanics and thermodynamic ensembles

MC and MD simulations generate a sequence of points in phase space, with each point corresponding to a micro-state of the system. From a sufficiently large collection of such micro-states, macroscopic observables of the system, such as pressure, energy, heat capacities, etc., can be obtained via statistical mechanics, provided the micro-states belong to the same statistical physics ensemble. An ensemble is a collection of microscopic states of a system, over which a certain minimal set of thermodynamic parameters remains fixed. These parameters, also called macroscopic state variables, include temperature (T), pressure (P), the number of particles (N), volume (V), energy (E), and chemical potential (μ). The macroscopic intensive state variables for a given ensemble are constant at

all times and take the same values at all positions in the system and have no gradients or fluxes. Commonly used ensembles in statistical mechanics are the micro-canonical ensemble (abbreviated NVE), for which the number of particles, volume and total energy of the micro-states are fixed; the canonical ensemble (NVT) with N, V and T fixed; the isobaric-isothermal ensemble (NPT); and the grand canonical ensemble (μVT) with fixed chemical potential, volume and temperature [5, 6].

Microcanonical (NVE) ensemble: In the micro-canonical ensemble, the total energy, volume, and particle number are conserved, while other thermodynamic variables like pressure and temperature may vary. For simulations, this means the equations of motion for the system are solved without any additional constraints on particle velocities, and the system volume and particle number are kept constant. In practice, it is difficult to obtain a fixed energy state because of large fluctuations in the temperature, pressure, entropy, etc. To carry out simulations in the NVE ensemble, it is recommended that the starting configuration be in equilibrium to avoid such large fluctuations. The NVE ensemble is useful for simulating adiabatic systems, consisting of N particles, with fixed volume. Pressure and temperature fluctuations in the NVE ensemble are useful for calculating thermodynamic properties like viscosity and specific heat capacity.

Canonical (NVT) ensemble: The canonical ensemble represents the thermodynamic state of an atomic system having a fixed volume and fixed particle number, in thermal equilibrium with a heat bath at a constant temperature. During simulations in this ensemble, temperature is controlled through the scaling of particle velocities via a process called thermostating. As the system is in thermal contact with a heat bath (thermostat), energy is transferred between the system and the bath until thermal equilibrium is attained. Hence, the total energy of the system is not fixed. The canonical ensemble is the most popular ensemble in practice since, one is generally concerned with the systems in

thermal equilibrium.

Isothermal and Isobaric (NPT) Ensemble : In addition to controlling the temperature, one can control the pressure using an appropriate thermostat/barostat to realize the isothermal, isobaric ensemble. It is abbreviated NPT, as the particle number, pressure, and temperature are fixed at equilibrium. In this ensemble, volume is not constant and is adjusted during the simulation to maintain the desired pressure. The NPT ensemble is useful when pressure and temperature are significant in the system. NPT can be used for equilibrium simulations to simultaneously achieve desired temperature and pressure state.

Grand canonical (μVT) Ensemble : In the grand canonical ensemble, the system can exchange both energy and particles with a reservoir. The system is in thermal and chemical equilibrium with a heat and particle reservoir so that the energy and total number of particles are not constant. This ensemble is also called μVT since the volume, chemical potential, and temperature remain constant in the simulation. The μVT ensemble is useful for simulating coexistence of different phases, such as a liquid or solid in contact with its vapor, in equilibrium such that particles can be exchanged between liquid and vapor and heat is traded between the thermostat bath and the system.

2.1.2 Empirical potential functions or "force fields" in molecular simulations

Classical molecular simulations are based on Newtonian dynamics. According to Newton's second law, the rate of change of momentum $\vec{P_i}$ of an of a particle i is completely determined by the net force $\vec{F_i}$ acting on it

$$\vec{F_i} = \frac{d\vec{P_i}}{dt} \tag{2.1}$$

For a system of interacting particles, this net force arises from the interaction of the particles with the rest of the the system, and can be written as the gradient of the interaction potential:

$$\vec{F_i} = -\vec{\nabla} U(\mathbf{r}), \tag{2.2}$$

where $\mathbf{r}$ is the set of coordinates of all particles in the system and $U(\mathbf{r})$ is the empirical potential energy functions describing the particle's interaction with the rest of the system. The accuracy of any classical simulation strictly depends on the ability of the the potential energy function also known as the "force field", to correctly mimic interactions in the actual system [7]. In designing force fields, it is often desirable to use simple models with minimal number of parameters which capture reliably, the behavior of the system. This facilitates implementation and transferability, and reduces the computational time. The general form of force-fields in molecular modeling can be expressed as a sum of bonded and non-bonded interactions terms :

$$U(\mathbf{r}) = U_{bonded}(\mathbf{r}) + U_{non-bonded}(\mathbf{r}) \tag{2.3}$$

Bonded interactions: Interactions between atoms linked by covalent bonds in a molecule, usually involve stretching along the bonds, bending between the bonds or twisting around the bond axis. From empirical observations bonded atoms can be modeled as balls linked by springs, and the physics of spring deformation used to describe bond stretching, bending and torsion. Stretching involves length change in the bond while bending is related to planar angle change as as shown in Fig. 2.1 (a) and (b) respectively. Torsion represents the twisting motion of sets of atoms located on different planes around the bond axis as illustrated in Fig. 2.1 (c) and (d). Such out of plane bending is also known as dihedral interaction.

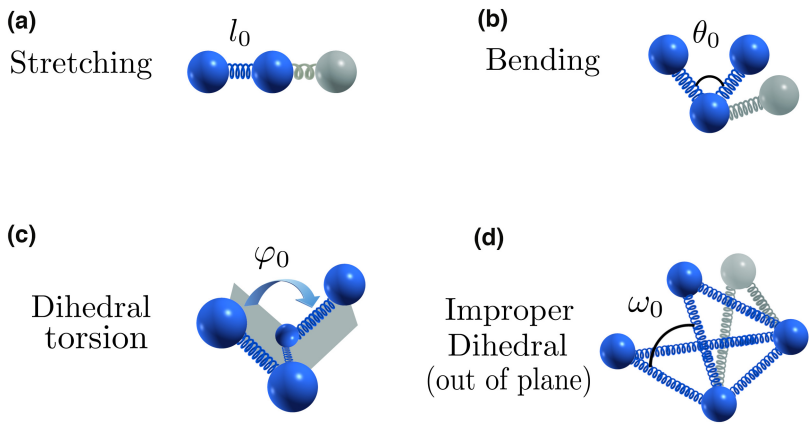

Figure 2.1: Schematic representation of different bonded interactions

The overall bonded interaction can be expressed as [7]:

$$U_{bonded}(r) = \frac{1}{2}[\sum_{bonds} k_l(l-l_0)^2 + \sum_{angles} k_\theta(\theta-\theta_0)^2 + \sum_{dihedrals} k_\varphi(1+cos(\varphi-\varphi_0)) + \sum_{impropers} k_\omega(\omega-\omega_0)^2], \tag{2.4}$$

where k_l,k_θ, k_φ and k_ω are force constants for stiffness of bond stretching, angle bending, dihedral torsion and out of plane or improper dihedral torsion, respectively. l_0, θ_0, φ_0 and ω_0 denote the initial bond lengths and angles while l,θ, φ and ω denote the values after deformation. Bond lengths and stiffness parameters are usually obtained from experiments or from ab-initio quantum mechanical calculations.

Non-bonded interactions: Non-bonded interactions describe van der Waals and electrostatic interactions between non-bonded atoms or molecules. These interactions are typically weaker compared to intra-molecular or bonded interactions. The general form of the potential energy for non-bonded interactions is given by:

$$U_{non-bonded}(\mathbf{r}) = U_{vdW}(\mathbf{r}) + U_{electrostatic}(\mathbf{r}) \tag{2.5}$$

where U_{vdW} is the van der Waals and $U_{electrostatic}$ the electrostatic interaction term. These interactions are usually treated as sums over pairwise terms. For simplicity, sums over triplets and higher order terms are [5].

van der Waals interactions: Traditionally, the Lennard-Jones (LJ) potential is used to mimic van der Waals term. The LJ potential simultaneously considers the repulsive forces between particles at small separations, and attractive forces that occur at larger separations. This potential is given by the following equation [7] :

$$U_{LJ}(r) = 4\varepsilon \left[\left(\frac{\sigma}{r_{ij}} \right)^{12} - \left(\frac{\sigma}{r_{ij}} \right)^{6} \right] \tag{2.6}$$

where r_{ij} is the separation distance between two particles, ε is the well-depth of the interaction potential which measures how strongly the two particles attract each other, and σ is the particle diameter, showing the distance where inter-particle potential is zero. In this equation, the first term represents the steep repulsion experienced by particles at small separations due to Pauli exclusion while second term is the attractive force experienced at larger separations due to induced dipole-dipole or London dispersion. The LJ interaction potential between two particles as a function of their separation is illustrated in Figure 2.2. For transferability, the parameters ε and σ are usually defined for identical atomic species, and for interactions involving dissimilar atomic species, the Lorentz-Berthelot mixing rules [8] are commonly used to determine the LJ parameters for cross interactions. For example, for two atom species A and B, having LJ interaction parameters $(\varepsilon_A, \sigma_A)$ and $(\varepsilon_B, \sigma_B)$, the LJ parameters $(\varepsilon_{AB}, \sigma_{AB})$ for cross interactions of specie A, with B are given by:

$$\varepsilon_{AB} = \sqrt{\varepsilon_A \varepsilon_B}, \qquad \sigma_{AB} = \frac{\sigma_A + \sigma_B}{2}. \tag{2.7}$$

For a LJ particle interacting with an infinite flat wall made of other LJ particles,

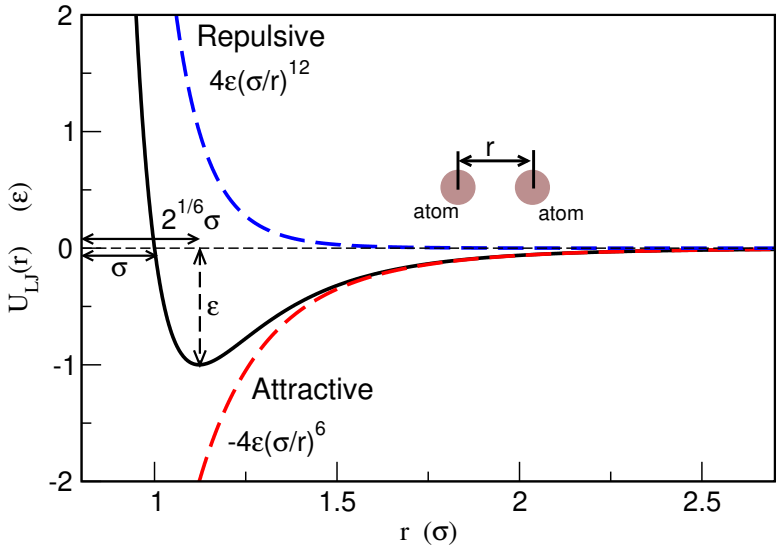

Figure 2.2: Lennard Jones interaction potential (black curve) between two atoms in units of ε and σ. The red and blue curves show respectively the attractive and repulsive parts of the potential.

the effective interaction with the wall can be simplified by assuming that the wall is a pseudo-continuum of density ρ, occupying all space for $z < 0$ and interacting through the usual 12 - 6 LJ potential with parameters $\varepsilon_{wf} = \sqrt{\varepsilon_w \varepsilon_f}$ and $\sigma_{wf} = (\sigma_w + \sigma_f)/2$, where ε_w, σ_w, ε_f, σ_f are the LJ parameters of the wall and the particle respectively. The net interaction of the wall with the particle is obtained be integrating the LJ 12-6 interactions over a half sphere above the continuum wall as illustrated in Fig. 2.3(a):

$$U_{wf}(z) = 4\varepsilon_{wf}\rho \int_0^{2\pi} d\theta \int_{-\infty}^{z} dh \int_0^{\infty} r dr \left(\frac{\sigma_{wf}^{12}}{(r^2+h^2)^6} - \frac{\sigma_{wf}^{6}}{(r^2+h^2)^3} \right) \tag{2.8}$$

$$U_{wf}(z) = \varepsilon_{surf} \left(\frac{2}{15} \frac{\sigma_{wf}^{9}}{z^9} - \frac{\sigma_{wf}^{3}}{z^3} \right), \tag{2.9}$$

where,

$$\varepsilon_{surf} = \frac{2\pi \sigma_{wf}^3 \varepsilon_{wf}}{3}, \tag{2.10}$$

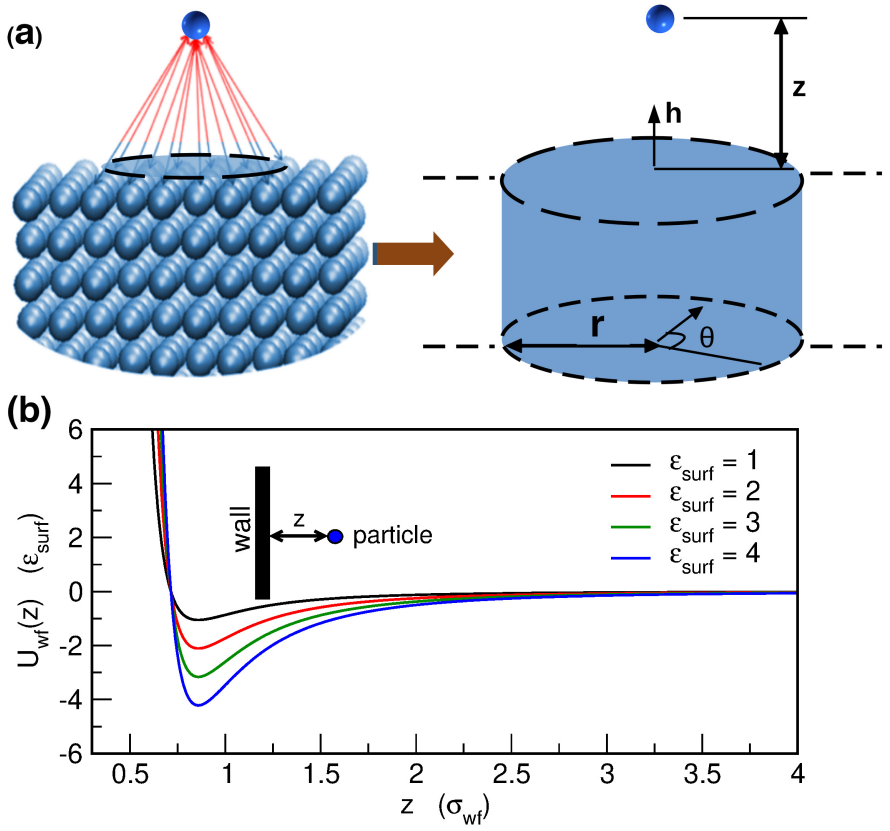

Figure 2.3: (a) Approximation of an atomically detailed wall of 12-6 L-J particles, by a pseudo-continuum structure-less wall via the 9-3 LJ potential. (b) shows the LJ 9-3 interaction potential between a particle and a wall as function of the perpendicular distance z of the particle from the wall, for different ε_{surf}.

Equation 2.9 is known as the 9-3 LJ potential. All interactions of wall particles with a particle above it, are summed into a single wall-particle interaction. This improves considerably the speed of computation of interactions between a fluid and solid surface. Fig. 2.3(b) shows variation of the LJ 9-3 potential as a function of the distance from the wall. In our investigations of wall fluid interactions we use the LJ 9-3 potential to speed up computations. Note that both the 12-6 LJ and the 9-3 LJ potentials decay to a negligible value for $r \sim 2.5\sigma$. Such potentials are called short range potentials. In order to speed up simulations, pairwise interactions for short range potentials are usually calculated only for particles that lie within a given cutoff distance from each other. The typical cutoff distance is usually $\sim 2.5\sigma$.

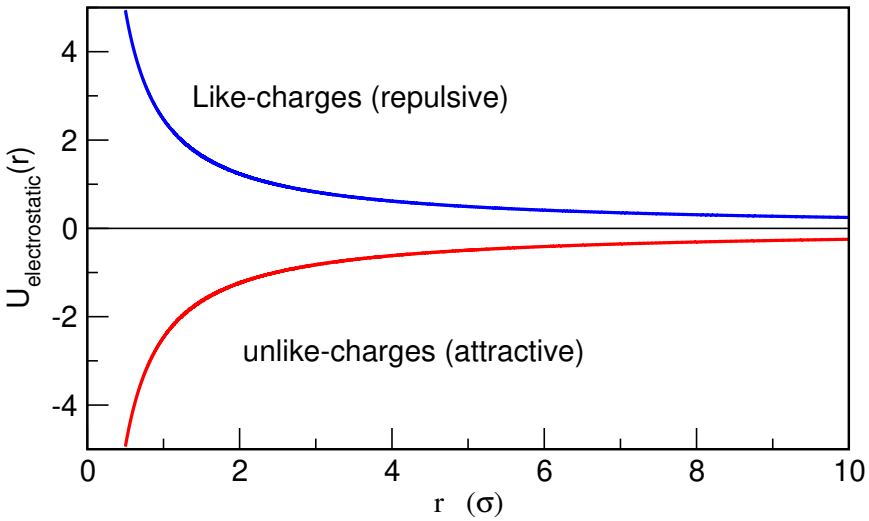

Figure 2.4: Electrostatic interaction potential between like and unlike charges. Note that the potential does decay to zero even at large separations

Electrostatic interactions: Electrostatic interactions between atoms or molecules are usually modeled by the Coulomb potential given by:

$$U_{elctrostatic}(r_{ij}) = \frac{1}{4\pi\epsilon_0}\frac{q_i q_j}{r_{ij}} \tag{2.11}$$

where ϵ_0 is the dielectric constant for vacuum, q_i values are the partial charges, is the distance between the two charges. The typical Coulomb interaction potential for two like and unlike charges is shown in Fig. 2.4. The range of Coulomb interactions is far greater than that of LJ interactions. Such long range effects must be considered in simulations involving charged particles. However, summation of long-range potential for infinite neighboring atoms and periodic images are not convergent. This problem can be handled reasonably using the approach of Ewald summation.

In the Ewald summation method the Coulomb energy of N interacting charges in a neutral simulation box surrounded by infinite periodic replica boxes is divided into two parts: a short-range contribution which converges rapidly in real space, and a long-range contribution which is a slowly varying continuous

function in real space and converges rapidly in reciprocal space [9]. This is done as follows: the charge distribution in the central box is expressed in two parts as $\rho_i(r) = \rho_i^S(r) + \rho_i^L(r)$ where $\rho_i^S(r) = q_i\delta(r-r_i) - q_i G_\sigma(r-r_i)$ and $\rho_i^L(r) = q_i G_\sigma(r-r_i)$. q_i is the charge at position r_i, while $G_\sigma(r-r_i) = \frac{1}{(2\pi\sigma^2)^{3/2}} e^{[-|r|^2/(2\sigma^2)]}$ is a Gaussian fictitious screening charge distribution. The total electrostatic interaction energy of the central box and the periodic images is given by:

$$E = \frac{1}{4\pi\varepsilon_0}\frac{1}{2}\sum_n^\infty \sum_i^N \sum_j^{N'} \int\int \frac{\rho_i(r)\rho_j(r)}{|r-r'+nL|} d^3r d^3r', \tag{2.12}$$

where the symbol $'$ indicates that the summation is for $i \neq j$. Substituting the expression for the charge density, and noting that in a neutral system $\sum_{i=1}^N q_i = 0$, the total coulomb interaction energy can be expressed as $E = E^S + E^L$, with

$$\begin{aligned} E^S &= \frac{1}{4\pi\varepsilon_0}\frac{1}{2}\sum_n^\infty \sum_i^N \sum_j^{N'} \frac{q_i(r)q_j(r)}{|r-r'+nL|} \text{erfc}\left(\frac{|r-r'+nL|}{\sqrt{2}\sigma}\right) \\ E^L &= \frac{1}{L^3\varepsilon_0}\sum_{k\neq 0} \frac{e^{-\sigma^2k^2/2}}{k^2}|S(k)|^2 \end{aligned} \tag{2.13}$$

being respectively the short range and the long range contributions. E^S is short-ranged in real space and is truncated by the conjugate error function erfc. In the summation for E^L, $S(k)$ is the structure factor of the charge distribution computed in the reciprocal space. In practice this is evaluated as follows: First the central simulation box is partitioned into a grid and the point charges are smeared into uniform charges over the nearest grid cell by interpolation. This creates a grid of uniformly spaced charges used to perform the fast Fourier transform in periodic images, with truncation of the wave vector by $e^{-\sigma^2k^2/2}$. The inverse fast Fourier transform is then performed to obtain the long range contribution in real space.

2.2 Molecular Dynamics (MD) Simulation

In the molecular dynamics simulations the positions and velocities of the particles are determined by numerically solving the Newton's equations for a system of interacting particles in time, starting from a known initial configuration. MD provides in principle a time ordered evolution of the system from which both structural and dynamical properties can be calculated. Fig.2.5 shows a schematic representation of a molecular dynamics algorithm.

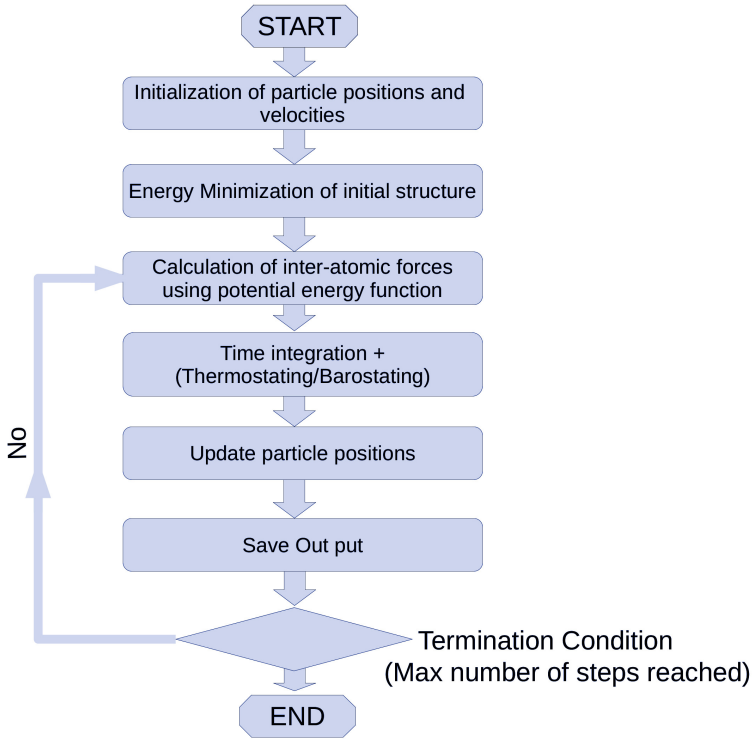

Figure 2.5: Schematic of the molecular dynamics algorithm

2.2.1 Initialization and Energy Minimization

MD simulations require an initial configuration in which the positions and velocities of all atoms in the system are known. In general, the initial positions are

obtained from experimental observations such as crystal structures, theoretical modeling such as MC simulations or randomly distributing particles in the simulation domain such as in the case of mono-atomic fluids. The initial velocities are typically assigned by the Boltzmann or Gaussian distribution at a given temperature. The Boltzmann distribution gives the probability (P) of atom i to have velocities $\vec{v}_{ix}$, $\vec{v}_{iy}$ and $\vec{v}_{iz}$ along the x, y and z directions respectively, at a temperature T, as:

$$p(\vec{v}_{ix}, \vec{v}_{iy}, \vec{v}_{iz}) = \left(\frac{m_i}{2\pi k_B T}\right)^{\frac{2}{3}} e^{-\left(\frac{m_i(\vec{v}_{ix}^2+\vec{v}_{iy}^2+\vec{v}_{iz}^2)}{2k_B T}\right)}, \tag{2.14}$$

where k_B is the Boltzmann constant. In addition the initial velocities are set such that the total linear momentum of the system is equal to zero.

For reliable simulations, it is also required that the initial configuration be at its minimal energy. Adjusting the energy of the initial configuration to a minimal energy is known as energy minimization. This can be done through the help of algorithms such as the method of steepest descent or via conjugate gradient methods. In the steepest descent method atoms are moved such that the net force on each atom reduces. Atomic positions are updated according to the relation $x_{\text{new}} = x_{\text{old}} - \gamma\frac{\partial U}{\partial x}$, where γ is a constant. This method is called steepest decent because the direction in which atoms are moved is opposite to the direction in which the gradient of the interaction potential is largest at the initial point.

2.2.2 Time-integration schemes

Time integration algorithms are used for solving Newton's equations of motion for a system of N interacting particles by assuming that the net force acting on a particle remains constant over a small time interval, and then calculating the displacement of the particle under influence of the force in that time window. By

repeatedly performing these small steps, a time series of the positions, velocities and accelerations of the particles is obtained. This is referred to as the trajectory of the system. For a deterministic treatment it is important that the integration scheme be time-reversible and conserve quantities like energy and momentum. The choice of time step is usually motivated by the the time scale of molecular processes occurring in the system, and the desired degree of accuracy. Long time steps result in less accurate trajectories and do not capture fast molecular processes taking place on smaller time scales. The choice of integration time step is usually of the order of a few femto seconds. Popular time integration algorithms for Newtons equations of motion include the Verlet, Leap-frog and Velocity Verlet algorithms, which all belong to a family of methods called central difference algorithms. These schemes are fundamentally derived from a Taylor series expansion of particle positions and velocities:

$$\begin{aligned}\vec{r}_i(t+\Delta t) &= \vec{r}_i(t) + \Delta t\vec{v}_i(t) + \frac{1}{2}\Delta t^2\vec{a}_i(t) + \mathcal{O}(\Delta t^3) \\ \vec{v}_i(t+\Delta t) &= \vec{v}_i(t) + \Delta t\vec{a}_i(t) + \frac{1}{2}\delta t^2\vec{b}_i(t) + \mathcal{O}(\Delta t^3),\end{aligned} \tag{2.15}$$

with $\vec{r}$ and $\vec{v}$ being the positions and the velocities of a particle i and Δt is the time interval. The series expansion is usually truncated after the quadratic term.

2.2.2.1 The Verlet Algorithm

The Verlet algorithm uses the current positions and accelerations at time t and the positions at the previous time step ($t - \Delta t$), to calculate positions at the new time ($t + \Delta t$). The scheme follows from subtracting the expansions for $\vec{r}_i(t - \Delta t)$

from that for $\vec{r}_i(t + \Delta t)$ (hence the name central difference).

$$\begin{aligned} \vec{r}_i(t + \Delta t) &= \vec{r}_i(t) + \Delta t\vec{v}_i(t) + \frac{1}{2}\Delta t^2\vec{a}_i(t) + \mathcal{O}(\Delta t^3) \\ \vec{r}_i(t - \Delta t) &= \vec{r}_i(t) - \Delta t\vec{v}_i(t) + \frac{1}{2}\Delta t^2\vec{a}_i(t) - \mathcal{O}(\Delta t^3) \\ \implies \vec{r}_i(t + \Delta t) &= 2\vec{r}_i(t) + \vec{r}_i(t - \Delta t) + \Delta t^2\vec{a}_i(t) - \mathcal{O}(\Delta t^4) \end{aligned} \tag{2.16}$$

All terms with odd powers of Δt get eliminated and thus the accuracy of the the final expression is $\sim O(\Delta t)^4$), an order higher than a simple Taylor series expansion. The particle velocity is not included in the integration scheme. The velocity is approximated from the particle positions as follows:

$$\vec{v}_i(t + \Delta t) = \frac{\vec{r}_i(t + \Delta t) - \vec{r}_i(t - \Delta t)}{2\Delta t} + \mathcal{O}(\Delta t^3) \tag{2.17}$$

The disadvantages of this integration scheme are that the positions of particles at two separates times t and $(t - \Delta t)$, have to be stored in the memory at all times and the velocity is determined in an approximate manner. Furthermore, this is not a self-starting algorithm. At $t = 0$ the particle positions at $t = -\Delta t$ are required for calculating the new positions at $t = \Delta t$. One way around this problem is to use the Fourier expansion $\vec{r}_i(\Delta t) = \vec{r}_i(0) + \Delta t\vec{v}_i(0) + \frac{1}{2}\Delta t^2\vec{a}_i(0)$, and then use the positions at $t = 0$ and $t = \Delta t$ to propagate the algorithm.

2.2.2.2 The Velocity Verlet Algorithm

An improvement to the Verlet algorithm is the velocity Verlet algorithm in which the particle positions, velocities and acceleration at current time t, are used to calculate the new positions at $(t + \Delta t)$ as follows:

$$\vec{r}_i(t + \Delta t) = \vec{r}_i(t) + \vec{v}_i(t)\Delta t + \vec{a}_i(t)\frac{\Delta t^2}{2} \tag{2.18}$$

$$\vec{v}_i(t + \Delta t) = \vec{v}_i(t) + \frac{1}{2}\Delta t[\vec{a}_i(t) + \vec{a}_i(t + \Delta t)] \tag{2.19}$$

First the positions at time $(t+\Delta t)$ are calculated from the positions, velocities and accelerations at time t, then the using the new positions, the accelerations at time $(t+\Delta t)$ are calculated, and finally the velocities at $(t+\Delta t)$ are then calculated. The advantage of this scheme is that the velocities are more accurately determined since they are incorporated into the integration scheme. In our simulations we use the velocity Verlet algorithm for integrating the equations of motion.

2.2.3 Periodic boundary conditions, minimum image convention and potential cutoff

Simulating systems with size comparable to that of macroscopic systems is impractical. The simulation domain in Molecular simulations is usually very small compared to actual macroscopic systems, and this can adversely affect the determination of bulk properties. In small finite systems a large fraction of particles lie at the surface, which can introduce fictitious surface effects. Some of these effects can be mitigated in molecular simulations by the introduction of periodic boundary conditions (PBCs). PBCs make the simulation domain appear infinite by replicating images of the simulation box periodically along the given spatial directions. Periodicity along a given direction with simulation cell lying in the interval [0,L], implies that a particles with position $x \in [0,\mathrm{L}]$ has periodic images given by $x' = x \pm nL$, where n is an integer. Thus each particle in the simulation box has an infinite number of periodic images. In this way the simulation domain appears infinite and comparable to macroscopic systems. Figure 2.6 shows a simulation box (blue shade) along with some of its periodic images. The particle images move in unison with the original particle. Thus when a particle exits the simulation cell at one end it is balance by one of its images entering the simulation cell from the opposite end as illustrated by the arrows in Fig.2.6. The number of particles in the simulation cell is thus conserved.

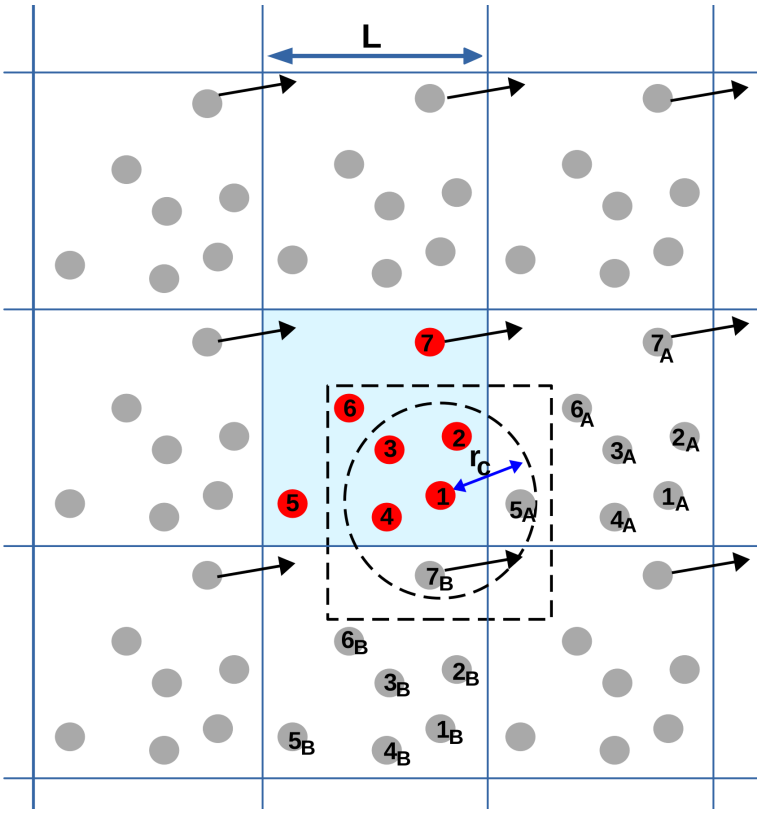

Figure 2.6: Periodic boundary conditions. The actual particles in the box are shown in red and the periodic images are shown in gray. An image particle replaces the original, when the original particle moves out of the simulation box (shown by the arrows). Each particle interacts with other particles or nearest. The region specified by minimum image convention for interactions with particle 1, is shown by the dotted box. The region specified by potential cutoff at distance r_c, is shown by the dotted circle. r_c must be less than half the box length L (Figure adapted from [5]).

In a simulation box of N particles, the potential energy or the net force on one particle is due to the sum of its interaction with the rest of the (N-1) particles in the box. With the use of periodic boundary conditions, this sum includes the interaction with all the infinite periodic images as well. Computing this infinite number of interactions is impossible. For short range potentials, the largest contribution to the potential and forces comes from those particles that are located close to the particle of interest. The sum of interactions may be restricted by making the following assumption: A region of same size and shape as the simulation box with the particle of interest at its center, is considered, and only particles lying within this region are considered to interact with the

central particle. A schematic of the region is shown by a dotted box in Figure 2.6. The particles in this region are the closest periodic images of the rest of the N-1 particles to the central particle. This approach is called the minimum image convention. For example in Figure 2.6, the central box contains 7 particles labeled $1 \rightarrow 7$. The particle of interest 1 is shown at the center of the dotted box. The particles lying within the dotted box $\{2, 3, 4, 6, 5_A$ and $7_B\}$, are the closest periodic images and are considered to interact with 1. Particle 5 and 7 lie outside the region prescribed by minimum image convention and so do not interact with 1. Note that the number of particles in the region specified by the minimum image convention is same as the number in the central box.

The minimum image convention reduces the infinite sum of interactions for a given periodic system of N particles, to $\frac{1}{2}$N(N-1). For large N, this number of interactions is still difficult to evaluate. The number can be further reduced by considering that only atoms which lie within a prescribed distance r_c from the central particle of interest contribute to the interaction. r_c is called the cutoff distance and the potential is assumed to be zero for $r > r_c$. A spherical cutoff represented by the dotted circle in Fig. 2.6, is usually used to preserve the isotropy of interactions. With cutoff, only particles { 2,3,4,5_A and 7_B} contribute to the force on particle 1, while 6 does not. The cutoff distance lies within the region prescribed by the minimum image convention, thus $r_c < \frac{1}{2}$L, where L is the length of the simulation box. For Lennard Jones potential the typical cutoff is usually $r_c = 2.5\sigma$ where σ is the particle size.

2.2.4 Controlling the temperature

MD simulations in various ensembles require control of temperature since real systems are at some given temperature. This is achieved through the use of thermostats [10]. Thermostats are also useful for avoiding energy drifts that may

arise from accumulation of numerical errors during simulations. For a system of N interacting particles, the temperature is related to the particle velocities by:

$$\frac{3}{2}k_B T(N - N_c) = \frac{1}{2}\sum_{o}^{N} m_i v_i^2, \tag{2.20}$$

where N is the number of particles in the system, N_c is the number of constraints, v_i the velocity of the ith particle, k_B the Boltzmann constant .

An obvious way of controlling the temperature will be to scale the velocities particles by a factor λ at every step in the simulation [11]. The corresponding change in the temperature is given by :

$$\begin{aligned} \Delta T = \frac{1}{2}\sum_{i=o}^{N}\frac{2}{3}\frac{m_i(\lambda v_i)^2}{Nk_B} - \frac{1}{2}\sum_{i=o}^{N}\frac{2}{3}\frac{m_i(v_i)^2}{Nk_B} \\ T_0 - T(t) = (\lambda^2 - 1)T(t) \\ \implies T_0 = \lambda^2 T(t) \end{aligned} \tag{2.21}$$

Thus the velocities can be re-scaled by a factor $\lambda = \sqrt{T_0/T(t)}$, where T_{new} is the target temperature and $T(t)$ is the current temperature of the system. The disadvantage of this approach is that temperature fluctuations which are present in the thermodynamic systems are not allowed.

Rather than scaling to the desired temperature in a single step, the scaling factor can be defined such that the rate of change of temperature is proportional to the temperature difference [12]:

$$\frac{dT}{dt} = \frac{1}{\tau}\left(T_0 - T(t)\right), \tag{2.22}$$

where τ is a coupling constant. The change in temperature between successive

time steps will be $\Delta T = \frac{\Delta t}{\tau}(T_0 - T(t))$. The velocity scaling factor then becomes:

$$\lambda^2 = 1 + \frac{\Delta t}{\tau}\left(\frac{T_0}{T(t)} - 1\right) \tag{2.23}$$

The coupling parameter τ controls how fast the temperature reaches the target temperature. This is called the Berendsen thermostat. In the limit $\tau \to \infty$, the thermostat is inactive and the system is in the Micro-canonical ensemble, while $\tau \to \Delta T$ is just the velocity re-scaling case. Thus this thermostat also has the disadvantage that the fluctuations in temperature do not attain the Canonical ensemble.

An alternative way to maintain the temperature is to extend the system by introducing a fictitious dynamical variable $\tilde{s}$ with associated mass Q and velocity $\dot{\tilde{s}}$. This approach is called the Nose-Hoover thermostat [13, 14] and allows to simulate a system which asymptotically (at long times) tends to the Canonical ensemble. The magnitude of Q determines the coupling between the reservoir and the real system. Due to the additional variable, the extended system has (3N + 1) degrees of freedom, where N is the number of particles in the system. Particle coordinates remain same in the extended system as in the real system; $\tilde{r} = r$, while the role of $\tilde{s}$ is to scale the time in the extended system; $d\tilde{t} = \tilde{s}dt$. Thus velocities of particles in the extended system can be written as $\dot{\tilde{r}} = \tilde{s}^{-1}\dot{r}$. The Lagrangian for the extended system can be written as:

$$L = \sum_i \frac{m_i}{2}\tilde{s}^2\dot{\tilde{r}}_i^2 - U(\tilde{r}) + \frac{1}{2}Q\dot{\tilde{s}}^2 - (N+1)k_bT_0\ln\tilde{s} \tag{2.24}$$

The first two terms of equation (2.24) represent the kinetic energy minus the potential energy of the real system, while the last two terms are the kinetic energy minus the potential energy of $\tilde{s}$, chosen such that at steady state ($\dot{\tilde{s}} = 0$), the system describes the canonical ensemble and the kinetic energy is given by $\frac{3}{2}(N +$

$1)k_bT$ as required by equipartition. The corresponding equations of motion are:

$$\begin{aligned}\ddot{\tilde{r}}_i &= \frac{\widetilde{F}_i}{m_i\tilde{s}^2} - \frac{2\dot{\tilde{s}}\dot{\tilde{r}}_i}{\tilde{s}}, \\ \ddot{\tilde{s}} &= \frac{1}{Q\tilde{s}}\left(\sum_i m_i\tilde{s}^2\dot{\tilde{r}}_i^2 - (N+1)k_bT_o\right)\end{aligned} \tag{2.25}$$

These can be solved using time integration algorithms. The extended system describes the micro-canonical ensemble, but since the real system is allowed to exchange energy with $\tilde{s}$, it can be shown that in the asymptotic limit, the real system describes the canonical ensemble. In our investigations we have used the Nose-Hoover thermostat for temperature control.

2.2.5 Controlling pressure

In real systems the pressure is usually well defined, hence controlling pressure is essential during simulation. A number of algorithms exist for controlling the pressure in molecular simulations, one of the simple ones being the Berendsen barostat [12], in which the pressure is controlled by multiply the box dimensions by a global factor ζ. The pressure in a system of N particles in a volume V at temperature T(t), is given by

$$P = \rho T(t) + \frac{1}{3V}\sum_i\sum_{j\neq i}\vec{f}(r_{ij})\cdot\vec{r}_{ij}, \tag{2.26}$$

with ρ the density $\vec{f_{ij}}$ the force on particle i due to particle j, and $\vec{r_{ij}}$ the displacement vector from i to j. If the target pressure is P_0, then the volume scaling factor can be expressed as [15]:

$$\zeta = \left[1 - \frac{\Delta t}{\tau_p}(P(t) - P_0)\right]^{\frac{1}{3}}, \tag{2.27}$$

with $P(t)$ being the current pressure and τ_p a coupling factor determining how fast the pressure is scaled to the target pressure. Re-scaling the simulation box volume in this way at every time step of the simulation my lead to strong oscillations of pressure. The more stable Parrinello-Rahman barostat [16], which uses an extended ensemble approach similar to the Nose-Hoover method, has been used in our investigations.

2.3 Monte Carlo simulations

Monte Carlo simulations model equilibrium thermodynamics and physical properties of a system by generating random configurations of the system, with a probability which is characteristic of the underlying ensemble. Unlike MD, MC simulations do not produce a time ordered trajectory hence MC simulations cannot be used to obtain information on the dynamics of the system. The advantage of MC however is that "un-physical" moves which are not possible in MD, can be performed to rapidly generate new configurations of a system of interest. This makes MC simulations faster and more flexible compared to MD. The precise method by which MC simulations generate the new configurations varies depending on the nature of the system and the statistical ensemble chosen. In the canonical ensemble for example, new configurations are generated by randomly choosing a particle in the simulation domain and then attempting to displace it such that the resultant configuration is an "important" micro-state of the system. The process of generating a new configuration from an old one is called a MC move. "Important" configurations are those that contribute most to the macroscopically observed ensemble averages. Consider a microscopic variable A. Its ensemble average in the canonical ensemble is given as:

$$\langle A \rangle = \frac{\int d\mathbf{r}^N \exp[-\beta U(\mathbf{r}^N)] A(\mathbf{r}^N)}{\int d\mathbf{r}^N \exp[-\beta U(\mathbf{r}^N)]}, \tag{2.28}$$

where $\mathbf{r}^N$ denotes the coordinates of all N particles, U is the potential energy of the system, $\beta = \frac{1}{k_B T}$, k_B is the Boltzmann constant and $\exp[-\beta U]$ is know as the Boltzmann factor. From the numerator of equation (2.28) it is evident that the contribution of $A(\mathbf{r}^N)$ to $\langle A \rangle$ depends on the Boltzmann factor $\exp[-\beta U]$. Hence in order to evaluate $\langle A \rangle$ efficiently, only configurations for which the Boltzmann factor is large are considered. This is referred to as importance sampling. One way of doing this is via the Metropolis scheme.

2.3.1 The Metropolis scheme

Consider a configuration with potential energy $U(\mathrm{r}_1, \cdots, \mathrm{r}_i, \cdots, \mathrm{r}_N)$. A MC move is performed on a random particle i, to yield a new configuration of potential energy $U(\mathrm{r}_1, \cdots, \mathrm{r'}_i, \cdots, \mathrm{r}_N)$. The change in potential energy of the system $\Delta U = [U(\mathrm{r}_1, \cdots, \mathrm{r'}_i, \cdots, \mathrm{r}_N)] - [U(\mathrm{r}_1, \cdots, \mathrm{r}_i, \cdots, \mathrm{r}_N)]$. According to the Metropolis-Hastings algorithm [17]:

1. If $\Delta U \leq 0$ then the move is accepted and the system configuration is updated

2. If $\Delta U > 0$, then the move is accepted subject to a probability. The probability of finding a particle at the new position $p_n \propto \exp\left(-\frac{U(\mathrm{r}_1, \cdots, \mathrm{r'}_i, \cdots, \mathrm{r}_N)}{k_B T}\right)$, while the probability of finding a particle at the initial position is $p_i \propto \exp\left(-\frac{U(\mathrm{r}_1, \cdots, \mathrm{r}_i, \cdots, \mathrm{r}_N)}{k_B T}\right)$. If the ratio $\left(\frac{p_n}{p_i}\right) = \exp\left(-\frac{\Delta U}{k_B T}\right) \geq \gamma$, where is γ is a random number sampled uniformly between 0 and 1, then the move is accepted and the system configuration updated. How ever if $\left(\frac{p_n}{p_i}\right) = \exp\left(-\frac{\Delta U}{k_B T}\right) < \gamma$, then the move is rejected. The acceptance rule can thus be summarized as:

$$P_{\text{acc}} = \min\left[1, \exp(-\beta \Delta U)\right] \tag{2.29}$$

where P_{acc} is the acceptance probability.

In calculating the potential energy of the configuration, the empirical force-fields, periodic boundary conditions as well as the minimum image convention discussed above are respected. For displacement moves, when the displacement is small, the resultant change in the energy of the configuration is minimal and may result in a large acceptance rate, but the phase space will not be sampled properly. Similarly the displacement is too large then almost every moves will be rejected, leading to poor sampling. Hence it is important to tune the displacement such that the acceptance ratio $= \frac{\text{Accepted moves}}{\text{Number of trials}}$ reaches an optimal value ~ 0.5, which ensures the proper sampling of equilibrium phase space. The structural properties and thermodynamics of the system are computed from the collection of accepted microstates.

2.3.2 Determination of the Chemical potential: Widom method

The chemical potential is the change in the total energy of the system when a particle is added or removed from the system. An elegant approach for estimating the chemical potential of moderately dense systems has been proposed by Widom [18, 5]. Consider a mono dispersed system of N interacting particles. The chemical potential of the system is given by:

$$\mu = -k_B T \ln\left(\frac{Z_(N+1)}{Z_N}\right), \tag{2.30}$$

where $Z_(N+1)$ and Z_N are respectively the partition functions for the $(N+1)$ and N particle systems. In the canonical ensemble this can be written as:

$$\mu = -k_B T \ln\left(\frac{V}{\Lambda^d(N+1)}\right) - k_B T \ln\left(\frac{\int_0^1 dr^{N+1} e^{-\beta U(r^{N+1};L)}}{\int_0^1 dr^N e^{-\beta U(r^N;L)}}\right) \;=\; \mu^{id} + \mu^{ex} \tag{2.31}$$

The first term represents the ideal gas contribution (μ^{id}) to the chemical potential , while the second term is the excess part (μ^{ex}) due to particle interaction. The ideal part can be evaluated analytically, and by expressing the energy difference $\Delta U = U(r^{N+1}) - U(r^N)$, the excess part can be written as

$$\mu_{ex} = -k_B T \ln \int dr_{N+1} \left\langle e^{-\beta \Delta U} \right\rangle_N , \tag{2.32}$$

with the angled brackets $\langle \cdots \rangle_N$ denoting the average taken in the canonical ensemble over the configuration space of the N particle system. Equation (2.32) can be sampled by brute force according to the following procedure:

1. Perform MC displacement moves
2. Choose a random location in the simulation domain and insert a particle
3. Calculate the change in the total energy of the system ΔU and calculate the factor $e^{-\beta \Delta U}$
4. Delete the inserted particle.
5. Repeat steps 1 – 4 several times to obtain several values of $e^{-\beta \Delta U}$
6. Calculate the excess chemical potential.

2.3.3 Grand Canonical Monte Carlo (GCMC)

In Grand Canonical Monte Carlo (GCMC) simulations [19, 20], particle insertion and deletion moves are permitted in addition to displacement moves, while the volume V, temperature T and chemical potential μ are kept fixed. Fixing the chemical potential can be interpreted as coupling the system to a particle reservoir. Particles are exchanged between the system and reservoir until the chemical potential of the system matches that of the reservoir. Thus the number of particles

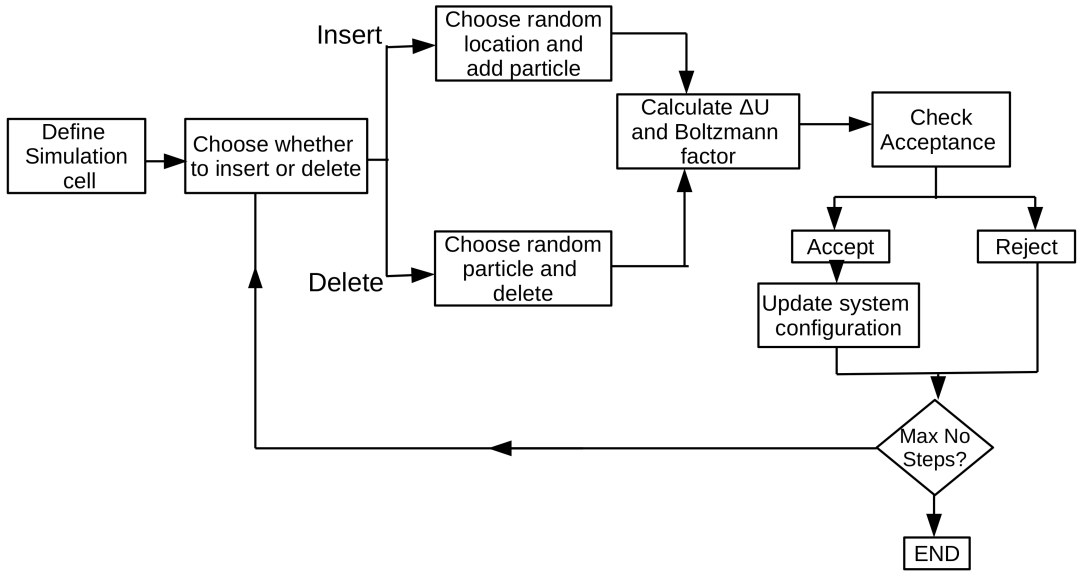

Figure 2.7: Flowchart of grand canonical Monte Carlo simulation algorithm

in the system is not fixed. GCMC is particularly suited for studying the structure and behavior of nano-confined fluids. The acceptance rules for displacement, particle insertion and particle deletion moves are given respectively by:

$$
\begin{aligned}
P_{\text{acc,disp}} &= \min\left[1, \exp(-\beta\Delta U)\right] \\
P_{\text{acc,insert}} &= \min\left[1, \exp(\ln\frac{V}{\Lambda^3} - \ln(N+1) - \beta\Delta U - \beta\mu)\right] \\
P_{\text{acc,delet}} &= \min\left[1, \exp(-\ln\frac{V}{\Lambda^3} + \ln(N+1) - \beta\Delta U - \beta\mu)\right],
\end{aligned}
\tag{2.33}
$$

where Λ is the thermal de Broglie wavelength. For detailed balance, particle displacement, insertion and deletion moves are performed with equal probabilities. Evidently, at high densities the acceptance of particle insertion moves becomes very low. Thus GCMC can only be used for for low and moderately dense systems. Figure 2.7 shows the flowchart of a typical GCMC simulation. First it is decided whether to do displacement, insertion or deletion, with equal probability. For insertion, a random location is chosen within the system. For deletion or displacement, a random particle is chosen from the system. The

change in internal energy ΔU associated with the proposed move is calculated by summing the interactions of all other particles with the particle being inserted or deleted or moved. This then tells us the acceptance probability of the move as per equations 2.33. The move is then accepted or rejected by testing the acceptance probability against a pseudo random number generator. If the move is accepted, the system configuration is updated.

2.4 Calculation of properties from MC and MD simulations

Once equilibrium is attained, properties of the system such as density, pressure, flow rate, temperature, stress are calculated from the trajectories. On the microscopic scale, the unconstrained properties of the system fluctuate. Experimentally measured quantities correspond to ensemble averages of fluctuating microscopic system properties. Here we briefly discuss the various fluid properties that have been investigated in this thesis.

2.4.1 Structural Properties

The structural properties can be calculated from both MD and MC trajectories. We calculate the following quantities:

1. **Radial distribution function:** The radial distribution function (rdf) or pair correlation function describes the probability of finding a particle at a distance r from a given particle. Thus the radial distribution function describes how the density of the system varies in space around a given particle. The radial distribution function can be written as:

$$g(r) = \left\langle \frac{1}{4\pi r^2 \rho \Delta r} \frac{1}{N} \sum_{j=1}^{N} \sum_{i=1}^{N} \delta(r - |\vec{r_j} - \vec{r_i}|) \right\rangle \tag{2.34}$$

In calculating the rdf one finds out how many particles lie within a distance r, to $r + \Delta r$ around a given central particle. In 3D this would mean the number of molecules that lie within a spherical shell of radius r and thickness Δr around a central particle. If the homogeneous bulk density is ρ, then this number will be $4\pi r^2 \rho \Delta r$ in a homogeneous system. This is used a normalization factor. The average $\langle\rangle$ is taken over different simulation snapshots of the equilibrated trajectory. In 2D this factor will be $\rho 2\pi r \Delta r$.

2. **The structure factor:** The structure factor can be obtained directly from neutron scattering experiments and its inverse Fourier transform gives the radial distribution function. In simulations the procedure is somewhat the opposite: one determines first the radial distribution function directly from the simulation data, and then the structure factor is calculated as the Fourier transform of the radial distribution function. The structure factor is given by:

$$S(q) = \left\langle \frac{1}{N} \sum_{j=1}^{N} \sum_{k=1}^{N} e^{-i\vec{q}(\vec{r_j} - \vec{r_k})} \right\rangle \tag{2.35}$$

where $\vec{q} = \vec{k_o} - \vec{k_f}$ is the difference between the wave vector of the incident neutron and the wave vector of the reflected neutrons and $q = |\vec{q}|$. For an isotropic system the Fourier transformation of the rdf yields [5]:

$$S(q) = 1 + 4\pi\rho \int_0^\infty r^2 (g(r) - 1) \frac{sin(qr)}{qr} \tag{2.36}$$

3. **Tetrahedral Order parameter** The tetrahedral order parameter measures the degree of tetrahedrality in the arrangement of molecules. [5]:

$$Q(i) = 1 - \frac{3}{8} \sum_{j=1}^{3} \sum_{k=j+1}^{4} \left(cos(\theta_{jik}) + \frac{1}{3} \right)^2 \tag{2.37}$$

where i is the index of the central molecule, while sum over j and k runs over all possible combinations of the 4 surrounding water molecules (six such combinations are possible).

2.4.2 Dynamic properties

Dynamical properties can be obtained from MD trajectories only. The dynamics at the molecular level are usually captured through various correlation functions like the Van Hove function and the velocity auto-correlation function and mean square displacement .

1. **Self van Hove function:** The self part of the van Hove Correlation function captures the dynamic relaxation in the system. The self Van Hove function gives the probability of finding a particle at a position $r = |\vec{r}|$ at time t, given that the particle was at the origin at time $t = 0$, thus characterizing particle displacements in space and time. For a system of N particles, the Self Van Hove function can be expressed as

$$G_s(r, \Delta t) = \frac{1}{N} \left\langle \sum_{i=1}^{N} \delta(r - |\vec{r_i}(t + \Delta t) - \vec{r_i}(t)|) \right\rangle \tag{2.38}$$

In slab-like geometry one can define the anisotropic self van Hove function

$$G_{s\perp}(r_\perp, z, \Delta t) = \frac{1}{N} \left\langle \sum_{i=1}^{N} \delta(r_\perp - \sqrt{((x_i(t) - x_i(0))^2 + (y_i(t) - y_i(0))^2)}) \right\rangle \tag{2.39}$$

2. **Self intermediat scatering function** The self intermediate scattering function probes the structural relaxation of of a fluid [21] and is defined as:

$$F_s(k, t) = \frac{1}{N} \left\langle \sum_{j=1}^{N} e^{(ik(|\mathbf{r}_j(t) - \mathbf{r}_j(0)|)} \right\rangle, \tag{2.40}$$

where $\mathbf{r}_j(t)$ is the position of particle j at time t, N is the total number of particles and $k = 2\pi\sigma_0$, is the length of the wave vector, set to correspond to the first peak of the particle-particle structure factor. The characteristic time scale for structural relaxation of the fluid, τ_R is defined as the time for $F_s(k,t)$ to drop to a value of $1/e$ [22, 23].

3. **Viscoelastic response:** In a mechanical system with time dependent strain $\gamma(t)$, the general constitutive relation connecting the stress $\sigma(t)$ and the strain in the linear response regime can be written as :

$$\sigma(t) = \int_{-\infty}^{t} C(t-t')\gamma(t')dt', \tag{2.41}$$

Tanking the Fourier transform of both sides of equation (2.41), we can write:

$$\sigma(\omega) \quad = \quad \eta(\omega)\dot{\gamma}(\omega) \quad = \quad \eta(\omega)i\omega\gamma(\omega) \quad = \quad G(\omega)\gamma(\omega), \tag{2.42}$$

where $\dot{\gamma}(\omega) = i\omega\gamma(\omega)$ is the strain rate. $\eta(\omega)$, the ratio of stress and strain-rate is the frequency dependent viscosity and $G(\omega)$ (ratio of stress and strain) is frequency dependent modulus.

$$\eta(\omega) \quad = \quad \frac{\sigma(\omega)}{\dot{\gamma}(\omega)} = \int_0^{\infty} C(t)e^{-i\omega t}dt \tag{2.43}$$

$$G(\omega) \quad = \quad \frac{\sigma(\omega)}{\gamma(\omega)} = i\omega\eta(\omega). \tag{2.44}$$

$C(t)$ is related to the equilibrium stress autocorrelation function (SACF) or stress relaxation function as:

$$C(t) = \frac{1}{Vk_BT}\left\langle \delta\sigma(0)\delta\sigma(t)\right\rangle, \qquad \delta\sigma(t) = \sigma(t) - \left\langle\sigma(t)\right\rangle, \tag{2.45}$$

where the angular brackets $\langle\ \rangle$ denote the ensemble average, V is the volume

of the system, k_B, the Boltzmann constant, T the absolute temperature, and the stress tensor $\sigma(t)$ is given by [5]:

$$\sigma^{\alpha\beta} = \left(\sum_{i=1}^{N} m_i v_i^{\alpha} v_i^{\beta} + \sum_{i}^{N} r_i^{\alpha} f_i^{\beta} \right), \tag{2.46}$$

Here $\alpha, \beta = \{x, y, z\}$, are Cartesian directions, N is the total number of particles in the system, m_i is the mass of the ith particle and v_i^{α} is the component of its velocity in the direction α. f_i^{α} is the component of the force on particle i due to its interaction with the rest of the system (including the confining surfaces) and r_i^{α} is the component of its displacement in the direction α. The first sum in Equation (2.46), represents the kinetic contribution while the second sum represents the contribution of the particle's interaction with the rest of the system, to the stress tensor.

The zero frequency limit of Equation (2.43) yields the Green-Kubo expression for the viscosity, meanwhile the infinite frequency limit of Equation (2.44), gives the infinite frequency elastic modulus G_{∞}, which describes the elastic response of the fluid due to a sudden external force, and has been shown to be = $C(0)$ [24].

$$\lim_{\omega \to \infty} \eta(\omega) \quad = \quad \eta \quad = \quad \int_0^{\infty} C(t) dt \tag{2.47}$$

$$\lim_{\omega \to \infty} G(\omega) \quad = \quad G_{\infty} \quad = \quad C(0). \tag{2.48}$$

2.5 Enhanced sampling and Free energy profiles

MD and MC simulations form a powerful tool for studying complex atomic interactions taking place on rugged energy landscape. Sometimes relevant conformations of the system may be separated by large energy barriers ΔU. The probability of sampling these conformations, which is proportional to the

Boltzmann factor $e^{-\beta\Delta U}$, is very low. Thus, usual MD or MC methods cannot be used to sample such conformations. Enhanced sampling techniques have been developed to counter this problem. In this thesis we make use of the approach of metadynamics.

2.5.1 Metadynamics

Metadynamics [25] is an MD-based method that aims to enhance the exploration of the free energy surface, $F(\mathbf{S}(\mathbf{r})$ of a limited set of collective variables. A collective variable is any explicit continuous function $\mathbf{S}(\mathbf{r})$ of the coordinates such as bond lengths, torsion angles, coordination numbers, distances etc which can clearly distinguish between the initial, intermediate and final state of the system of interest [26]. In Metadynamics, the probability of visiting high free energy states is increased by adding an adaptive Gaussian external potential to the Hamiltonian during a normal MD simulation as follows:

$$H(\mathbf{p},\mathbf{r},t) = H(\mathbf{p},\mathbf{r}) + V(S(\mathbf{r}),t) \tag{2.49}$$

where $H(\mathbf{p,r})$ is the Hamiltonian of the unbiased system, while V(S(**r**),t) is the metadynamics biasing potential given by:

$$V_M(S(\mathbf{r},t)) = \int_0^t dt' \omega_0 \exp\left(-\sum_{i+0}^{d} \frac{[S_i(\mathbf{r}) - S_i(\mathbf{r}(t'))]^2}{2\sigma_i^2}\right), \tag{2.50}$$

where $V_M(S,t)$ is the total potential that has been deposited at time t in the space of the collective variables S. d is the number of collective variables, S_i is the ith collective variable and $S_i(\mathbf{r}(t'))$ is the instantaneous value of the ith collective variable, and ω_0 is the height of the deposited Gaussian. The added potential discourages the revisiting of states that have already been visited by the system, and improves the exploration of the phase space. When the system is stuck in a

minima, more and more Gaussian's are added at that CV value until the system is pushed out of that minima. When all minima are filled, then the system diffuses freely and at this point the simulation can be stopped. The free energy surface is then obtained as the negative of the total deposited bias.

$$V_M(S, t \to \infty) = -F(S) + C, \tag{2.51}$$

where C is an undetermined constant.

A major drawback of standard Metadynamics in this way is that it is unclear when to terminate the simulation and this results in overfilling of the free energy landscape and the obtained free energy difference between two points tends to oscillate about the true value. To overcome this convergence problem, the well tempered metadynamics scheme has been proposed [27, 28]. In the well-tempered metadynamics, the height of the Gaussian bias is reduced with time as follows:

$$\omega(S, t) = \omega_0 \exp\left[\frac{-V_M(S, t)}{k_B \Delta T}\right], \tag{2.52}$$

where ω_0 is the initial height of the Gaussian, V_W the total bias deposited prior to time t and ΔT is a coupling parameter (bias factor) which determines the rate of decay of the deposited Gaussians. ΔT has dimensions of temperature. In the long time limit, the height of the Gaussian functions became negligible, and the well tempered (WT) metadynamics potential converges to the following function of the free energy :

$$V_M(S, t \to \infty) = -\frac{\Delta T}{T + \Delta T} F(S) + C, \tag{2.53}$$

Apart from improving the convergence, well tempered metadynamics also has the advantage that the bias factor ΔT can be tuned to yield two limiting cases. In the limit $\Delta T \to 0$, one gets normal $\omega(S, t) \to 0$, which is simply the normal

MD with no biasing, while in the limit $\Delta T \rightarrow \infty$, one recovers the standard metadynamics $\omega(S,t) \rightarrow \omega_0$.

2.6 Quantum mechanical calculations

Description of phenomena in which chemical bonds are broken and formed, such as surface formation energies or vacancy formation energies need to include the electronic degrees of freedom. Such calculations are done through quantum mechanics based methods such as density functional theory [29]. For a system of atoms or molecules it is known that the nuclear and electronic degrees of freedom can be decoupled due to slow nuclear motion compared to the motion of electrons. Density functional theory provides an efficient framework for treating the electronic degrees of freedom, in which an interacting N electron system is mapped unto a system of N non-interacting electrons in an effective external potential. According to the Hohenberg-Kohn theorems [30], this external potential is uniquely determined by the electronic charge density $\rho(r)$, and the charge density that minimizes the total energy, is the ground state charge density. The Hamiltonian of the non interacting electrons is given by :

$$\begin{aligned} H_{KS} &= -\frac{\hbar}{2m}\nabla^2 + V_{eff}(r;\rho) \\ \text{where} \quad V_{eff}(r,\rho) &= V_{ext}(r) + \frac{e^2}{2(4\pi\epsilon_0)}\int \frac{\rho(r')}{|r-r'|}dr' + E_{XC}(r) \end{aligned} \tag{2.54}$$

Here, $V_{eff}(r)$ is the effective potential experienced by the electron. In the expression for $V_{eff}(r)$, the first term $V_{ext}(r)$ is the external potential due to the atomic nuclei, the second term is the coulomb interaction between the electron than the rest of the electrons, while the last term $E_{XC}(r)$ contains all the exchange and correlations effects on the electron.The single electron wave function thus

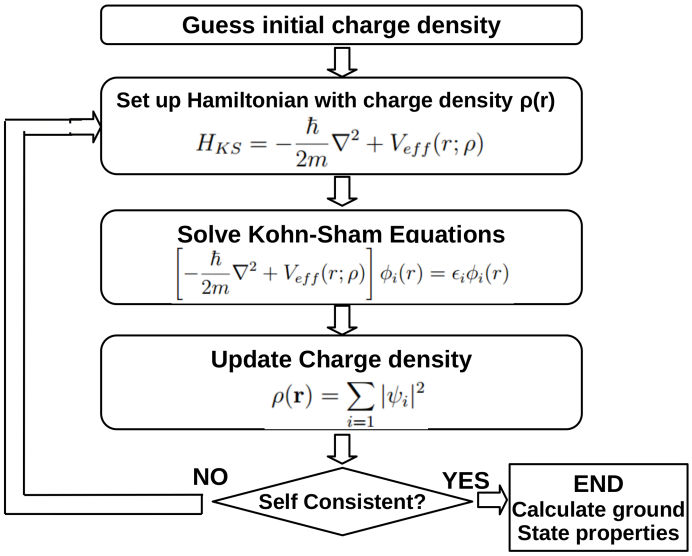

Figure 2.8: Flowchart illustrating the iterative procedure to solve the Kohn-sham equations

satisfies the following Schrodinger-like equation:

$$\left[-\frac{\hbar}{2m}\nabla^2 + V_{eff}(r;\rho)\right]\phi_i(r) = \epsilon_i\phi_i(r) \tag{2.55}$$

The charge density itself can be constructed from the sum over the single electron wave functions as:

$$\rho(\mathbf{r}) = \sum_{i=1} |\psi_i|^2 \tag{2.56}$$

Equations 2.54, 2.55 and 2.56 provide a framework for obtaining the ground state charge density and energy in a self consistent iterative manner as shown in Fig 2.8. One starts by making a guess of the electronic charge density $\rho(r)$, use it to establish the effective potential V_{eff}, then solve the Schrodinger-like Kohn-Sham equations to obtain the single electron $\phi_i(r)$, use the $\phi_i(r)$ to calculate the new charge density and repeat the entire cycle until a self consistency condition is reached when the output charge density differs from the input charge density by a preassigned small value.

In the formalism detailed above, the exact form of the exchange correlation contribution $E_{XC}[\rho(r)]$ is unknown. Various approximations have been developed for E_{XC}, the most common being the local density approximation (LDA) and the generalized gradient approximation (GGA). In the LDA, the exchange-correlation energy of an in-homogeneous electron system having the charge density $\rho(r)$ at any point r in space, is considered to be equal to the exchange-correlation energy of a homogeneous electron gas having the same electron charge density $\rho(r)$. Exchange -correlation functionals for the homogeneous electron gas have been estimated by Ceperley and Adler [31], using quantum Monte Carlo simulations. Various parametrizations of the these functionals have also been reported. These include parametrizations by Perdew and Zunger [32], Perdew and Wang [33], etc . These are known as LDA functionals. LDA is known to work best for systems in which the charge density is a slow varying function of the spatial coordinates. GGA considers additionally the gradient of the charge density in the parametrization of E_{XC}, and results in better accuracy than LDA. Several parametrizations of E_{XC} using the GGA have been reported. These are known as GGA functionals and include parametrizations by Perdew-Wang [34] and Perdew-Burke-Ernzerhof (PBE) [35] etc.

In this thesis we perform density functional theory calculations using the PBE GGA exchange-correlation functional. The wave functions are expanded using the plane-wave basis set as implemented in Vienna ab-initio simulation package [36, 37], with projector-augmented wave potential [38]. We calculate surface formation energies for different crystal surfaces, and vacancy formation energies for the formation of vacancies at different crystal surfaces. This permits us to construct realistic models of surfaces and nano-particles, which we use for molecular dynamics investigations.

References

[1] G. W. Brodland, *Seminars in cell & developmental biology* (Elsevier, 2015), vol. 47, pp. 62–73.

[2] X. Nie, S. Chen, M. Robbins, *et al.*, *Journal of Fluid Mechanics* **500**, 55 (2004).

[3] J. S. Hansen, J. C. Dyre, P. Daivis, B. D. Todd, H. Bruus, *Langmuir* **31**, 13275 (2015).

[4] R. W. Carpick, M. Salmeron, *Chemical reviews* **97**, 1163 (1997).

[5] J.-P. Hansen, I. R. McDonald, *Theory of simple liquids: with applications to soft matter* (Academic press, 2013).

[6] D. Frenkel, B. Smit, *Understanding molecular simulation: from algorithms to applications*, vol. 1 (Elsevier, 2001).

[7] M. P. Allen, D. J. Tildesley, *Computer simulation of liquids* (Oxford university press, 2017).

[8] D. Boda, D. Henderson, *Molecular Physics* **106**, 2367 (2008).

[9] I.-C. Yeh, M. L. Berkowitz, *The Journal of chemical physics* **111**, 3155 (1999).

[10] P. H. Hünenberger, *Advanced computer simulation* (Springer, 2005), pp. 105–149.

[11] V. Rühle, *Am. J. Phys* pp. 1–4 (2007).

[12] H. J. Berendsen, J. v. Postma, W. F. Van Gunsteren, A. DiNola, J. R. Haak, *The Journal of chemical physics* **81**, 3684 (1984).

[13] S. Nosé, *The Journal of chemical physics* **81**, 511 (1984).

[14] D. J. Evans, B. L. Holian, *The Journal of chemical physics* **83**, 4069 (1985).

[15] H. C. Andersen, *The Journal of chemical physics* **72**, 2384 (1980).

[16] M. Parrinello, A. Rahman, *Journal of Applied physics* **52**, 7182 (1981).

[17] N. Metropolis, A. W. Rosenbluth, M. N. Rosenbluth, A. H. Teller, E. Teller, *The journal of chemical physics* **21**, 1087 (1953).

[18] B. Widom, *The Journal of Chemical Physics* **39**, 2808 (1963).

[19] D. Adams, *Molecular Physics* **29**, 307 (1975).

[20] D. Adams, *Molecular Physics* **28**, 1241 (1974).

[21] T. S. Ingebrigtsen, J. R. Errington, T. M. Truskett, J. C. Dyre, *Physical review letters* **111**, 235901 (2013).

[22] N. Kuon, A. A. Milischuk, B. M. Ladanyi, E. Flenner, *The Journal of chemical physics* **146**, 214501 (2017).

[23] S. Krishnan, K. Ayappa, *Physical Review E* **86**, 011504 (2012).

[24] R. Zwanzig, R. D. Mountain, *The Journal of Chemical Physics* **43**, 4464 (1965).

[25] A. Laio, M. Parrinello, *Proceedings of the National Academy of Sciences* **99**, 12562 (2002).

[26] S. Hayward, N. Go, *Annual review of physical chemistry* **46**, 223 (1995).

[27] A. Barducci, G. Bussi, M. Parrinello, *Physical review letters* **100**, 020603 (2008).

[28] A. Barducci, M. Bonomi, M. Parrinello, *Wiley Interdisciplinary Reviews: Computational Molecular Science* **1**, 826 (2011).

[29] R. M. Martin, *Electronic structure: basic theory and practical methods* (Cambridge university press, 2020).

[30] N. W. Ashcroft, N. D. Mermin, *et al.*, Solid state physics (1976).

[31] D. Ceperley, B. Alder, *Science* **231**, 555 (1986).

[32] J. P. Perdew, A. Zunger, *Physical Review B* **23**, 5048 (1981).

[33] J. P. Perdew, Y. Wang, *Physical Review B* **98**, 079904 (2018).

[34] J. P. Perdew, Y. Wang, *Physical review B* **45**, 13244 (1992).

[35] J. P. Perdew, K. Burke, M. Ernzerhof, *Physical review letters* **77**, 3865 (1996).

[36] G. Kresse, J. Furthmüller, *Physical review B* **54**, 11169 (1996).

[37] G. Kresse, *Journal of Non-Crystalline Solids* **192**, 222 (1995).

[38] P. E. Blöchl, *Physical review B* **50**, 17953 (1994).

Chapter 3 Structure, phase behavior and viscoelastic response of fluid in asymmetric nanoconfinement *

3.1 Introduction

As introduced in Chapter 1, fluids nano-confined at heterostructure interfaces behave very differently compared to their bulk counterparts. With the recent development of interfaces with tuneable wetting using 2-D van der Waal materials like graphene and hexagonal boron nitride [1], several new applications have been envisaged in the domain of nanofluidics, such as water filtration [2, 3, 4, 5], energy storage [6, 7], drug delivery [8, 9, 10], confinement-controlled chemistry in aqueous media [11, 5], nano-fluidic transistors and diodes [12, 13], to name only a few. These applications exploit the phase behavior and transport properties of fluids trapped between surfaces having dissimilar wetting tendencies. Though the electronic properties of hetero-structures have been looked into in details [14, 15], relatively less is known about transport of fluids trapped at interface between two differently wettable surfaces.

An important transport property of fluids is their viscoelasticity; the ability of the fluid to exhibit both solid-like elasticity and liquid-like viscosity depending

*This Chapter is based on the following publication:
E. Tendong, T. Saha Dasgupta, and J. Chakrabarti. Journal of Physics: Condensed Matter 34.19 (2022): 195101

on the timescale of observation. Viscoelastic behavior is usually characterized by the frequency dependent elastic (storage) and viscous (loss) moduli [16]. These moduli measure respectively the degree of liquid-like and solid-like response of fluid undergoing mechanical perturbation at a given frequency. As the frequency of perturbation increases, solid-like behavior (storage modulus) increases, while the liquid-like behavior (loss modulus) reduces. The inverse frequency at which the storage and loss moduli become equal in magnitude, is the viscoelastic relaxation time of the fluid [17].

Viscoelastic response and phase behavior of fluids under symmetric confinements where the confining walls are identical, have been extensively studied in the past. The fluids are found to exhibit layered structures, with in-plane ordering of fluid layers, alternating between triangular and square packing as the slit size is varied [18, 19, 20, 21, 22, 23, 24, 25, 26]. Changes in viscoelastic relaxation time scale due to molecular rearrangement in the fluid as slit-width is varied have also been studied[27, 28, 20].

Unlike symmetric channels [21, 29, 22, 30, 31], unequal interaction strengths of confining walls with the fluid tend to disrupt formation of frozen phases [32]. Experimental studies have reported noisy frequency-dependent shear responses for asymmetrically confined water [33] due to competing tendencies of water to wet the hydrophilic surface and de-wet the hydrophobic one. Detail knowledge of the fluid structure and transport properties is necessary for realizing various applications. However, to the best of our knowledge, there has not yet been any attempt to investigate the viscoelastic properties of asymmetrically confined fluids resulting from different tendencies of wetting at the boundaries.

In the current chapter, using GCMC and MD simulations, we explore the phase behavior and viscoelastic relaxation of a single component fluid trapped between two van der Waals' walls with different wettability, and separated by a distance of few times the particle size (strong confinement regime [10]). The

trapped fluid is considered to be of Lennard-Jones (LJ) type, while the walls are modeled as structure-less continuum solids having different wettability. One of the surfaces is considered to interact strongly with the fluid, corresponding to a completely wet surface, while the second surface interacts weakly with the fluid, corresponding to a partially wet surface. The ratio of the interaction strengths of the walls with the fluid defines the asymmetry of the slit denoted ξ. We study the structure and phase changes of the asymmetrically confined fluid film, with changing slit width and asymmetry. We also investigate the viscoelastic response of the asymmetrically confined fluid film as the asymmetry and slit size are varied, and relate it to the observed structural changes.

It is found that with increasing asymmetry there is a crossover in the effective density of fluid in the slit from rarer (R) to denser (D) than bulk density at an asymmetry $\xi(= \xi_{RD})$. The in-plane ordering of the fluid film is also observed to undergo a transition from disordered phase F to a phase with triangular bond-orientational order S for sufficiently large $\xi(= \xi_{FS})$, passing though an intermediate phase with mixed ordered and disordered patches.

The viscoelastic response of the asymmetrically confined fluid film, is probed by performing MD simulations on a number of equilibrated configurations from the GCMC simulations, to extract the loss and storage modulus so far as the system remains in fluid-like phase. We find that the compression moduli transverse to the confinement direction, have the slowest relaxation time scales. For low frequencies, the loss modulus is higher than the the storage modulus, meanwhile at high frequencies the storage modulus becomes dominant. The frequency at which the loss modulus and storage modulus have equal magnitude, defines the viscoelastic relaxation time. Below the R$\rightarrow$D crossover (i.e for $\xi < \xi_{RD}$), the viscoelastic relaxation time varies slowly as the asymmetry increases, following the variation of the structural relaxation time. For $\xi > \xi_{RD}$, the viscoelastic relaxation time increases sharply with changing asymmetry, deviating from the

structural relaxation time. This two regime behavior of the viscoelastic relaxation time is found to be universal for all the slit widths in the strong confinement regime. In the vicinity of ordering transition ($\xi \sim \xi_{FS}$), on the other hand, the storage and loss modulus cross-over becomes ill-defined with the two moduli overlapping as in gel. The storage component takes over the loss component, for large asymmetry as in a crystal phase, even before the long ranged order sets in.

3.2 Computational details

3.2.1 Simulation setup

A schematic of the simulation setup for a Lennard-Jones (LJ) fluid in a slit-like pore with asymmetric wall-fluid interaction is illustrated in Figure 3.1. The fluid-fluid interactions U_{ff}, are described using the LJ 12-6 potential,

$$U_{ff}(r_{ij}) = 4\varepsilon_{ff}\left[\left(\frac{\sigma_o}{r_{ij}}\right)^{12} - \left(\frac{\sigma_o}{r_{ij}}\right)^{6}\right], \tag{3.1}$$

where $r_{ij} = |\mathbf{r_j} - \mathbf{r_i}|$ is the distance between the centers of a pair of interacting fluid particles i and j. ε_{ff} is the potential well depth, σ_o is the diameter of fluid particles and interactions between fluid particles are truncated for $r_{ij} > 3.5\sigma_o$.

The fluid film is confined between two structure-less solid walls of sides $40\sigma_o \times 40\sigma_o$, with periodic boundaries along x and y, placed at a separation h, ranging from $1.5\sigma_o$ to $3.5\sigma_o$ along the z direction. The strongly interacting wall is place at $-h/2$ and the weakly interacting wall at $h/2$ (see Figure 3.1). Interactions of the fluid with each of the confining walls U_{wf}, are modeled via the 9-3 LJ potential [34, 35, 36, 37].

$$U_{wf}(z_i) = \varepsilon_{wf}\left[\frac{2}{15}\left(\frac{\sigma_{wf}}{z_i}\right)^{9} - \left(\frac{\sigma_{wf}}{z_i}\right)^{3}\right], \tag{3.2}$$

Here z_i is the perpendicular distance from the ith particle to a wall, and ε_{wf} represents the wall-fluid interaction strength. The derivation of this potential has been elaborated in Chapter 2. To model the slit asymmetry, the strength of interaction of fluid with one of the confining surfaces, denoted $\varepsilon_{wf} = \varepsilon_S$, is taken to be stronger than the interaction strength of the fluid with the second wall, denoted $\varepsilon_{wf} = \varepsilon_W$ as shown in Figure 3.1. The asymmetry in interaction strengths of the two confining walls with the fluid is represented by a parameter ξ defined as

$$\xi = \frac{\varepsilon_S}{\varepsilon_W}. \tag{3.3}$$

In all the simulations of the asymmetric slits, we set $\varepsilon_W = \varepsilon_{ff}$ typical for solvophobic surface, while ε_S is varied to obtain different values of asymmetry ξ from 1 to 16 . For both walls $\sigma_{wf} = \sigma_o$ and the cutoff distance of wall-fluid interactions is same as that of the fluid-fluid interaction. All quantities are expressed in terms of energy, distance and mass units, which are set respectively by the potential parameters ε_{ff} and σ_o, and the particle mass m. [38]

3.2.2 Determination of chemical potential

For GCMC simulations, the slit is considered in equilibrium with a virtual LJ bulk liquid reservoir close to the solid-liquid coexistence line with density $\rho_0 = 0.9$ and temperature $T = 1.0$. The chemical potential for this phase point is determined via the Widom test particle insertion method outlined in Chapter 2. For this, 3000 particles are randomly placed in a cubic simulation box of sides $15\sigma_0$ and equilibrated within the NVE ensemble using a self developed MD code. Particle positions and momenta are updated following the velocity Verlet scheme for a 10^4 steps. This is followed by 2×10^6 simulation steps in NVE ensemble during which a test particle insertion is attempted after every 10 steps. The excess chemical potential obtained from test particle insertion is $\mu_{ex} = 0.41$. The

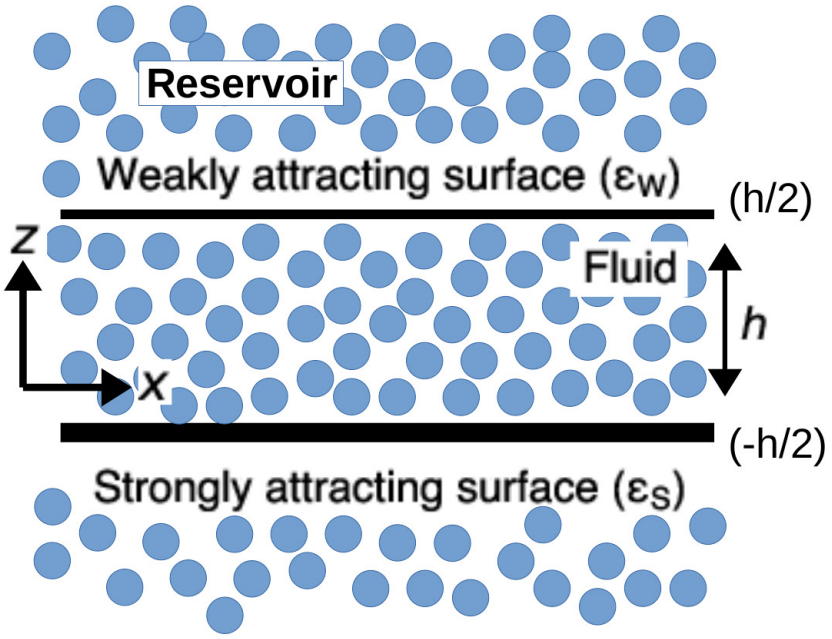

Figure 3.1: Schematic representation of the simulation cell showing fluid confined by strongly attracting and weakly attraction structureless walls at a separation h, in equilibrium with a reservoir. (The y-axis not shown is pointing into the page).

chemical potential $\mu = \mu_{id} + \mu_{ex}$ where $\mu_{id} = k_B T \ln \rho = -0.11$, is the ideal part and μ_{ex} is the excess part. The chemical potential is found to be $\mu = 0.3$, in agreement with previously reported data [39]. This value is kept fixed for all the GCMC simulations thus ensuring that all slits considered are in thermodynamic equilibrium with the same bulk phase [40, 41].

3.2.3 Simulation details

All simulations have been carried out using the Large-scale Atomic/Molecular Massively Parallel Simulator (LAMMPS) package [42], with interaction potentials as defined in Equation (4.1) and (4.2). Each of the GCMC simulations consists of 2×10^6 GCMC steps with 100 trial moves per step for equilibration, and 5×10^6 GCMC steps of production run, with the system trajectory recorded every five steps and used for evaluating the structural properties.

To obtain the viscoelastic properties, five independent equilibrated config-

urations are taken from each of the GCMC simulations and used to perform equilibrium MD simulations in the constant particle number, constant volume (NVE) ensemble. 1×10^6 equilibration steps with the Langevin thermostat used to adjust the system temperature, after which the thermostat is turned off. 5×10^6 production steps with a time step $\delta t = 0.001$, are then performed, during which the system configuration is saved every step. The results averaged over all five independent trajectories for improved accuracy.

3.3 Analysis

We analyze the structure and viscoelastic response of the confined fluid through the following quantities:

(a) Mean density: The mean density of fluid confined in the channel is given by :

$$\langle \rho \rangle = \frac{\langle N \rangle}{A \times h_{eff}}, \tag{3.4}$$

where $\langle N \rangle$ is the mean number of particles within the slit in the equilibrated portion of the trajectory from the GCMC simulations, A, is the cross-sectional area of the slit and $h_{eff} = h - 2\gamma$ is the effective slit width accessible to the fluid. $\gamma = 0.44\sigma_0$ corresponding to the distance from the inner wall surface to the wall-fluid boundary, which is inaccessible to the fluid due to Pauli repulsion [43].

(b) Density profile: The density profile gives the distribution of fluid along the confinement direction, and can be expressed as:

$$\rho(z) = \frac{1}{L \times L \times \Delta z} \left\langle \sum_{i=1}^{N} \phi(r_i - z) \right\rangle, \tag{3.5}$$

where $\phi(r_i - z) = 1$ if $z \leq r_i \leq z + \Delta z$, and zero otherwise. N is the total number of particles in the slit, L is the box length and the angled brackets represent an

average over different time frames.

(c) Bond orientation order parameter: As introduced in Chapter 2, the bond orientation order parameter of a 2-D fluid layer, is given by:

$$\Psi_n = \left\langle 1/N_l \sum_{0}^{N_l} \psi_n(r_j) \right\rangle, \tag{3.6}$$

where N_l is the number of particles in the fluid layer, $\psi_n(r_j) = \left| \frac{1}{N_j} \sum_k^{N_j} e^{in\theta_{jk}} \right|$ is the local bond order, N_j is the number of nearest neighbors of a particle j with position r_j, all lying in the same layer, and θ_{jk} is the angle between a line joining particle j to its k-th neighbor in the same layer and an arbitrary fixed axis. n = $\{4, 6\}$ represents the rotational symmetry of the layer.

(d) Viscoelastic relaxation time: The viscoelasticity of the fluid film is characterized through the complex frequency dependent viscosity given by the generalized Green-Kubo relation [44, 45]:

$$\eta_{\alpha\beta}(\omega) = \frac{V}{k_B T} \int_0^\infty C_{\alpha\beta}(t) e^{-i\omega t} dt = \frac{1}{\omega} \left(G^S_{\alpha\beta}(\omega) - i G^L_{\alpha\beta}(\omega) \right), \tag{3.7}$$

where $C_{\alpha\beta}(t)$, is the stress auto-correlation function (SACF) obtained from various components of the stress tensor $\sigma_{\alpha\beta}$ as outlined in Chapter 2. V is the effective volume of the slit, T the temperature, k_B the Boltzmann factor and ω is the angular frequency. $G^S_{\alpha\beta}(\omega)$ is called the storage modulus as it characterizes the ability of the fluid to store elastic energy, while $G^L_{\alpha\beta}(\omega)$ represents the viscous contribution to the system's response and is called the loss modulus. The viscoelastic relaxation time $\tau_{\alpha\beta} = 1/\omega$ corresponds to the inverse frequency at which the loss modulus is equal to the storage modulus $G^S_{\alpha\beta}(\omega) = G^L_{\alpha\beta}(\omega)$.

(e) Structural relaxation time: Structural relaxation of the fluid is probed via the self (incoherent) intermediate scattering function [37] $F_s(k, t)$ described in Chapter 2. The characteristic time scale for structural relaxation of the fluid, τ_R

is defined as the time for $F_s(k,t)$ to drop to a value of $1/e$ [46, 47].

3.4 Results and Discussion

3.4.1 Structural changes

We first focus on structural data obtained from the GCMC simulations. The evaluate the mean number density $\langle\rho\rangle$ of fluid in the slit given by Equation (3.4). For a given ξ , the plot of $\langle\rho\rangle/\rho_0$ vs h , where ρ_0 is the bulk density, exhibits oscillatory behavior. The oscillations get more pronounced for larger ξ values as shown in Figure 3.2(a). The peaks occur when number of fluid layers formed is commensurate with the slit-width [48, 49]. The first peak corresponds to one commensurate layer, the second peak corresponding to two commensurate layers and so on. The minima occur when the slit-width is incommensurate with respect to formation of layers within the slit. The observed dependence of the mean density on the slit width is in agreement with previously reported data [41]. For a fixed h , $\langle\rho\rangle/\rho_0$ increases with ξ (see inset of Figure 3.2(a)). For low values of ξ, it is observed that $\langle\rho\rangle/\rho_0 < 1$, showing a fluid phase (R) with density rarer than the bulk is stable in the slit at the given chemical potential. As ξ increases beyond ξ_{RD} there occurs a cross-over to a fluid phase (D) denser than the bulk with $\langle\rho\rangle/\rho_0 > 1$. Similar cross-over has been reported for strongly confined water [50].

We examine the detailed structure of the fluid for slit-widths accommodating up to three fluid layers, via the z-density profile, and the average in-plane bond-orientation order parameter Ψ_n as given by Equation (3.5), and (3.6) respectively. n is chosen to be 6, which reflects the rotational symmetry of layer. Ψ_6 takes value 1 if the ordering of fluid particles in the layer has hexagonal symmetry, and is less than 1 otherwise. We show the data for a few representative cases. As seen in Figure 3.2(b)) for $h = 1.9$, there is a single fluid layer and the layer density

increases with ξ. Ψ_6 in the layer (inset, Figure 3.2(b)) shows transition from bond-orientationally disordered fluid phase (F) to an orientationally ordered solid-like phase denoted (S) at $\xi_{FS} = 9$, where ξ_{FS} denotes the asymmetry value for which at least one of the fluid layers within the slit shows the F to S transition. With increasing h, more fluid layers get accommodated within the slit. For a

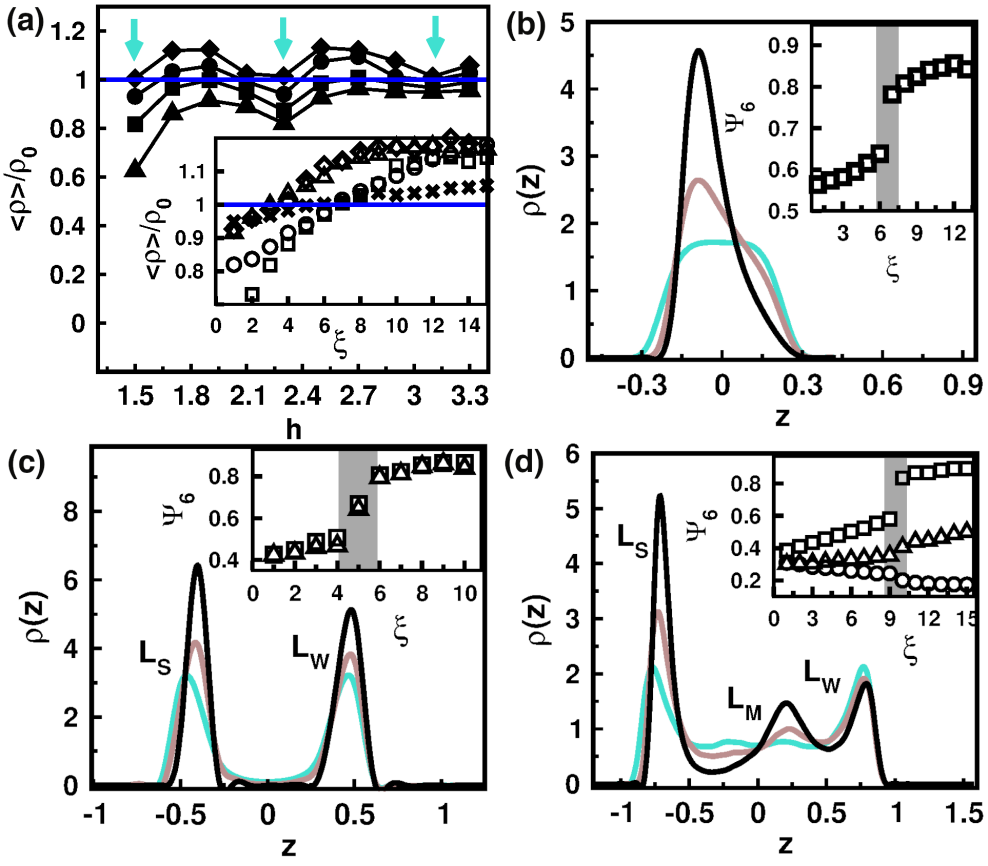

Figure 3.2: (a) Mean fluid density within the slit, as a function of slit-width h , for different values of asymmetry: $\xi = 1$ (triangles), $\xi = 3$ (squares), $\xi = 5$ (circles) and $\xi = 7$ (diamonds). The lines joining the symbols are only guide to the eyes. The arrows indicate the incommensurate slit-widths. Inset shows the effective density as a function of ξ for slit-widths h = 1.5 (squares), h = 1.9 (triangles), h = 2.3 (circles),h = 2.5 (diamonds) and h = 3.1 (crosses). The horizontal line demarcates rarer densities (R) and denser (D) regions, compared to the bulk density. (b), (c) and (d) show respectively the density profiles of fluid along the confinement direction for slits of width h = 1.9, h = 2.5 and h = 3.1, for different values of $\xi = 1$ (cyan), $\xi = 3$ (brown), and $\xi = 7$ (black). The insets show the average bond-orientation order parameter as a function of ξ, for different fluid layers; L_S (squares) L_M (triangles) and L_W (circles), and the shaded strip demarcates the zone of transition.

slit with h = 2.5, the density profile in Figure 3.2(c) reveals two distinct fluid

layers in the slit. We designate as L_S and L_W, the layer adjacent to strongly and weakly attracting wall respectively. The density difference between the two layers reduces as ξ decreases, and as expected, vanishes for ξ = 1. Ψ_6 value (inset Figure 3.2(c)) shows simultaneous cross-over from (F) to (S), for both fluid layers around $\xi_{FS} = 6$. For the case of h = 3.1, the density profile (Figure 3.2(d)) shows three fluid layers within the slit. With increasing asymmetry the layer adjacent to the strongly interacting wall (L_S) shows bond-orientation ordering (F→S), around ξ_{FS} =10, while the layer adjacent to the weakly attracting surface (L_W), and the middle layer (L_M), remain disordered (see inset Figure 3.2(d)). Thus, the entire slit does not show formation of ordered phase but rather a coexistence of solid-like and liquid-like fluid layers.

To gain insights into the fluid structure close to the F→S transition, we examine the decay of spatial correlations of the local bond orientation order given by $G_6(r) = \frac{\langle \psi_6^*(r_j)\psi_6(r_i)\rangle_L}{g(r)}$, where $\psi_6(r_i)$ is the local bond order for the i^{th} particle in layer L, and $g(r)$ is the pair correlation function [51]. $G_6(r)$ is known to exhibit exponential decay for disordered phases and no decay for crystalline phases [52]. As a representative case we show data for the layer L_S, for slit-width h = 2.5. The decay of $G_6(r)$ crosses over from an exponential dependence for $\xi = 4$ as shown in Figure 3.3(a), to a power-law decay, $\sim r^{-\kappa}$ with exponent κ = 0.27 for $\xi = 5$, and finally to a situation with no decay for $\xi = 6$, as shown in Figure 3.3(b).

A power law decay with exponent $\kappa \sim 0.25$ may suggest either a phase having long range bond orientation order but no long range translation order, known as the hexatic phase or a partially ordered state due to phase coexistence [53]. The susceptibility of bond orientation order $\chi_6 = \langle(\Psi_6)^2\rangle$, together with the correlation function, can offer a more definitive picture. While a hexatic structure gives rise to a single peak in bond order susceptibility, a phase coexistence results in double peaks. We calculate the distribution of χ_6 for different sub-sizes of the layer as suggested in [54]. As shown by Figure 3.3(c), the distribution develops

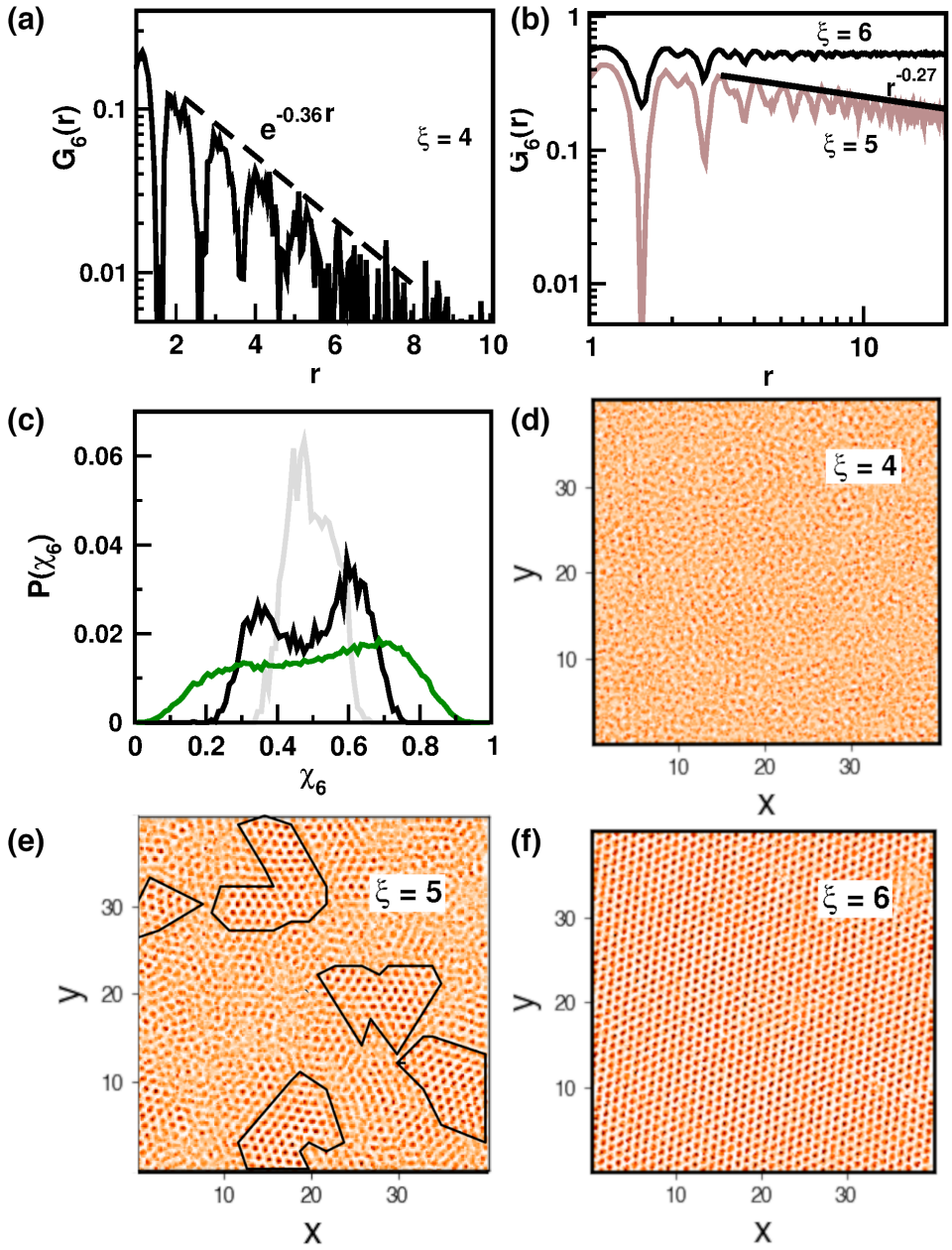

Figure 3.3: (a) $G_6(r)$ (in semi-log scale) for the layer L_S in slit of width h = 2.5 for asymmetry $\xi = 4$. $G_6(r)$ (in log-log scale) for the layer L_S in slit of width h = 2.5, for asymmetry $\xi = 5$ (brown) and $\xi = 6$ (dark). L_W shows similar behavior (not shown). (c) Susceptibility of the bond-orientation order parameter, evaluated close to transition ($\xi = 5$), for subsystems of size $l/2$ (brown), $l/4$ (black) and $l/16$ (green), with $l = 40\sigma_0$. (d), (e) and(f) show in-plane density maps of fluid in layer L_S, for $\xi = 4$, 5 and 6 respectively. Note the ordered (encircled regions) and disordered patches within the layer for $\xi = 5$.

two peaks as subsystem size is reduced. This indicates the coexistence of bond-orientation ordered and disordered patches in the layer, rather than a uniform hexatic phase. The in-plane density plots in Figure 3.3(d), (e) and (f), confirm a disordered fluid layer for $\xi = 4$, coexistence of ordered and disordered patches within the layer for $\xi = 5$ and an ordered layer for $\xi = 6$.

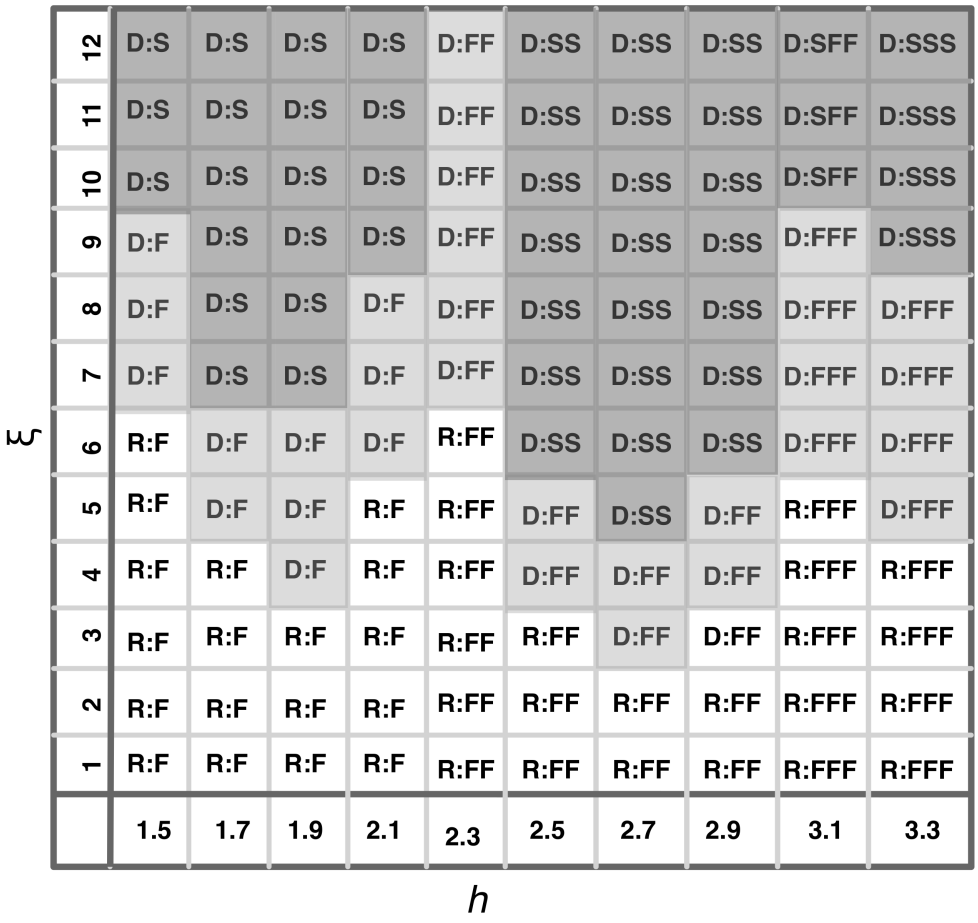

Figure 3.4: Schematic representation of different structural phases of asymmetrically confined LJ-fluid in h -ξ plane. Symbols R and D stand for phases rarer or denser than the bulk phase respectively, while F and S denote bond-orientationally disordered or ordered fluid layers respectively. Dark shading indicates the bond-orientationally ordered phase with density D, the light gray shading is fluid phase with density D, while the unshaded portion is the fluid phase with density R.

The cross-over between structural phases in h -ξ plane is summarized in Figure 3.4. The phases are denoted as follows: The letter to the left of the colon corresponds to the density, while the letters to the right of the colon denote bond-

orientational ordering of the layers, the leftmost letter for L_S and the rightmost for L_W.

3.4.2 Viscoelastic and structural relaxation

We probe the viscoelastic and structural relaxation of the system for different slit widths, as the asymmetry ξ increases, until the F→S transition is encountered ($\xi < \xi_{FS}$). For this we evaluate the stress autocorrelation function (SACF) $C_{\alpha\beta}(t)$, from the MD trajectories of these fluid-like phases. For narrow slit-like geometries such as those considered here, components of the SACF parallel to the confinement direction are not meaningful, due to suppression of stress fluctuations along this direction [47]. We thus consider the compression and shear components of SACF perpendicular to the confinement direction, given respectively by: $C_{\perp,c}(t) = \frac{1}{2}(\langle\delta\sigma_{xx}(t+t_0)\delta\sigma_{xx}(t_0)\rangle_{t_0} + \langle\delta\sigma_{yy}(t+t_0)\delta\sigma_{yy}(t_0)\rangle_{t_0})$ and $C_{\perp,s}(t) = \langle\delta\sigma_{xy}(t+t_0)\delta\sigma_{xy}(t_0)\rangle_{t_0}$ where the subscript c stands for the compressional and s for the shear stress components.

We then obtain the frequency-dependent loss and storage moduli from the Fourier transform of $C_{\perp,\zeta}(t)$, (ζ = c, s) as given by the generalized Green-Kubo relation, Equation (3.7). The integral in Equation (3.7), has an infinite upper time limit which cannot be attained in actual simulations. In practice to evaluate the integral using molecular dynamics simulations data, the infinite upper time limit is replaced with a finite time being the time for which $C_{\perp,\zeta}(t)$ crosses zero for the first time. This ensures that effects of noisy oscillations of the correlations function close to zero are minimized, without loosing details on its decay. Figure 3.5 column (a) shows the decay of the SACF for fluid in a slit of width h = 1.9, for different values of asymmetry. The arrows indicate the time when the correlation function first decays to zero. This time is taken as the upper time

limit in evaluating the generalized Green-Kubo integral. We verify that the zero frequency Green-Kubo integral given by Equation (3.7) with $\omega = 0$, attains a plateau value (which is the static viscosity) for this choice of upper time limit. As shown in Figure 3.5 column (b) the integral attains its plateau value for this choice of cutoff . Further more, the static viscosity $\eta(\omega = 0)$ obtained from the zero frequency Green-Kubo integral, and that obtained from the real part of the Fourier-Laplace transform are in agreement as can be seen by comparing adjacent plots in Figure 3.5 column (b) and (c). A similar approach has been employed by [44, 45] in describing frequency dependent viscosity of 2-D dusty plasma. Elsewhere [55], it has been suggested that effects of long time noisy oscillations of correlation functions may be minimized by smoothly truncating the integral Equation (3.7) with a sum of exponentials, assuming a terminal exponential decay. However this may not be applicable in our case as $C_{\perp,\xi}(t)$ is known to show power law dependence at long times [56].

Figure 3.6(a) and (b) compares the decay of $C_{\perp,c}(t)$ and $C_{\perp,s}(t)$ respectively, for different ξ values, for fluid in a slit of width $h = 1.9$. It is observed that both $C_{\perp,c}(t)$ and $C_{\perp,s}(t)$ show longer decay times as well as higher initial stress in the short-time limit, with increasing ξ. This may be attributed to the decreased mobility of particles as slit asymmetry increases, leading to a slower stress dissipation.

Figure 3.6(c) shows plots of the storage and loss modulus as function of the frequency ω, for a representative case of fluid in a slit of width $h = 1.9$, for two values of the asymmetry $\xi = 1$ and $\xi = 4$. It turns out that in both cases the low frequency response is dominated by the viscous modulus, while the high frequency response is dominated by elastic modulus which is typical behavior for a viscoelastic fluid [44, 16, 57, 45].

There is a well-defined frequency where the two moduli cross each other. The inverse of the frequency value for which $G^S_{\perp,c}(\omega) = G^L_{\perp,c}(\omega)$, is viscoelastic relaxation time denoted by $\tau_{\perp,c}$. Similarly one can define the relaxation time

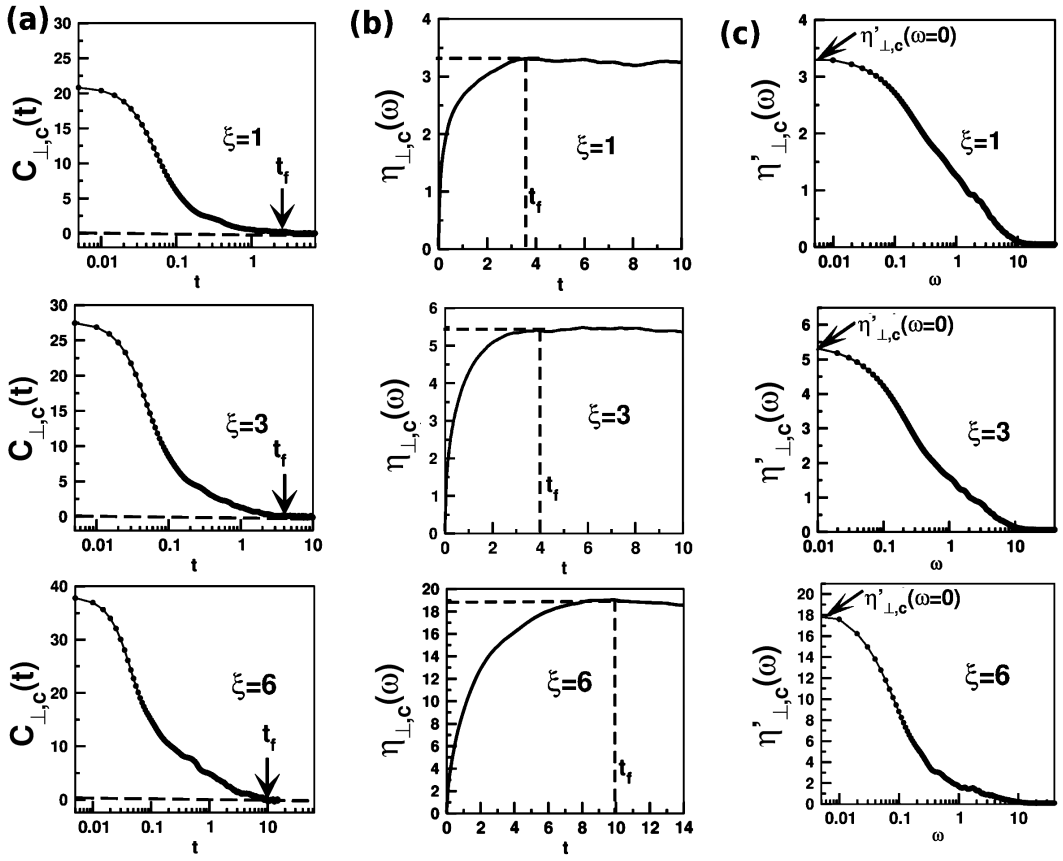

Figure 3.5: Column (a) shows the stress auto-correlation function $C_{\perp,c}(t)$, for fluid in a slit of height $h = 1.9$, for different values of slit asymmetry $\xi = 1$, 3 and 6. The time $C_{\perp,c}(t)$ first reaches zero is marked by t_f. Column (b) shows the Green-Kubo integral for the correlation functions shown in column (a). Notice that the integral reaches its plateau value at time $t = t_f$, marked by the vertical dotted lines. This plateau value is the static viscosity (marked by horizontal dotted lines). Column (c) shows the frequency dependent viscosity evaluated from the generalized Green-Kubo relation, for each of the auto-correlations $C_{\perp,c}(t)$ shown in column (a). The upper time limit used is t_f. Notice that the value of the zero frequency viscosity $\eta_{\perp,c}(\omega = 0)$ here, corresponds to the static viscosity shown in column (b).

for the other viscoelastic components, like relaxation time $\tau_{\perp,s}$ [58] for the shear components. We observe that $\tau_{\perp,c}$ is greater than $\tau_{\perp,s}$ for different slit-widths and asymmetries we consider. The longer timescale $\tau_{\perp,c}$ is taken to describe the viscoelastic relaxation of the system. From Figure 3.6(c) it is also observed that, the cross-over frequency shifts to a lower value and hence to a larger viscoelastic relaxation time, as ξ increases.

In addition to the stress relaxation we also consider the density relaxation

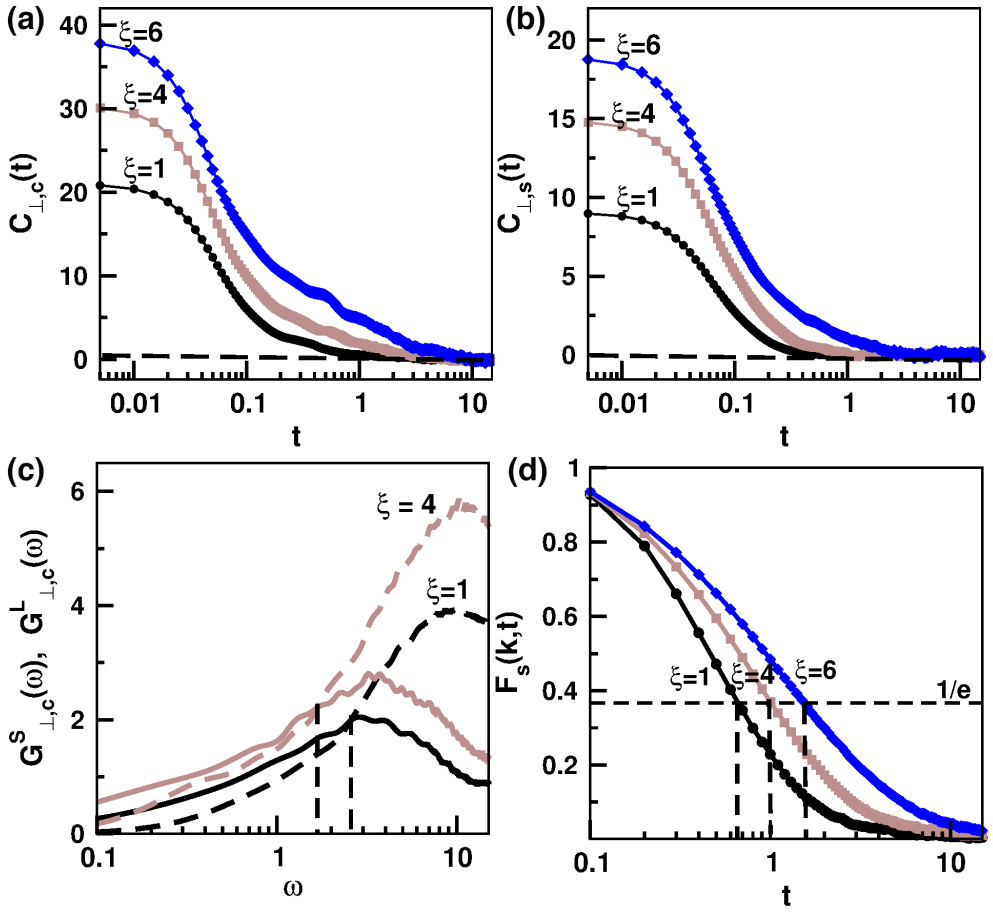

Figure 3.6: (a) Longitudinal and (b) Shear stress auto-correlation for fluid in a slit of width $h = 1.9$, for different ξ values. (c) The loss (solid line) and storage (dotted line) moduli, for fluid in a slit of $h = 1.9$, at two asymmetry values $\xi = 1$ (dark) and $\xi = 4$ (gray). The vertical dotted lines mark the frequency at which the loss modulus is equal to the storage modulus. The inverse of this frequency defines the viscoelastic relaxation time (b) Self- intermediate scattering function for different values of asymmetry, in a slit with slit-width $h = 1.9$. The dotted horizontal line represents $F_s(k;t) = 1/e$ which defines the structural relaxation time (dotted vertical lines).

of the fluid layers. The structural relaxation time for different slit widths and asymmetry values is obtained from the self intermediate scattering function $F_s(k,t)$, with the wave vector k taken perpendicular to the confinement direction [59]. Figure 3.6(d) shows $F_s(k,t)$ for a representative case of fluid in a slit of width $h = 1.9$, for different values of slit asymmetry ξ. The horizontal dotted line marks the point where $F_s(k,t)$ has decayed to $1/e$, from which the structural relaxation time τ_R is defined. $F_s(k,t)$ shows single step decay indicating fluid-like

character [51] of the system, and the relaxation time τ_R is observed to increase with increasing ξ.

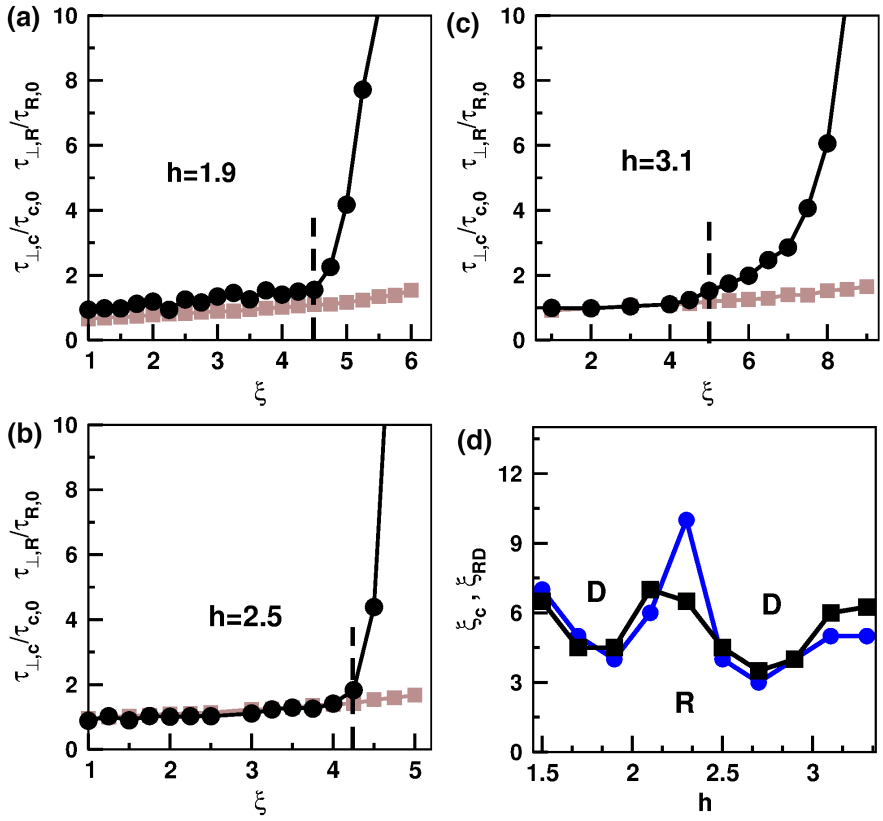

Figure 3.7: (a), (b) and (c) show the viscoelastic relaxation time (circles) and structural relaxation time (squares), for fluid in slits of width $h = 1.9$, $h = 2.5$ and $h = 3.1$ respectively. The dotted vertical lines mark the asymmetry value ($\xi = \xi_c$) for which the viscoelastic relaxation time deviates from the structural relaxation time. (d) ξ_c (squares) and ξ_{RD}(circles)as a function of the slit width. Notice that the profile traced by ξ_c closely matches that of ξ_{RD}.

We show in Figure 3.7(a), (b) and (c) comparison between $\tau_{\perp,c}$ and τ_R, as the asymmetry is varied for slits with $h = 1.9$, 2.5 and 3.1, having one, two and three confined fluid layers respectively. For each slit width, the viscoelastic relaxation time $\tau_{\perp,c}$ is observed to be comparable to the structural relaxation time τ_R, for low ξ. Both relaxation times show only a small variation with increasing ξ up to a critical asymmetry ξ_c (indicated by the vertical dotted line). Beyond ξ_c, the structural relaxation time τ_R keeps increasing slowly with ξ, while the viscoelastic relaxation time $\tau_{\perp,c}$ shows sharp increase, deviating from

the structural relaxation time.

Figure 3.7(d) shows the dependence of ξ_{RD} and ξ_c with h. We find that ξ_c shows oscillatory behavior with increasing h. This oscillatory dependence of ξ_c is found to be driven by the slit commensurabilty. The minima for ξ_c correspond to commensurate, while maxima correspond to incommensurate slit widths, indicating the commensurate slits attain the crossover for lower values of ξ (minima in Figure 3.7(d)), as compared to the incommensurate slits (maxima in Figure 3.7(d)). Similar oscillatory behavior has been reported recently [48] for the static viscosity of nano- confined water between two graphene sheets, and attributed to the fact that fluid layers in commensurate slits show less out of plane diffusivity and hence are greater stability. The second interesting observation is that the variation of ξ_c with increasing h closely matches that of ξ_{RD}, indicating that the deviation of the viscoelastic relaxation time from the structural relaxation accompanies the R $\rightarrow$ D crossover.

3.4.3 Universal behaviour

In order to compare the dependence of $\tau_{\perp,c}$ on the ξ for different slits, it is useful to scale the asymmetry as $q = (\xi - \xi_c)/\xi_c$, such that the crossover corresponds to $q = 0$, for all h. Figure (3.8) shows plots of the $\tau_{\perp,c}$ vs q, for various slit widths. It is observed that the $\tau_{\perp,c}$ data for different h shows a rather universal trend with two distinct dependencies below q = 0 and above q = 0. Note the sharp change of viscoelastic response around q =0 also corresponds to the R to D cross-over. In the (R) phase, i.e $q \leq 0$, $\tau_{\perp,c}$ shows little variation with q for all slit widths, while in the (D) phase $q > 0$, this behavior breaks down and $\tau_{\perp,c}$ increases sharply with increase in q.

The change in the relaxation behavior can be understood by examining the behavior of the individual fluid layers within the slit, as the asymmetry is varied.

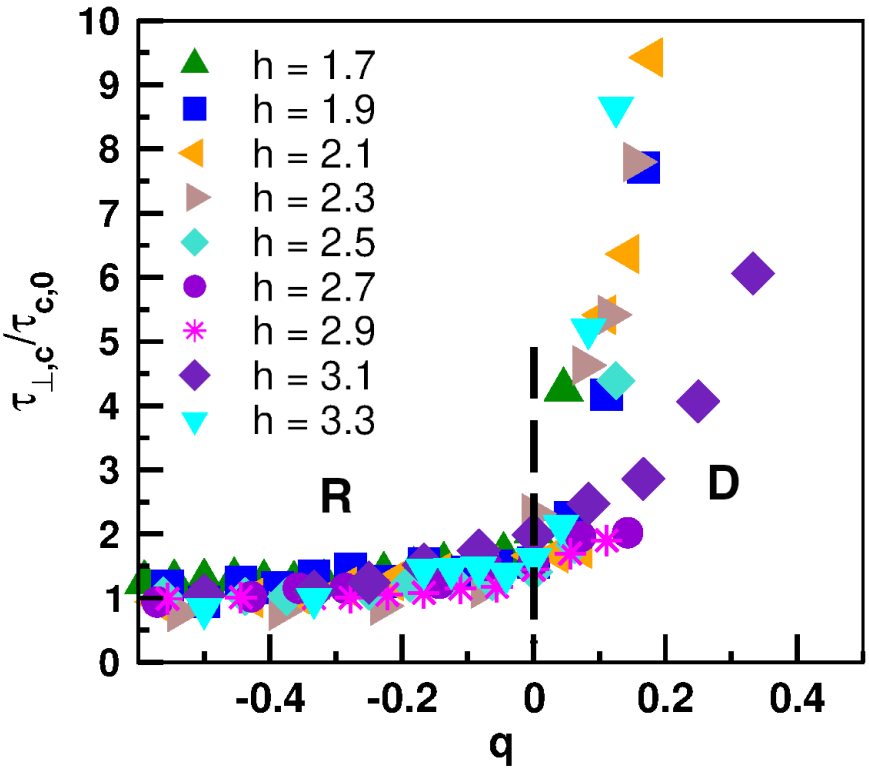

Figure 3.8: Viscoelastic relaxation time as a function of the scaled asymmetry, for different slit widths.

Figure 3.9(a) shows the viscoelastic relaxation time for fluid layers L_S and L_W which are adjacent to the strongly attracting and weakly attracting surfaces respectively for a slit of width h = 2.5, compared with the overall relaxation time of the slit. It is observed that below the critical asymmetry ξ_c, the overall relaxation time of the fluid follows closely that of the fluid layer L_W, while beyond ξ_c, the overall relaxation behavior follows closely that of the layer L_S. The overall viscoelastic relaxation time can be expressed as a weighted average of contributions from individual fluid layers $\tau_{\perp,c} = w_s\tau_{\perp,c}^{L_S} + w_w\tau_{\perp,c}^{L_W}$, where w_s and w_w are the weights of the contribution of L_S and L_W, such that $w_s + w_w = 1$. Figure 3.9(b) shows w_s and w_w for different slit-widths. It is observed that w_s drops to zero from a value close to unity and w_w increases to unity from low values with the cross over near $q = 0$.

Similarly we show in Figure 3.9(c), data for fluid layers L_S, L_M and L_W,

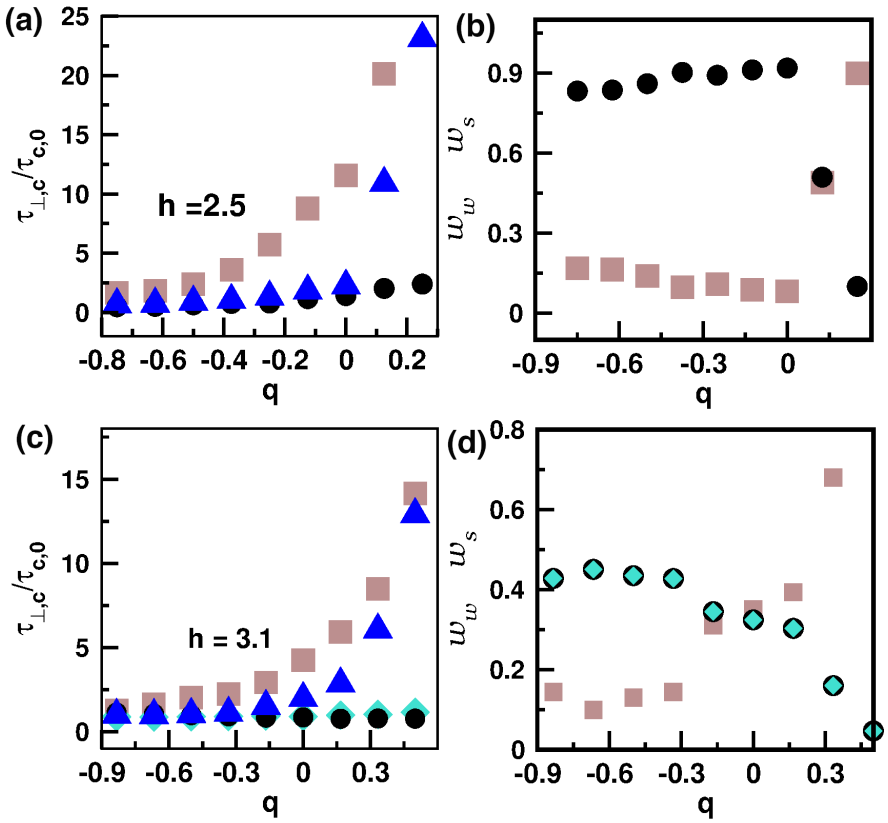

Figure 3.9: (a) Layer resolved local viscoelastic relaxation time for layer L_S (squares) and layer L_W (circles), for fluid in a slit of width h =2.5, compared with the overall viscoelastic relaxation time for the slit (triangles). (b) Weights w_s (squares) and w_w (circles) of the contribution of L_S and L_W respectively, to the overall viscoelastic relaxation time of the slit. (C) Viscoelastic relaxation time of fluid layer L_S (squares) L_M (diamonds) and L_W (circles), in a slit of width h = 3.1, compared with the overall viscoelastic relaxation time of the slit (triangles). (d) Weights w_s (squares) and w_w (diamonds) and w_w (circles) of the contribution of the respective layers L_S, L_M, and L_W, to the overall viscoelastic relaxation time of the slit.

within a slit of width h = 3.1 . L_M and L_W are seen to have a comparable relaxation time as asymmetry varies, while L_S shows slower relaxation. Here again, we write the relaxation time as the layer contribution weighted sum, $\tau_{\perp,c} = w_s\tau_{\perp,c}^{L_S} + w_w\tau_{\perp,c}^{L_M} + w_w\tau_{\perp,c}^{L_W}$, with $w_s + 2w_w = 1$. We assume equal weights (w_w) for L_M and L_W due to their similar relaxation time. Figure 3.9(d) shows the dependence of the weights on the scaled asymmetry q. As observed previously the weights crossover at q= 0, w_w being dominant for q< 0, while w_s having dominant contributions for q> 0. Thus, in the phase (R) with density rarer

than bulk density, the overall viscoelastic relaxation time follows that of the fast relaxing fluid layers, while in the phase (D) with density greater than bulk, the relaxation is dictated by that of the slowly relaxing fluid layer adjacent to the strongly attracting surface, accounting for the universal behavior of the viscoelastic response at different slit widths.

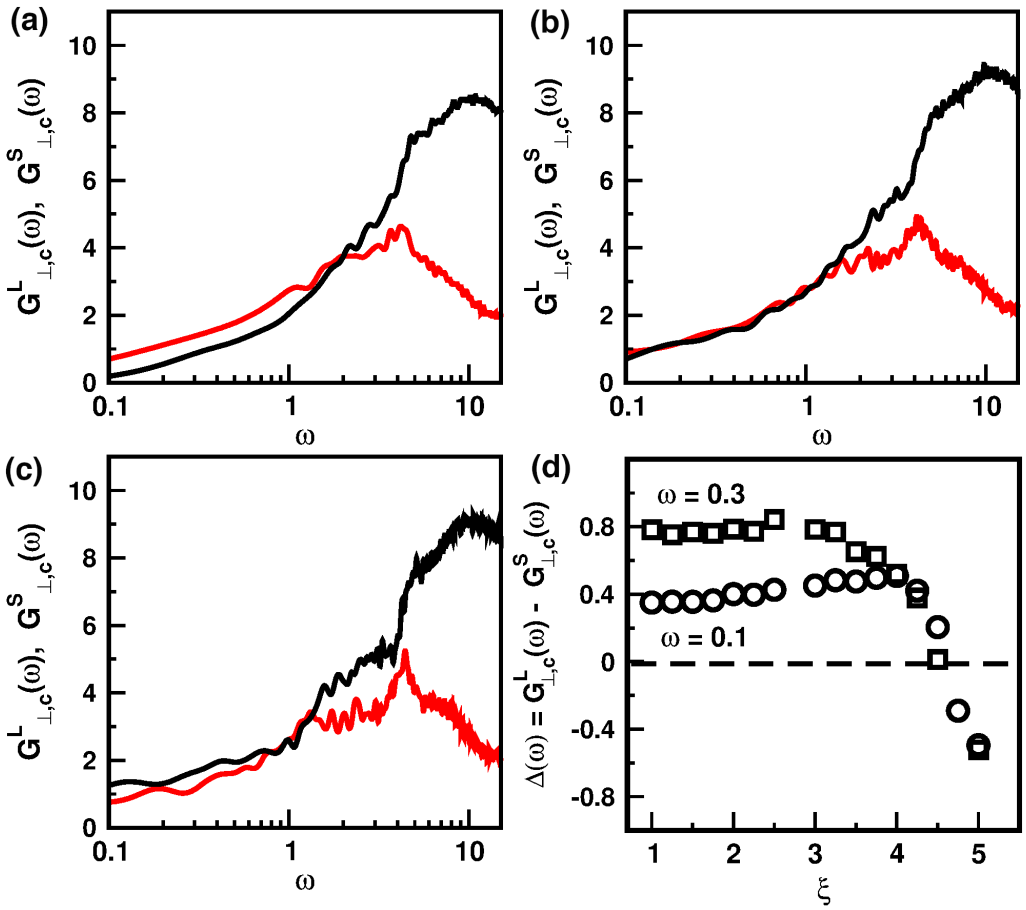

Figure 3.10: (a), (b), (c) show $G^S_{\perp,c}(\omega)$ (black) and $G^L_{\perp,c}(\omega)$ (red) for fluid in slit of width h= 2.5 and $\xi = 4.0$, 4.5 and 5.0 respectively. (d) Variation of $\Delta(\omega = 0.1)$ (circles) and $\Delta(\omega = 0.3)$ (squares) as ξ varies. The dotted horizontal line denotes where the loss and storage moduli become equal

3.4.4 Viscoelastic response close to F→S transition

We consider the viscoelastic response of the fluid in the vicinity of the F→S transition ($\xi \approx \xi_{FS}$). In this regime, as asymmetry increases, the difference between loss $G^S_{\perp,c}(\omega)$ and storage moduli $G^L_{\perp,c}(\omega)$ gradually decreases as ξ approaches ξ_{FS}, till the two moduli overlap for a range of low and intermediate frequency values. This behavior is characteristic of gel-like mechanical response [16, 60]. Eventually $G^S_{\perp,c}(\omega) > G^L_{\perp,c}(\omega)$ indicating onset of purely elastic (solid) response. Such behavior is shown for a representative case of h = 2.5, in Figure 3.10(a), 3.10(b), 3.10(c), for $\xi = 4.0$, $\xi = 4.5$, and $\xi = 5.0$ respectively. The slit contains two fluid layers and both layers show steady increase in Ψ_6 beyond $\xi = 4$, and Ψ_6 saturates after $\xi = \xi_{FS} = 6$ (see Figure 3.2c). The entire region from $\xi = 4$ to $\xi = 6$ thus represents coexistence between bond orientationally disordered and ordered patches as shown through the in-plane density contour map Figure 3.3f. It may be noted that dominant elastic (solid-like) response sets-in in this coexistence region before full orientational ordering is attained. To make this explicit we plot of $\Delta(\omega) = G^L_{\perp,c}(\omega) - G^S_{\perp,c}(\omega)$ vs asymmetry, in Figure 3.10(d), for $\omega = 0.1$ and $\omega = 0.3$. It is observed that Δ for both frequencies goes to zero as the bond orientation order parameter starts growing and changes sign before the F→S transition. Here $\Delta = 0$ corresponds to gel-like mechanical response. Thus, the phase-coexistence region is characterized by gel-like mechanical response which eventually yields to crystal-like elastic response as one moves closer to the transition point.

3.5 Conclusion

To summarize, we study the viscoelastic relaxation of fluid, trapped in a slit formed by two van der Waals walls, having different wettabilities and separated by a gap of a few particle diameters. With increasing slit asymmetry, the fluid

in the slit is observed to go from a phase with density rarer (R) than the bulk density, to one that is denser (D) than bulk. Further increase of the slit asymmetry leads to in-plane ordering with the fluid layers having triangular ordering. In comparison, symmetric slits are observed to show triangular or square ordered frozen phases depending on the commensurability of the slit. For low values of the asymmetry, the viscoelastic relaxation time of the confined fluid is seen to be comparable to its structural relaxation time, up to a critical asymmetry ξ_c beyond which the viscoelastic relaxation increases sharply, deviating from the structural relaxation time. This deviation point ξ_c is observed to correspond with the R $\rightarrow$ D crossover in density, and shows an oscillatory dependence with increasing slit width, driven by the effects of slit commensurability. With respect to the scaled asymmetry q (scaled by the critical value ξ_c) an universal behavior is observed independent of the slit width; for q < 0, viscoelastic relaxation time shows little variation with increasing q, meanwhile this behavior breaks down for q> 0, with viscoelastic relaxation time showing a sharp increase as q increases. On the other hand in the vicinity of the F $\rightarrow$ S transition, an overlap of the viscous and elastic response over a range of intermediate frequencies is observed, suggesting gel-like viscoelastic behavior. The elastic response eventually becomes dominant as the long ranged orientation order sets in at ξ_{FS}. Physically this universal behavior is driven by the fact that below the crossover, the overall viscoelastic relaxation of the fluid within the slit is determined by the fast relaxing layers close to the weakly attracting surface, whereas beyond the crossover point, the relaxation is dominated by that of the dense fluid layer adjacent to the strongly attracting surface. The gel-like viscoelastic response can be attributed to coexistence of ordered and disordered phases in the fluid film. We expect a qualitatively similar scenario for other wall-fluid models, provided asymmetry is sufficiently strong. For example, it has previously been shown [61] that the thermodynamic, dynamic, and structural properties of fluids

confined by purely repulsive walls, as well as Weeks-Chandler-Andersen (WCA) type wall-fluid models [62, 63], are qualitatively similar to those for a system with a pure LJ attractive walls. Our findings may be important for interpreting results of nano-rheological measurements for a variety of systems, from molecular fluids under strong confinement in nano-meter sized slits , to macromolecular dispersions in micrometer channels.

References

[1] A. C. de Moraes, *et al.*, *Advanced Functional Materials* **29**, 1902245 (2019).

[2] X. Wu, X. Xu, C. Guo, H. Zeng, Metal oxide heterostructures for water purification (2014).

[3] T. Liu, X. Liu, N. Graham, W. Yu, K. Sun, *Journal of Membrane Science* **593**, 117431 (2020).

[4] M. Nazari, A. Davoodabadi, D. Huang, T. Luo, H. Ghasemi, *ACS nano* **14**, 16348 (2020).

[5] M. K. Borg, J. M. Reese, *Mrs bulletin* **42**, 294 (2017).

[6] S. Sun, C. Liao, A. M. Hafez, H. Zhu, S. Wu, *Chemical Engineering Journal* **338**, 27 (2018).

[7] V. Augustyn, Y. Gogotsi, *Joule* **1**, 443 (2017).

[8] Zhang, *et al.*, *Bioactive Materials* **5(4)**, 1071 (2020).

[9] J. K. Patra, *et al.*, *Journal of nanobiotechnology* **16**, 71 (2018).

[10] E. Tendong, T. S. Dasgupta, J. Chakrabarti, *Journal of Physics: Condensed Matter* **32**, 325101 (2020).

[11] D. Munoz-Santiburcio, D. Marx, *Chemical Reviews* (2021).

[12] R. Karnik, *et al.*, *Nano letters* **5**, 943 (2005).

[13] R. Karnik, C. Duan, K. Castelino, H. Daiguji, A. Majumdar, *Nano letters* **7**, 547 (2007).

[14] S.-J. Liang, B. Cheng, X. Cui, F. Miao, *Advanced Materials* **32**, 1903800 (2020).

[15] K. Novoselov, o. A. Mishchenko, o. A. Carvalho, A. C. Neto, *Science* **353** (2016).

[16] R. Khare, J. de Pablo, A. Yethiraj, *The Journal of Chemical Physics* **114**, 7593 (2001).

[17] T.-D. Li, E. Riedo, *Physical review letters* **100**, 106102 (2008).

[18] M. Ramaswamy, *et al.*, *Physical Review X* **7**, 041005 (2017).

[19] P. Peyla, C. Verdier, *EPL (Europhysics Letters)* **94**, 44001 (2011).

[20] K. Voïtchovsky, *Nanoscale* **8**, 17472 (2016).

[21] J. K. Holt, *et al.*, *Science* **312**, 1034 (2006).

[22] M. P. Goertz, J. Houston, X.-Y. Zhu, *Langmuir* **23**, 5491 (2007).

[23] M. Barisik, A. Beskok, *Microfluidics and Nanofluidics* **11**, 269 (2011).

[24] Z. Sun, Y. Kang, *Physics Letters A* **378**, 1739 (2014).

[25] Z.-L. Sun, Y.-S. Kang, Y.-M. Kang, *Chinese Physics B* **28**, 036102 (2019).

[26] Z. Sun, Y. Kang, Y. Kang, *Industrial and Engineering Chemistry Research* **58**, 15637 (2019).

[27] S. Yamada, *Tribology Letters* **13**, 167 (2002).

[28] D. Wilms, N. B. Wilding, K. Binder, *Physical Review E* **85**, 056703 (2012).

[29] K. Umeda, K. Kobayashi, T. Minato, H. Yamada, *Physical Review Letters* **122**, 116001 (2019).

[30] C. Sendner, D. Horinek, L. Bocquet, R. R. Netz, *Langmuir* **25**, 10768 (2009).

[31] D. Ortiz-Young, H.-C. Chiu, S. Kim, K. Voïtchovsky, E. Riedo, *Nature communications* **4**, 1 (2013).

[32] A. Malani, K. Ayappa, *Molecular Simulation* **38**, 1114 (2012).

[33] X. Zhang, Y. Zhu, S. Granick, *Science* **295**, 663 (2002).

[34] C.-Y. Lee, J. A. McCammon, P. Rossky, *The Journal of chemical physics* **80**, 4448 (1984).

[35] H. Zhang, *et al.*, *Physical Review E* **89**, 032412 (2014).

[36] J. Rickman, *Physical Review E* **86**, 062501 (2012).

[37] T. S. Ingebrigtsen, J. R. Errington, T. M. Truskett, J. C. Dyre, *Physical review letters* **111**, 235901 (2013).

[38] M. P. Allen, D. J. Tildesley, *Computer simulation of liquids* (Oxford university press, 2017).

[39] E. Ustinov, *The Journal of chemical physics* **147**, 014105 (2017).

[40] M. Miyahara, K. E. Gubbins, *The Journal of chemical physics* **106**, 2865 (1997).

[41] A. Vishnyakov, A. V. Neimark, *The Journal of chemical physics* **118**, 7585 (2003).

[42] S. Plimpton, Fast parallel algorithms for short-range molecular dynamics, *Tech. rep.*, Sandia National Labs., Albuquerque, NM (United States) (1993).

[43] Y. Noh, T. Vo, B. Kim, *Applied Sciences* **9**, 2439 (2019).

[44] Z. Donkó, J. Goree, P. Hartmann, *Physical Review E* **81**, 056404 (2010).

[45] Y. Feng, J. Goree, B. Liu, *Physical Review E* **85**, 066402 (2012).

[46] N. Kuon, A. A. Milischuk, B. M. Ladanyi, E. Flenner, *The Journal of chemical physics* **146**, 214501 (2017).

[47] S. Krishnan, K. Ayappa, *Physical Review E* **86**, 011504 (2012).

[48] M. Neek-Amal, F. M. Peeters, I. V. Grigorieva, A. K. Geim, *ACS nano* **10**, 3685 (2016).

[49] B. H. Kim, A. Beskok, T. Cagin, *Microfluidics and nanofluidics* **9**, 31 (2010).

[50] K. Nomura, *et al.*, *Proceedings of the National Academy of Sciences* **114**, 4066 (2017).

[51] J.-P. Hansen, I. R. McDonald, *Theory of simple liquids* (Elsevier, 1990).

[52] Y.-W. Li, M. P. Ciamarra, *Physical Review E* **102**, 062101 (2020).

[53] N. Gribova, A. Arnold, T. Schilling, C. Holm, *The Journal of chemical physics* **135**, 054514 (2011).

[54] K. J. Strandburg, J. A. Zollweg, G. Chester, *Physical Review B* **30**, 2755 (1984).

[55] A. V. Straube, B. G. Kowalik, R. R. Netz, F. Höfling, *Communications Physics* **3**, 1 (2020).

[56] M. Hagen, C. Lowe, D. Frenkel, *25 Years of Non-Equilibrium Statistical Mechanics* (Springer, 1995), pp. 240–249.

[57] Y. Feng, J. Goree, B. Liu, *Physical review letters* **105**, 025002 (2010).

[58] D. J Evans, G. P Morriss, *Statistical mechanics of nonequilbrium liquids* (ANU Press, 2007).

[59] E. Flenner, G. Szamel, *Proceedings of the National Academy of Sciences* **116**, 2015 (2019).

[60] H.-C. Tseng, J.-S. Wu, R.-Y. Chang, *Physical Chemistry Chemical Physics* **12**, 4051 (2010).

[61] P. Kumar, F. W. Starr, S. V. Buldyrev, H. E. Stanley, *Physical Review E* **75**, 011202 (2007).

[62] D. M. Heyes, H. Okumura, *The Journal of chemical physics* **124**, 164507 (2006).

[63] J. R. Bordin, A. B. de Oliveira, A. Diehl, M. C. Barbosa, *The Journal of chemical physics* **137**, 084504 (2012).

Chapter 4 Dynamics of water trapped in metal oxide-graphene nano-confinement *

4.1 Introduction

In the preceding chapter, we have explored the phase behavior and viscoelatic properties of a model fluid confined by structureless walls having unequal wettability. We have shown that the confined fluid exhibits a rich phase behavior as well as viscoelastic response driven by the confinement asymmetry. An example of confined fluid which is ubiquitous both in nature and in industry, is confined water [1]. Nano confined water has been in observed in systems ranging from cavities in biological macromolecules [2] to mesoporous rock formations [3]. The structure and phase behavior of water confined by symmetric hydrophobic walls like carbon nano slits [4, 5, 6], graphene oxide membranes [7] and graphene bi-layers [8], or hydrophilic confinements like zeolites [9], nano porous silicates [10] and titania surfaces [11, 12, 13] have been substantially explored in recent research [5, 6, 7, 10, 11].

Following the newly discovered 2D materials like graphene, attempts have been made to bring this emerging class of materials in contact with another

*This Chapter is based on the following publication:
E. Tendong, T. Saha Dasgupta, and J. Chakrabarti. Journal of Physics: Condensed Matter 32 (2020): 325101.

important class of materials, namely transition metal oxides (TMO), to form heterostructures with attractive application possibilities[14, 15, 16, 17]. In particular, graphene supported on TiO_2 has been considered in many such applications. For example, gated graphene-on-TiO_2-terminated $SrTiO_3$ (STO) field effect transistor has been successfully fabricated and characterized [18, 19]. In such devices ferroelectric-like surface dipoles on TiO_2 surface of STO, formed due to off-centric movement of Ti atoms, are found to give rise to large intrinsic polarization which gets probed by graphene [19]. A complete understanding of the synergistic interaction between graphene and TMO is necessary to broaden potential applications of graphene/TMO heterostructures. Since wet chemical methods are used to synthesize these heterostructures, graphene-TMO interaction is mediated by the water trapped in the process [20]. Water mediated interactions have also been shown to play key roles in diffusion and transport characteristics of guest molecules within narrow confinements, with important implications for microfluidic [21] and drug delivery applications [22]. It is, therefore, crucially important to understand the static and dynamic behaviour of trapped water at the metal oxide - graphene interface.

We note that the TiO_2 surface is polar (hydrophilic) and graphene is non-polar (hydrophobic), giving rise to an asymmetric confinement. Few investigations have looked into the structural properties of asymmetrically confined water [23, 24, 25]. However, the relaxation dynamics of water within such confinements has remained unexplored to a large extent to the best of our knowledge.

Armed with a general understanding of the structure of asymmetrically confined fluids from Chapter 3, in the current chapter we employ atomically detailed force-field MD simulations, to study the dynamics of water confined in an asymmetric slit, consisting of a graphene over-layer on the TiO_2 terminated (001) STO surface at room temperature. Here the detailed arrangement of atoms in the confining surfaces is considered. The forcefield parameters used are design

to reproduce the experimentally observed properties of the atoms being modeled. The atomistically detailed approach also allows us to explore the influence of arrangement of wall atoms on confined fluid. Following our investigation in Chapter 3, we focus on the strong confinement limit where the effects of both confining surfaces are experienced by water molecules in the slit. We find that there is a strongly pinned water layer at the STO surface, which shields the rest of water in the slit from hydrophilic effects of the surface. The translational and rotational dynamics of water molecules show heterogeneity due to coupling of slow relaxing and strongly pinned hydration layer over STO surface, with faster subsequent water layers. The nature of the dynamic heterogeneity is characterized through various correlation functions, as well as effective free energy landscape experienced by the water molecules in each water layer. We find that asymmetric slit may be exploited in the design of implantable drug delivery devices.

4.2 Computational details

4.2.1 Water model

Though the structure of water appears relatively simple, the development of a molecular model that reproduces all the known properties of water has so far remained elusive. In liquid water, each molecule is unique in the sense that its properties strongly depend on the arrangement of the other water molecules around it. The very small mass of the water hydrogen atoms also makes it difficult to properly represent them by a classical model. The main goal of good water models is usually to reproduce correctly the known properties of water and be able to predict new behavior, while remaining simple. Common explicit water models can be grouped into polarisable and rigid models. Polarisable

models represent the water molecule as balls on springs with bonds and angles allowed to fluctuate. These models reproduce well the vibrational and absorption spectrum of water, but perform poorly in determining the phase behavior of water [26]. Rigid models represent the water molecule like a ball and stick structure, employing fixed bond lengths and bond angles. Examples include the simple point charge (SPC) model [27] and the transferable intermolecular potential (TIPxP) models where x = 3,4,5 [28]. Polarisation in these models is implicit with the oxygen atom being accorded a negative partial charge and the hydrogen atoms having a positive partial charge in such a way that the charge of the molecule remains neutral. Extra dummy atoms in the TIPxP models, are used to better represent the charge distribution on the water molecule, as shown in Figure 4.1 for TIP4p-ew [29, 30] and TIP5p-ew [31] water models.

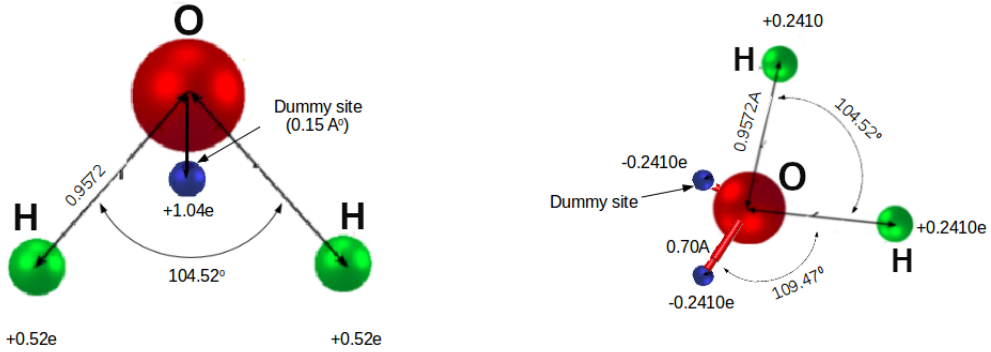

Figure 4.1: A representation of the TIP4P/ew (left) and TIP5P/e (right) water models (Figure adapted from Ref. [32]).

For modeling interactions of water at oxide surfaces, polarisable water models have been shown to under-predict transport properties and over-predict orientational order of water [26]. With charge scaling and proper treatment of electrostatic interactions, rigid models have been shown to predict correctly, the electrostatic solvation energies and structure of water at oxide surfaces [33]. In a comparative bench-marking [34] of different non-polarisable water models, the TIP4P-ew model has been shown to give the best overall predictions of water

properties under different thermodynamic conditions. Hence, we employ the TIP4P-ew [35] water model in which the effects of polarisation are included in an implicit fashion, and we use the shake algorithm [36] to restrain the water bond lengths and bond angles. This model is optimized for use with the Ewald summation technique of treating long range electrostatic interactions, and has been shown to accurately reproduce water properties over a wide range of thermodynamic conditions [37].

4.2.2 $SrTiO_3$ - water interaction model

For modeling the STO lattice and STO-water interactions, we use force-field parameters reported in [38]. This set developed from fitting experimental properties and results of *ab-initio* calculations, has been shown to accurately predict properties of STO-water interface [38, 39]. Ion-ion interactions in the STO slab follow the Buckingham potential [40] given by Equation (4.1), while STO-water interactions are of LJ type given by Equation (4.2):

$$U_{BH}(r_{ij}) = A_{ij} exp\left(\frac{-r_{ij}}{b_{ij}}\right) - \frac{C_{ij}}{r_{ij}^6}\,, \tag{4.1}$$

$$U_{LJ}(r_{ij}) = 4\epsilon_{ij}\left[\left(\frac{\sigma_{ij}}{r_{ij}}\right)^{12} - \left(\frac{\sigma_{ij}}{r_{ij}}\right)^{6}\right] \equiv \frac{A'}{r^{12}} - \frac{C'}{r_{ij}^6}. \tag{4.2}$$

The interaction parameters A_{ij}, b_{ij}, C_{ij}, A'_{ij}, and C'_{ij} for each atom pair (i,j) in Equation (4.1) and (4.2), are summarized in Table 4.1 and Table 4.2

4.2.3 Graphene - water interaction model

The interaction of water with graphene and carbon nanotubes has been widely explored. In our investigations, carbon-carbon and water-carbon interactions are modeled by the LJ potential, with the interaction parameters adapted from [41].

Table 4.1: Buckingham potential parameters for bulk STO. The ions have partial charges : Sr = +1.720, Ti = +2.339, O_{slb} = -1.353. (O_{slb} is the oxygen atom of the STO slab).

Atom pair (i,j)	A_{ij} $(kJmol^{-1})$	b_{ij} (Å)	C_{ij} $(kJmol^{-1}Å^6)$
Ti-Sr	547164	0.29	521
Ti-O_{slb}	664489	0.22	868
Sr-O_{slb}	211977	0.30	2509
O_{slb}-O_{slb}	168752	0.30	5229

Table 4.2: Lennard-Jones 12-6 potential parameters for STO-water and graphene-water interactions. (O_w is the oxygen atom of water).

Atomic pair	$A'_{ij}(kJmol^{-1}$ Å$^{12})$	$C'_{ij}(kJmol^{-1}Å^6)$
Sr-O_w	816491.0	0.00
Ti-O_w	54262.9	0.00
$O_{slb}O_w$	2479730	3502.40

The carbon atoms of the graphene sheet are weakly restrained at their positions by a harmonic potential of force constant 1000 kJ mol^{-1}nm^{-2}. Table 4.3 shows the interaction parameters for carbon-carbon and carbon-water interactions used in our work.

Table 4.3: Lennard-Jones 12-6 potential parameters for carbon-carbon and carbon-water interactions. (O_w is the oxygen atom of water).

Atomic pair	$A'_{ij}(kJmol^{-1}$ Å$^{12})$	$C'_{ij}(kJmol^{-1}Å^6)$
C - O_w	1104288.91	998.39
C - C	18706817.03	5735.33

4.2.4 MD simulation details

Figure 4.2 shows a schematic of the simulation box. An STO slab and a graphene layer are placed at a separation h along the z direction in a box of height 10 nm, with a vacuum layer of height $h_v = (10 - h)/2$ nm at both ends. The entire box is repeated periodically in all three spatial directions. The relaxed STO slab is taken from DFT calculations reported in [19], and has dimensions 4.73 nm by 4.73 nm, with 144 (12x12) surface unit cells of lattice constant 0.39 nm. The slab consists of

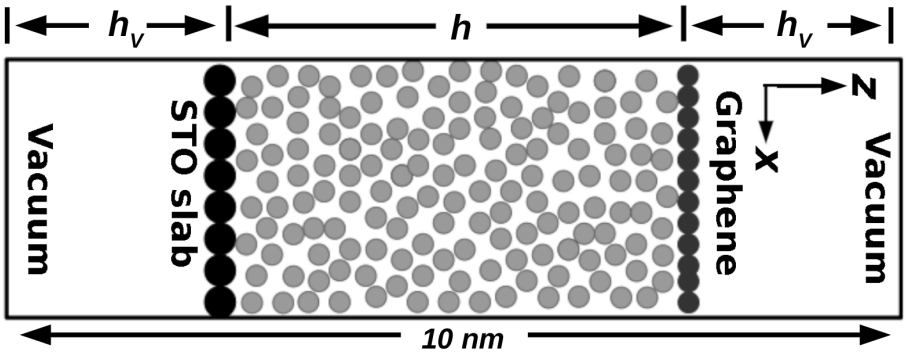

Figure 4.2: Schematic representation of the simulation cell.

5 alternating atomic planes of SrO and TiO_2, terminating at the TiO_2 layer along the [001] direction. The two bottom layers of the STO slab are restrained by a harmonic potential of force constant 1000kJ/mol nm^{-2}, to mimic the effects of the rest of the bulk crystal lattice. Simulations are performed for different values of the confinement width h ranging from 1 nm to 5 nm at constant temperature of 300K and constant volume, using the Gromacs-4.6.5 software package [42]

Within nanometre size confinements, the effective volume accessible to water molecules is smaller than the total available geometric volume . For a slit with separation h, the effective slit width h' available to the water can be estimated as [8]: $h' \approx h - \left[\frac{\sigma_1+\sigma_2+2\sigma_{ow}}{4}\right]$, where σ_1 and σ_2 are the Lennard Jones (LJ) radii of carbon and titanium atoms respectively, and σ_{ow}, is the LJ radius of water oxygen atoms. The effective density of the liquid within the slit it then given by $\rho' = N/v'$, where N is the number of water molecules, and $v' = L_x \times L_y \times h'$ is the effective volume. The effective density of water within each of the slits is kept constant. The number of water molecules considered within each of the slits and the corresponding geometric and effective densities are shown in Table 4.4. Each simulation consists of a 20 ns equilibration, followed by a 50 ns production run. The Verlet algorithm is used for integrating the equations of motion with a time step of 1 fs, and the system configuration is saved periodically at intervals of 1 ps.

Table 4.4: Water effective and geometric densities used for each the simulations

Slit width h (nm)	No. of atoms N	Eff. Density ρ' (g/cm^3)	Density ρ (g/cm^3)
5	3500	0.997	0.937
4	2755	0.997	0.922
3	2011	0.997	0.897
2	1265	0.997	0.846
1.5	894	0.997	0.798
1.2	670	0.997	0.747
1	521	0.997	0.696

4.2.5 Simulation with oleic acid

To investigate the dynamics of guest molecules in the slit, we consider a 3% w/w oleic acid water mixture [43], within 2 nm wide STO-graphene, and 2 nm wide STO-STO nano slits. The oleic acid is modeled via all-atom force field parameters taken from the GROMOS 54A7 [44] force field, and its interaction parameters with STO and graphene are calculated via the Lorentz-Berthelot mixing rules as discussed in chapter 2. The simulations are carried out at a constant volume, and the temperature is kept fixed using the Nose-Hoover thermostat. Each simulation consists of a 20 ns equilibration, followed by a 20 ns production run during which system snapshots are saved at intervals of 2 ps.

4.3 Analysis

As shown in Chapter 3, fluids confined in narrow slits exhibit a layered structure. We analyze the the structure and dynamic of each water layer using the following quantities:

(a) Residence time correlation: The residence time correlation for water molecules in a layer is given by:

$$C_T(t) = \left\langle \frac{1}{N_l(t_0)} \sum_{i=1}^{N} \left(\prod_{t'=t_0}^{t_0+t} \Theta_i(t') \right) \right\rangle_{t_0} , \tag{4.3}$$

where $\Theta_i(t') = 1$ if $z_a \leq z_i(t') < z_b$ and 0, otherwise. z_a and z_b define the lower and upper boundaries of the water layer along the z direction while z_i is the z coordinate of the ith water molecule. $N_l(t_0) = \sum_{i=1}^{N} \Theta_i(t_0)$ is the number of molecules in the layer at a time t_0, and $\langle \cdots \rangle_{t_0}$ represents an average over different time origins in the equilibrated portion of the trajectory.

(b) Reorientation time correlation: The rotational relaxation of water molecules in a layer is captured through the second order orientation time correlation given by:

$$C_R(t) = \left\langle \frac{1}{N_l(t)} \sum_{i=1}^{N} \left\{ P_2 \left[\hat{u}_i(t_0) \cdot \hat{u}_i(t_0 + t) \right] \prod_{t'=t_0}^{t_0+t} \Theta_i(t') \right\} \right\rangle_{t_0}, \tag{4.4}$$

where P_2 is the second Legendre polynomial and $\hat{u}_i(t)$ is the unit vector parallel to the dipole moment vector of the ith water molecule. In equation (4.4), $N_l(t) = \sum_{i=1}^{N} \prod_{t'=t_0}^{t_0+t} \Theta_i(t')$, is the number of water molecules that remains within the water layer throughout the time interval t_0 to $t_0 + t$.

(c) Self van Hove function: As introduced in Chapter 2, the self van Hove function (self-vHf) for a two dimensional water layer can be written as [45]:

$$\begin{aligned} G_\xi(\xi, z_a, z_b, \Delta t) = & \left\langle \left(\frac{1}{N_l(\Delta t)} \right) \right. \\ & \left. \times \sum_{i=1}^{N} \left\{ \delta(\xi - |\vec{\xi}_i(t_0 + \Delta t) - \vec{\xi}_i(t_0)|) \prod_{t'=t_0}^{t_0+\Delta t} \Theta_i(t') \right\} \right\rangle_{t_0} \end{aligned} \tag{4.5}$$

where $G_\xi = (G_T, G_R)$ for translation and rotation respectively. z_a and z_b define the boundaries of the water layer. For the translational self-vHf, $\vec{\xi}_i = \vec{r}_\perp^{\,i}$ is the projection of the particle positions on a plane perpendicular to the confinement direction. G_T is measurable via neutron scattering experiments [46]. In equation (4.5), $N_l(\Delta t)$ and $\Theta_i(t')$ have the same meaning as defined in equation (4.4). For the rotational motion, $\vec{\xi}_i = \vec{\phi}_i(t)$, where the rotational trajectory $\vec{\phi}_i(t)$ is

defined as [47]:

$$\vec{\phi}_i(t) = \int_{t_0}^{t_0+t} \delta\vec{\phi}_i(t')dt'. \tag{4.6}$$

$\delta\vec{\phi}_i(t)$ represents the rotational displacement of a water molecule over a time interval δt, and has magnitude $cos^{-1}[\hat{u}_i(t)\cdot\hat{u}_i(t+\delta t)]$ and direction $\hat{u}_i(t)\times\hat{u}_i(t+\delta t)$, with $\hat{u_i}(t)$ being the unit vector parallel to the ith water molecule dipole moment vector. The coarse graining time δt is chosen to be greater than the libration time of the water molecules.

(d) Mean squared displacement: The in-plane translational and rotational mean squared displacement (MSD) of water molecules in a layer, can be written as:

$$\left\langle \Delta\xi^2(t) \right\rangle = \left\langle \frac{1}{N_l(t)} \sum_{i=1}^{N_l} \left\{ |\Delta\vec{\xi}_i(t)|^2 \prod_{t'=t_0}^{t_0+\Delta t} \Theta_i(t') \right\} \right\rangle_{t_0}. \tag{4.7}$$

For translational motion $|\Delta\vec{\xi}_i(t)|^2 = |\Delta\vec{r}^{\,i}_{||}(t)|^2 = |x_i(t_0+t) - x_i(t_0)|^2 + |y_i(t_0+t) - y_i(t_0)|^2$, with x_i and y_i being the coordinates of the ith water molecule, and for rotational motion, $|\Delta\vec{\xi}_i(t)|^2 = |\Delta\vec{\phi}_i(t)|^2$. The diffusion coefficient is given by $D_\xi = \lim_{t\to\infty} \langle\Delta\xi^2(t)\rangle / 4t$. As before only water molecules that remain within the layer throughout the time interval t_0 to $t_0 + t$ are considered.

4.4 Results and Discussions

4.4.1 Structure of confined water

We start by examining the density profile of water in asymmetric nanoconfinement on which our dynamical studies have been carried out. Perpendicular to the surface of a single graphene or STO, water density profile shows variations which extend up to a distance of thrice the molecular diameter (~ 1 nm) from the

surface (Figure 4.3(a)). We mainly focus on the strong confinement limit where the two confining surfaces are separated by twice this distance or less. Figure 4.3(b) shows density profiles of water in 1 nm wide symmetric (graphene-graphene and STO-STO) and asymmetric (STO-graphene) nano-slits. It is observed that two symmetrically placed graphene walls repel water molecules to create a double peaked structure of water, while two symmetric STO walls create two strongly adsorbed layers in their vicinity. When one of the STO walls is replaced by graphene, the density in the layer close to graphene (L_G, between z_0 and z_1) gets depleted compared to that in the symmetric graphene confinement. As a result, an additional layer appears in the middle (L_M, between z_1 and z_2), along with a strongly adsorbed layer (L_S, between z_2 and z_3) near STO surface, similar to that in the symmetric STO confinement. In effect, the hydrophobicity of graphene gets enhanced by the proximity of STO. At the same time, the hydrophilicity of STO wall gets screened by the adsorbed water layer in its vicinity as observed earlier for water on metal surface [48]. This makes the slit effectively hydrophobic, bounded by the hydrated STO and the graphene surface.

Strong orientational ordering is observed in L_S as shown in the inset of Figure 4.3(b). The dipole moment vectors of water molecules within this layer tend to align preferentially at angles of $\theta = 0^o, 110^o$ and 150^o to the STO surface normal. In L_M the preferred orientation is $\theta = 60^o$, while in L_G no preferred orientation of the water molecules is observed. Having an understanding of the structure, we next probe the translational and rotational dynamical properties of the water layers.

4.4.2 Time Correlation functions

The dynamics of water layers are characterized through the analysis of various time correlation functions $C_\xi(t)$ ($\xi = T$ and R for translation and rotation, respectively). We first consider the residence time correlation function $C_T(t)$,

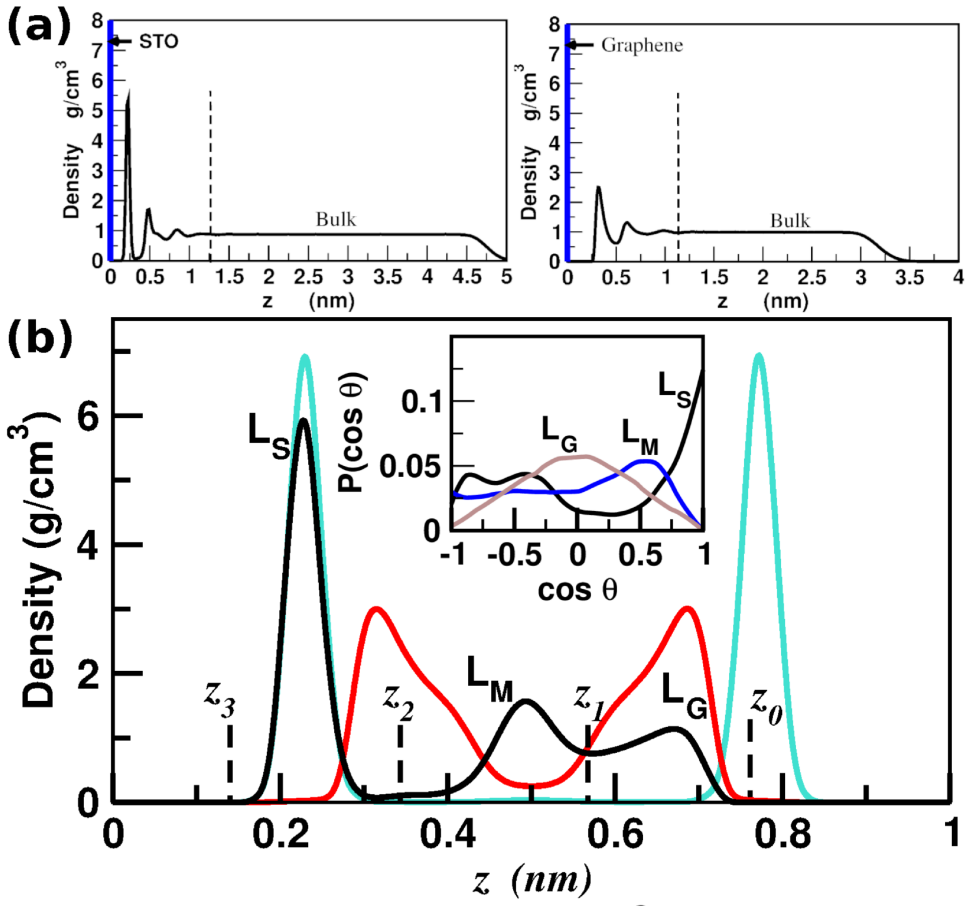

Figure 4.3: (a) Density profile of water close to single STO surface (left) and graphene (right). The dotted lines show where the density oscillations stop and bulk-like density starts. (b) Equilibrium density profile of water across the 1 nm nano-slit of graphene-STO (black) in comparison to graphene-graphene (red/dark grey) and STO-STO (cyan/light grey). See text for details. The inset shows orientations of water dipole moment vectors in L_S, L_M and L_G with respect to STO surface normal.

as defined in Equation (4.3). $C_T(t)$ gives the probability that a water molecule stays in a given layer for a time length t, and the decay rate of $C_T(t)$ gives the mean residence time of water molecules in the layer. Figure 4.4(a) shows plots of $C_T(t)$ for water layers L_S, L_M and L_G. For L_S, $C_T(t)$ shows slow decay with stretched exponential dependence of the form $C_T(t) \sim A_0 \exp([-t/\tau_0]^\beta)$, where τ_0 is an effective time constant and $\beta = 0.27$. The mean residence time given by $\tau_S^T = \int_0^\infty dt \exp([-t/\tau_0]^\beta)$, is of the order of 10 ns. Similar behavior has been observed for interfacial water layers in TiO_2 nanopores [49, 50, 51]. $C_T(t)$ for L_M and L_G shows exponential decay $C(t) \sim A \exp(-t/\tau)$ (cf. inset Figure 4.4(a)). The

average residence times for L_M and L_G are $\tau_M^T \approx 10$ps and $\tau_G^T \approx 7$ ps, respectively, three orders of magnitude faster than L_S.

Figure 4.4(b) shows the reorientation time correlation $C_R(t)$ of the water dipole moment vector. The decay time of $C_R(t)$ gives the reorientation time of the water molecules for a given layer. It is observed that $C_R(t)$ exhibits an initial fast sub-picosecond decay, followed by much slower decay with a decay time of order of several picoseconds [52, 53] for all layers. This fast decay time corresponds to librations of the water dipole moment vector about a fixed direction. Beyond the libration time, the behavior of $C_R(t)$ in all the water layers is best fitted to a stretched exponential dependence of the form $C_R(t) \sim A_0 \exp([-t/\tau_0]^\beta)$, with $\beta = 0.14, 0.61, 0.59$ for L_S, L_M and L_G respectively. The observed long time orientation relaxation times are $\tau_S^R \approx 45$ ps for L_S, $\tau_M^R \approx 7.3$ ps for L_M and $\tau_G^R \approx 6.1$ ps for L_G. Such non-exponential decay has been ascribed to the presence of a broad distribution of orientation times [54, 55]. Thus the translational and rotational relaxation times of L_G and L_M are quite comparable and both are significantly smaller than those of L_S. This difference in time scales suggests that water molecules in L_M layer cannot penetrate the L_S layer. The water pinned to STO surface screens its hydrophilic effects from the rest of the water layers.

As the slit is made smaller it is observed that the residence time of water molecules in L_G decreases sharply (Figure 4.4(c) closed symbols). An opposite behavior is observed for water in a symmetric graphene-graphene confinement, where the residence time close to the graphene layer is seen to increase with decreasing confinement (Figure 4.4(c) open symbols). The reduction in water residence time in L_G as the slit width reduces, is indicative of the increased tendency of water to de-wet the hydrophobic surface due to interaction with the hydrophilic one in proximity. This dynamically signals enhanced hydrophobicity of the graphene surface in the vicinity of the hydrophilic STO surface, in agreement to the structural data. The reorientation time of water molecules in L_G is

less affected as the width varies, shown in Figure 4.4(d).

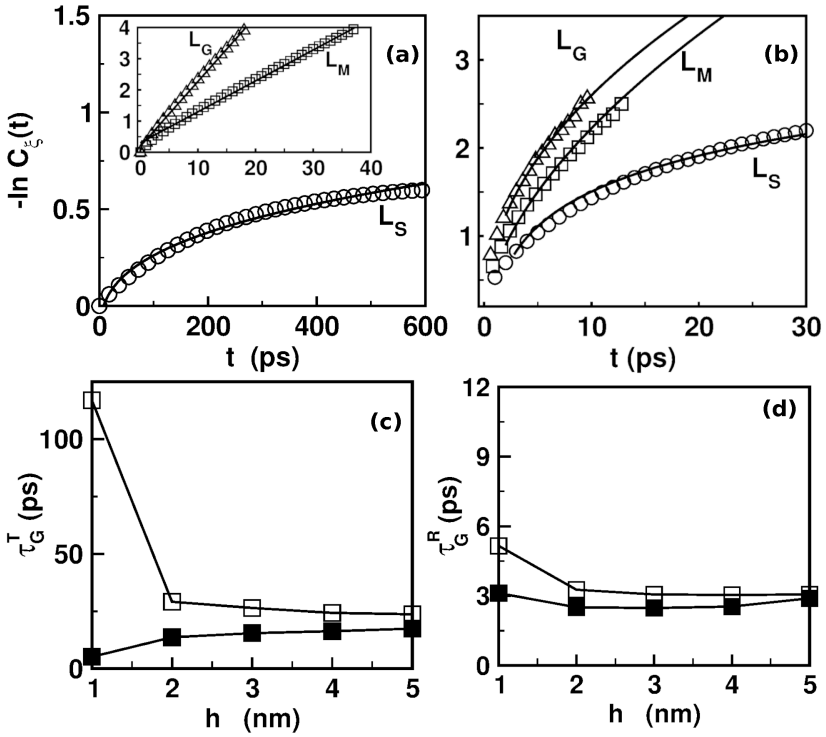

Figure 4.4: (a) Residence probability $C_T(t)$ versus t for L_S (main panel), L_M and L_G (inset). (b) Orientation time correlation function $C_R(t)$ versus t for L_S, L_M and L_G. The symbols represent data points, while the solid lines represent a fit to a stretched exponential (for L_S) and a double exponential behavior (L_M and L_G). Variations of residence time (c) and reorientation times (d) of water molecules in L_G with changing slit width, for asymmetric STO-graphene slits (filled symbols) and symmetric graphene-graphene slits (open symbols). The solid lines are a guide to the eye.

The relaxation dynamics may also be visualized via the self part of the translational and rotational van Hove density auto-correlation function (self-vHf) [46]. The self-vHf (see Equation (4.5)) gives the probability of finding a particle at a distance $|\xi|$ after a time Δt, given that the particle is at the origin at time $t = 0$. We report G_ξ at two representative times $\Delta t = \tau_l^\xi/2$ (intermediate) and $\Delta t = \tau_l^\xi$ (long time), where τ_l^ξ is the residence time or the rotational relaxation time for the lth water layer. G_ξ is expected to be Gaussian for a normal liquid. The data for G_ξ ($\xi = R, T$) for different layers exhibit deviations from this normal behavior as shown in Figure 4.5(a-b) for L_S, 4.5(c-d) for L_M and 4.5(e-f) for L_G. In the translation space for L_S, G_T shows a double Gaussian behavior, with a

secondary peak at $r/\sigma \approx 1$ (Figure 4.5(a)), where σ is the Lennard-Jones radius of the oxygen atom of the TIP4P water model. This indicates the existence of strongly pinned water molecules within the layer, which mainly vibrate about fixed positions and perform nearest neighbor jumps over long times. Similar conclusions have been reached for dynamics of glass forming liquids [56]. The rotational self-vHf for L_S shows an initial Gaussian decay followed by a tail part which is best fitted to exponential (Figure 4.5(b)). For L_M, both G_T and G_R exhibit an initial Gaussian decay, followed by an exponential tail, as shown in Figure 4.5(c) and 4.5(d) respectively. A similar behavior of G_T and G_R is observed for L_G, as seen in Figure 4.5(e) and 4.5(f).

To quantify the behavior of $G_s(r, z_a, z_b, \Delta t)$, for a given observation time Δt, we fit $\ln G_s(r, z_a, z_b, \Delta t) \sim -r^2$ for $r < r_c$ and $\ln G_s(r, z_a, z_b, \Delta t) \sim -r + C_0$ for $r > r_c$. The value of r_c represents the displacement beyond which the self-vHf shows an exponential tail for a given Δt. r_c is expected to increase as Δt increases, with the system approaching the diffusive regime. As shown in Figure 4.5(g) r_c saturates as Δt increases for both L_M and L_G. Similarly we fit $\ln G_R(\phi, z_a, z_b, \Delta t) \sim -\phi^2$ for $\phi < \phi_c$ and $\ln G_R(\phi, z_a, z_b, \Delta t) \sim -\phi + c_0$ for $\phi > \phi_c$. ϕ is the rotational displacement as defined by Equation (4.6) and ϕ_c represents the value beyond which the rotational self-vHf is no longer Gaussian for a given Δt. Figure 4.5(h) shows the dependence of ϕ_c on Δt for L_S, L_M, and L_G. As found for r_c, the value of ϕ_c is observed to saturate as Δt increases. These observations suggest that that the deviation from normal Gaussian behavior persists till the residence time in both L_M and L_G.

We also evaluate the in-plane translational and rotational mean squared displacement (MSD) of water molecules within each of the water layers, as given in Equation (4.7). Figure 4.6(a), the translational mean square displacements for water molecules in each of the layers shows a linear dependence on time, with the diffusion coefficient in L_S = 1.48×10^{-5} nm^2/ps, two orders of magnitude less

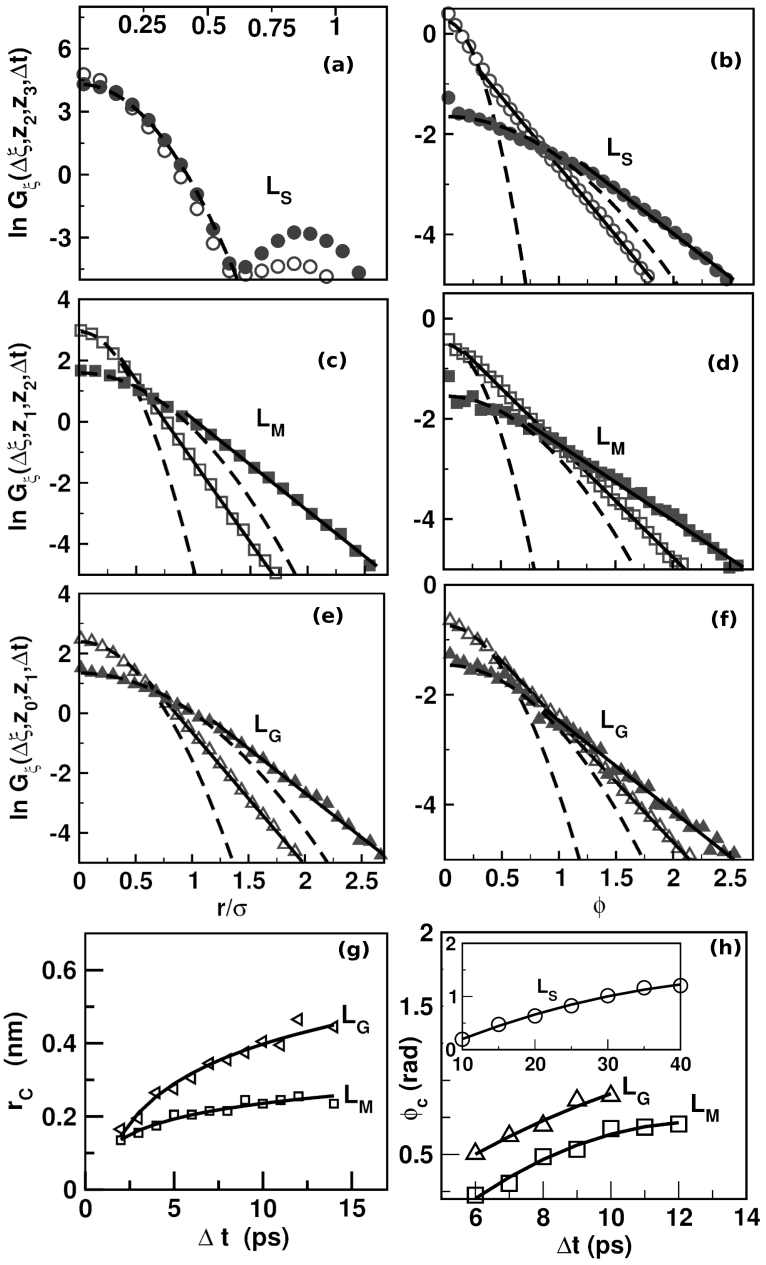

Figure 4.5: (a-f) The translational (left) and rotational (right) self-vHf G_T and G_R for L_S, L_M and L_G, evaluated at intermediate times (open symbols), and at long times (filled symbols).The dotted lines show the expected Gaussian behavior, and the solid lines show deviation from Gaussian behavior. (g-h) Variation of r_c (left) and ϕ_c (right) with Δt , for L_M and L_G . The inset of (h) shows the variation of ϕ_c with Δt for L_S .

than the diffusion coefficients for L_M and L_G (1.31×10^{-3} nm^2/ps and 2.41×10^{-3} nm^2/ps respectively). The rotational MSD is less affected by the asymmetric confinement, and depends linearly on time (Figure 4.6(b)), with the rotational

diffusion coefficient of the same order of magnitude for all the water layers (0.022 rad^2/ps, $0.027 rad^2/ps$ and $0.046 rad^2/ps$ for L_S, L_M and L_G respectively).

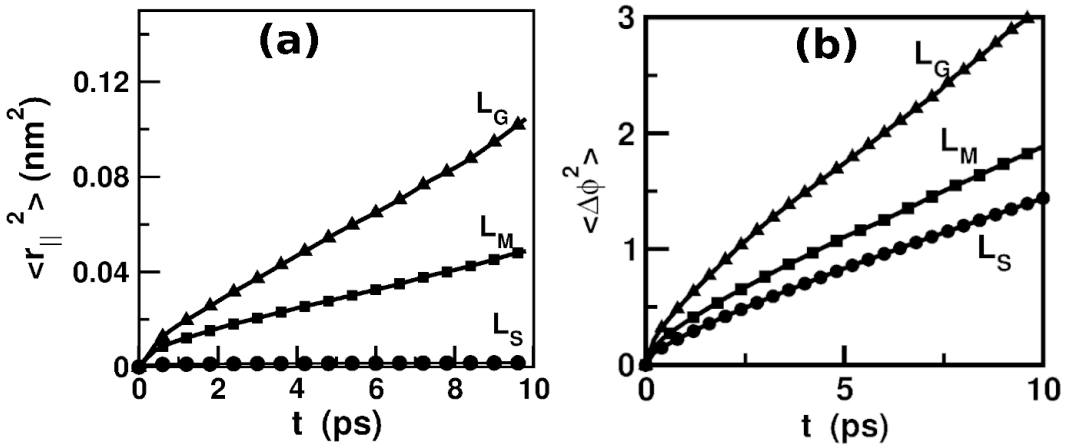

Figure 4.6: (a) The translational and (b) rotational mean squared displacement for L_S, L_M and L_G.

4.4.3 Dynamic heterogeneity

The self-vHf shows non-Gaussian behavior, contrary to that expected for Fickian diffusion. Such non-Gaussian Brownian diffusion is considered an indication of dynamic heterogeneity [57], as discussed for super-cooled liquids and colloids [58, 59], and for intercalated water droplets close to critical temperature [7]. In order to have insights the dynamic heterogeneity, we probe each layer individually. Since the slowest relaxation is observed in translational motion, we focus on the translational degrees of freedom.

First we probe the in-plane density distribution. For this, each layer is partitioned into a grid of square cells each of sides 1.5 Å, and the average density of water within each cell is evaluated for different time widows, T1 from 0 to 0.01 ns, and T2 from 5 to 5.01 ns after equilibration. T1 and T2 are taken sufficiently far apart from each other at temporal separation comparable to the slowest time scale in the system. The averaging time (10 ps) for the in-plane density is chosen to be of the order of the mean residence time of water molecules in the fast relaxing

L_M and L_G layers. A similar choice of timescales has been has been used to study water dynamic heterogeneity at the surfaces of proteins [60], oxides [61] and metal electrodes [62]. Figure 4.7 shows plots of in-plane density profiles of each layer for the two different time windows considered. For both time windows, the in-plane density profiles are observed to be qualitatively similar. In L_S water is observed to form two dimensional square ice-like crystallite regions (marked in the figure) even at room temperature, driven by strong pinning of water molecules on the STO surface. Defects in the crystalline arrangement (encircled regions in both panels of Figure 4.7(a)) are mobile and persist at long times. This partial ordering within L_S is seen to have strong effects on the subsequent water layer L_M . Water molecules in L_M tend to follow the disordered regions in L_S, (see encircled regions in both panels of Figure 4.7(b)). There is only a weak structural in-homogeneity in L_G .

Further insights to dynamic heterogeneity may be obtained from the distribution of local residence times of the water molecules. As before, we partition each water layer into a 2 dimensional grid, with each grid cell having a width of 5 Å. The grid size is larger than than that used in calculating the in-plane density profile and is so chosen as to have a number of water molecules for reasonable statistics. The local residence time correlation function for water within a grid cell υ_i in a given layer can be expressed as: $C_T^{\upsilon_i}(t) = \left\langle \frac{1}{N_l(t_0)} \sum_{i=1}^{N} \left(\prod_{t'=t_0}^{t_0+t} \Theta_i(t') \zeta(\upsilon_i, t') \right) \right\rangle_{t_0}$, where $\zeta(\upsilon_i, t') = 1$ if the ith water molecule is located inside the grid cell, and zero otherwise, $\Theta_i(t') = 1$ if $z_a \leq z_i(t') < z_b$ and 0, otherwise. For each initial time t_0, $C_T^{\upsilon_i}(t)$ is computed till it decays to zero. For L_S this typically $\sim$ 10 ns and $\sim$ 20 ps for L_M and L_G. The quantity is averaged over 5000 initial times separated by 1 ps after equilibration. The time windows are adequate and not too small as to get unnecessary fluctuations due to poor averaging nor too large as to smooth out the data. The local residence time is defined from the time constant of an exponential fit to $C_T^{\upsilon_i}(t)$ data. The local residence times $\tau_l(x, y, z)$

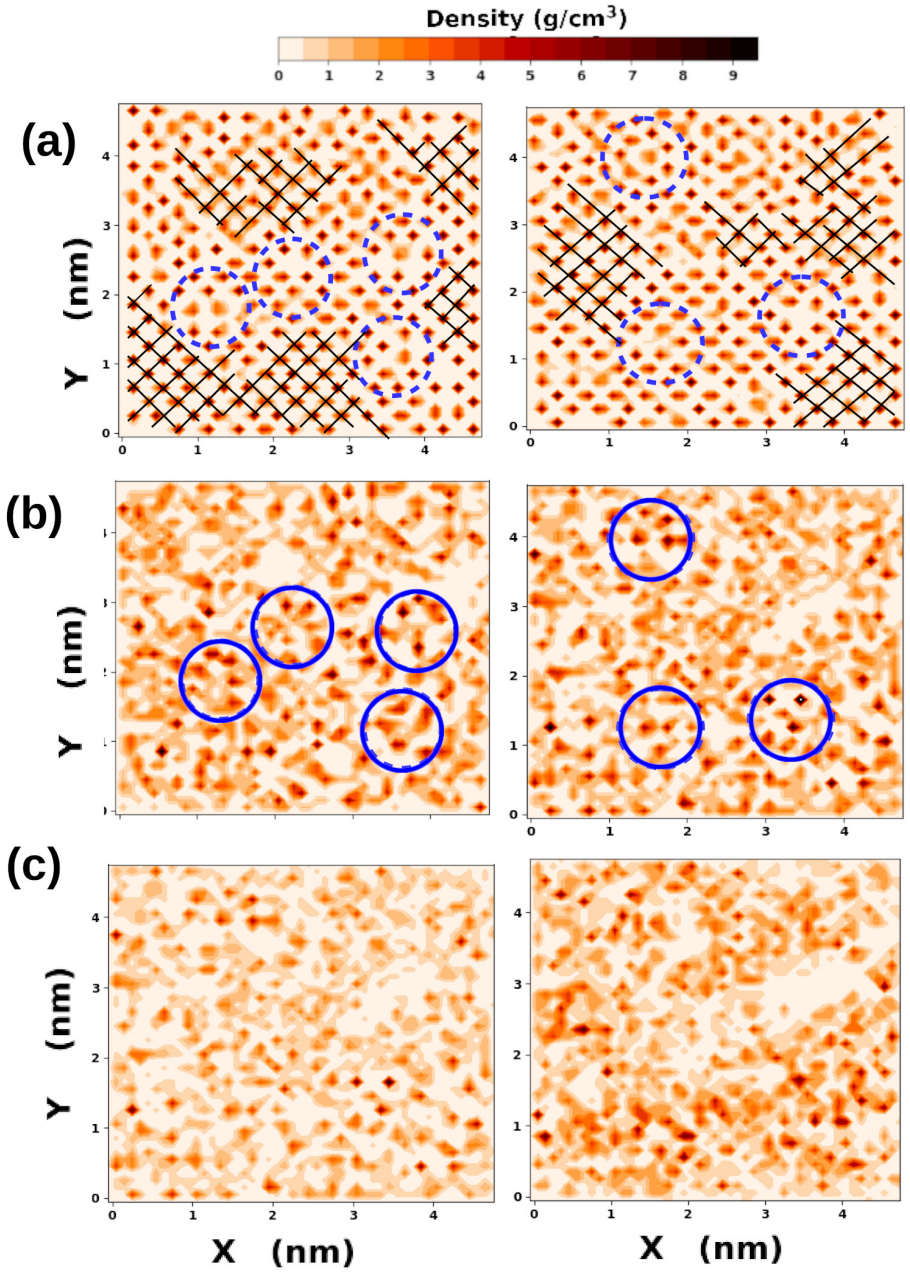

Figure 4.7: In-plane density density distribution of water molecules evaluated in time window T1 (left column) and T2 (right column), for L_S (a), L_M (b) and L_G (c). The grid shading marks square-icelike crystallites in L_S. The dotted circles show defects in L_S and the corresponding dense patches in L_M are marked by solid circles.

is related to the effective free energy as: $\tau_l(x,y,z) \propto \frac{1}{v} \exp\left(-\beta F(x,y,z)\right)$, where $\beta = 1/k_B T$ with k_B the Boltzmann constant, and $F(x,y,z)$ the effective free energy. τ_d is the time scale associated with particle translational diffusion, given

by $\tau_d = 1/\upsilon = d^2/D$, where D is the diffusion coefficient obtained from the MSD data for different layers, and d is the mean particle separation. We can thus express the free energy as: $F(x, y, z) \propto -\frac{1}{\beta} \ln\left(\frac{\tau_l}{\tau_d}\right)$. Similarly, in the rotational space the free energy may be expressed as $F(cos\theta) \propto -\frac{1}{\beta} \ln\left(\frac{\tau_P(cos\theta)}{\tau_R}\right)$, where $\tau_P(cos\theta)$ is the persistence time for a given orientation $cos\theta$, while τ_R is the mean rotational diffusion time estimated from the MSD data.

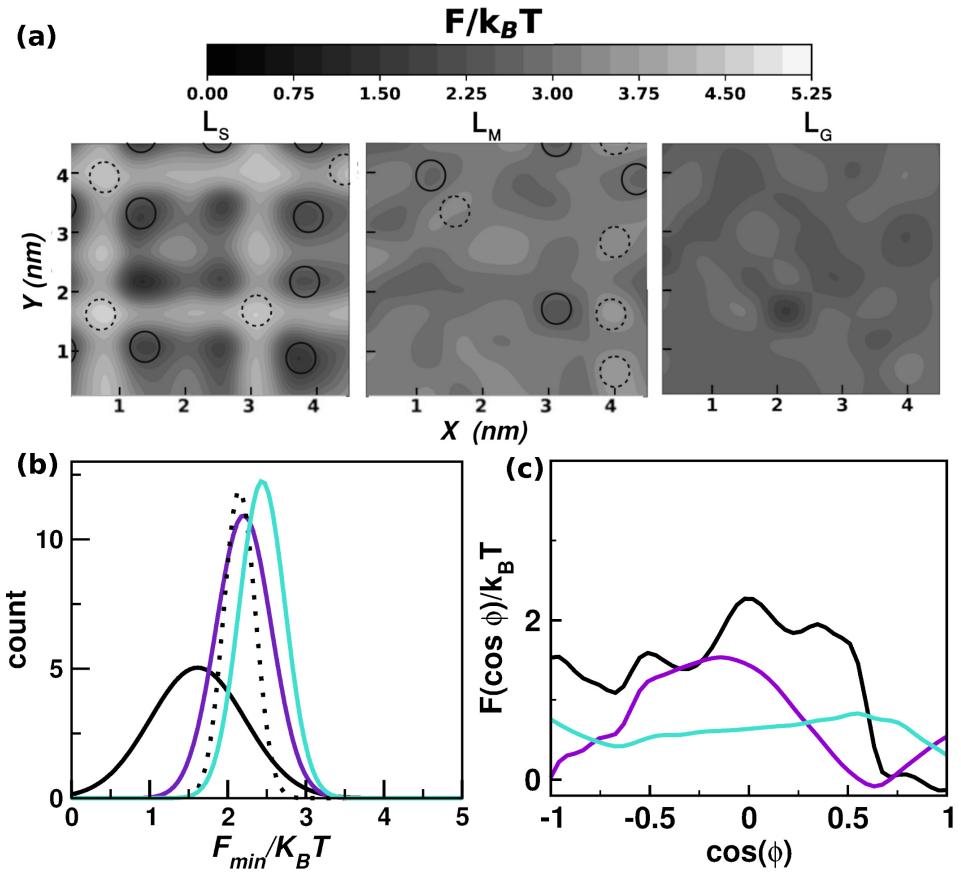

Figure 4.8: (a) Contour plot of the free energy landscapes experienced by water molecules in L_S, L_M and L_G. Dark to light shade represents deep to shallow wells, corresponding to strong and weak trapping of water molecules. The peaks (marked with solid circles) and valleys (marked with dotted circles) in the free energy landscape of L_M, are observed to resemble the valleys and peaks (respectively) of L_S. (b) Distribution of F_{min} of L_S (black), L_M (indigo/dark grey) and L_G (cyan/light grey), in comparison to that in graphene-graphene nano slit (dotted line).(c) Free energy profile in the orientation space, for water molecules in L_S (black), L_M (indigo/dark grey) and L_G (cyan/light grey).

.

Figure 4.8(a) shows the effective free energy landscapes in translational space for L_S, L_M and L_G. The free energy landscape of L_S is characterized by peaks and

deep wells, imposed by the strong pinning of water molecules at hydrophilic STO surface (leftmost panel Figure 4.8(a)). The free energy profile in L_M, has partial imprints of STO surface (middle panel Figure 4.8(a)). Many of the peaks in the free energy profile in L_M (dotted circle) correspond to the wells of the profile in L_S (solid circle), and vice-versa. The partial imprint confirms the screening of the hydrophilic surface by slow water layer in L_S over STO. The regions where the slow and pinned water molecules in L_S reside, is avoided by the water molecules in L_M. This is consistent with the lateral density distribution of water molecules in each layer, shown in Figure 4.7(c). The effective free energy landscape is more homogeneous in L_G (rightmost panel Figure 4.8(a)).

The heterogeneous dynamics is further evidenced by the distribution of local minima in the free energy landscape, F_{min}, of L_S, L_M and L_G (cf. Figure 4.8(b)). This distribution reflects the roughness of the energy landscape. The distribution is broad for L_S, in agreement with the stretched exponential decay of $C_T(t)$. The broadening may be understood from the mobile defects observed in Figure 4.6(a). The double peak in the translational self-vHf (Figure 4.5(a)) can be assigned to two different relaxations at two distinct sites. Pining leads to overall slow relaxation in the layer. In comparison, the distributions are found to be relatively sharper for L_M and L_G. The distributions in L_M is broader than in L_G. The broadening can be taken as induced by that experienced in L_S and also cause for dynamic heterogeneity. The distribution in L_G is broader compared to the case of water molecules in symmetric graphene-graphene nano-slit. Physically, within the asymmetric nano-slit, water molecules experience a very different potential as they migrate from one layer to another and this introduces dynamic heterogeneity in the system.

Figure 4.8(c) shows the free energy profiles in the orientation space for the different water layers, estimated from the persistence time data. For L_S, four minima are observed, indicating four different adsorption modes of water molecules

to the STO surface; $\theta = 0^o$: water dipole moment pointing perpendicular to the STO surface, and dipole moment vector oriented at : $\theta = 70^o$, $\theta = 110^0$ and $\theta = 150^0$, to the surface normal. The most prominent orientation, $\theta = 0^o$ defines the mode in which water molecules form two hydrogen bonds with surface oxygen atoms. The proximity to L_S, results in L_M having a preferred orientation of $\theta = 60^o$ to the surface normal. For L_G, the free energy profile is flat, with no preferred orientations of the molecules.

4.4.4 Comparison to the symmetric channels and single surfaces

Finally it is worth contrasting the dynamical behavior of water trapped within asymmetric nano confinement to the other cases, to highlight the uniqueness of the asymmetric confinement. Since the orientational relaxation times are not very sensitive, we focus on the translational residence times. Moreover, we consider the self-vHfs. We compare our data for the asymmetric confinement case with those of water within symmetric (graphene-graphene) nano confinements as well as close to single STO and single graphene surface. This comparison is summarized in Table 4.5. In bulk water as well as for water contact layer on a single graphene surface, the residence times of water molecules are comparable and the self-vHf both in translation and rotation are normal Gaussian. However, water molecules in the adsorbed layer on a single STO surface show different behavior. Here, the residence time increases by two orders of magnitude compared to bulk water, the self-vHf in translation is double Gaussian and that in rotation shows an exponential tail. In 1 nm wide symmetric confinement of two graphene surfaces, the residence time increases by an order of magnitude compared to the single graphene or bulk case, and the self-vHfs for both translation and rotation are Gaussian. In the 1 nm wide asymmetric confinement the layer adjacent to STO (L_S) is dynamically similar to the single STO case in terms of residence

time and self-vHfs. However, L_M and L_G layers have an order of magnitude smaller residence times compared to the symmetric case.The time scale for these layers are similar to the bulk water and that in the vicinity of a single graphene layer. The faster time scales are due to attraction by the hydrophilic STO layer. The self-vHfs in L_G and L_G are quite different compared to the layer adjacent to single graphene or bulk, despite having similar residence times. The self-vHfs have linear tails for L_G and L_M.

Table 4.5: Residence times and the shape of the self-vHfs (G: Gaussian, GG: Double Gaussian, GL: Gaussian with exponential tail) for water molecules in the contact layer on single graphene and STO surfaces, as well as in asymmetric and symmetric nano-slits.

Situation	Residence time	$G_T(r,t)$	$G_R(\phi,t)$
Bulk	5.4 ps	G	G
Single graphene	19.8 ps	G	G
Single STO	12.96 ns	GG	GL
Symmetric graphene	116 ps	G	G
Asymmetric L_S	13.49 ns	GG	GL
Asymmetric L_M	10.23 ps	GL	GL
Asymmetric L_G	6.71 ps	GL	GL

4.4.5 Implications for drug delivery

The faster relaxation dynamics in L_M and L_G compared to L_S in the case of asymmetric slit, may be useful for efficient transport of molecules. We investigate the behavior of a bio-molecule, namely oleic acid, within the slit, as detailed in section (4.2.5).

Figure 4.9 (a) and (b) show the equilibrium transverse density profiles of water, and the oleic acid (COO^-) head group within the STO-graphene and the STO-STO

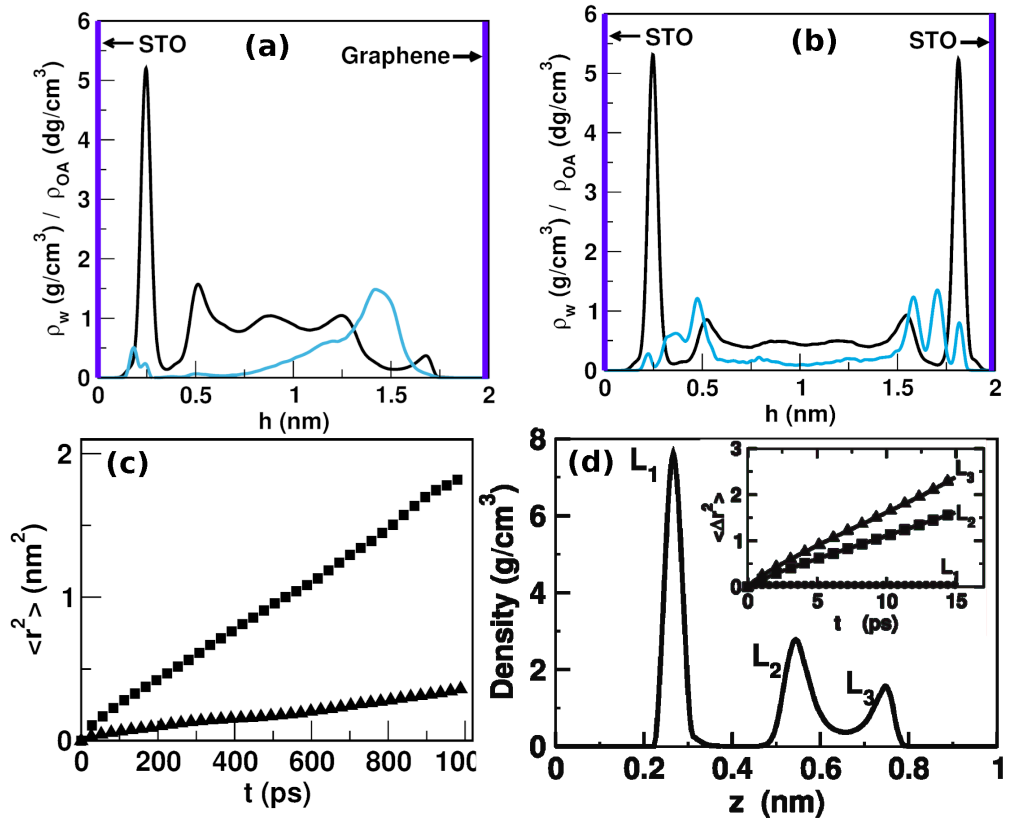

Figure 4.9: (a-b) Equilibrium density profiles of water (black/dark) and the oleic acid head group (cyan/gray), within a 2 nm wide (a) STO-graphene nano slit and (b) STO-STO nano slit. (c) Mean square displacement of oleic acid head group within the 2 nm wide STO-graphene nano (squares) and STO-STO (triangle) nano confinements. (d) Density profile of LJ liquid asymmetrically confined by strongly attracting and weakly attracting structure-less walls. The inset shows the mean squared displacement of molecules in each layer of the confined fluid

.

nano slits respectively. It is evident from these plots that the density of the head group is strongly modulated by the water density, with the oleic acid tending to reside where the water density is least. Within the STO-graphene nano-slit, this causes the oleic acid to preferentially reside closer to the the hydrophobic surface (Figure 4.9 (a)), and to avoid the hydrophilic surface on which pining may occur. For the STO-STO slit the head group of the oleic acid molecules tend to reside close to each of the confining surfaces as shown in Figure 4.9 (b). The effect of different confinement is dramatic in the the mean squared displacement as shown in Figure 4.9 (c). There is a sharp increase in mobility of oleic acid within the

STO-graphene slit, compared to the STO-STO slit. The self diffusion coefficient of the oleic acid within the STO-graphene slit is 1.05×10^{-4} nm^2/ps an order of magnitude higher than in STO-STO nano-slit.Diffusion through nano-channels has been identified as the major rate limiting step during drug release [22].

TiO_2 is known to be a bio-compatible material [63] and has been suggested for use in drug delivery. Typical drug molecules have a polar moiety which interacts with strongly hydrophilic polar TiO_2 surface. This hinders the mobility of drug molecules through TiO_2 nanopores and thereby, limiting its use for drug delivery.Although graphene is not bio-compatible, there are bio-compatible hydrophobic materials like cellulose, which lack the mechanical strength needed for long term implants [64]. It may be possible to impart mechanical support by overlaying such material over TiO_2 surface suitable for implantable drug delivery devices [65]. For this, however, one needs to check if the fluid properties remain similar in any asymmetric confinement. In Chapter 3 we have investigated the generic model of confined fluid in an asymmetric slit. For the STO-water-graphene system, the slit asymmetry is obtained by taking a ratio of the interaction energy of water with the STO slab to that with the graphene. For this asymmetry, and following the simulation procedure in Chapter 3, we obtain the density profile for fluid in a slit of height h = 3.1 σ_{ow} as shown in Fig. 4.9(d). This density profile is comparable to that obtained from the all atom STO-water-graphene simulation. The mean square displacement as a function of time for each of the liquid layers of the model fluid is shown in the inset of Figure 4.9(d). It is observed that the fluid layer adjacent to the strongly attracting wall (L_1) remains relatively immobile while mobility in L_2 and L_3 are comparable and much higher than that of L_1. Similar observations have been made for the STO-water-graphene system (cf. Figure 4.6(a)). The similarity between the two results suggests the behavior of the water under the asymmetric confinement to be general. Hence, over-layer of bio-compatible hydrophobic material on TiO_2

may provide adequate support, and high mobility of drug molecules necessary for implantable drug delivery devices.

4.5 Summary

We show that water, trapped between an oxide surface like TiO_2 surface of STO and a graphene cover at distance of 2 nm or less, gets strongly modified compared to bulk water. The coupling of ultra-slow dynamics of hydrating water layer at the STO surface with fast moving over-layers introduces translational as well as rotational dynamic heterogeneity throughout the slit. Our findings have implications in applications ranging from fabrication of heterostructures and water purification, to design of drug delivery devices.

References

[1] Q. Li, J. Song, F. Besenbacher, M. Dong, *Accounts of chemical research* **48**, 119 (2014).

[2] H. Kandori, *Biochimica et Biophysica Acta (BBA)-Bioenergetics* **1460**, 177 (2000).

[3] R. Zaleski, *et al.*, *The Journal of Physical Chemistry C* **126**, 5916 (2022).

[4] K. Koga, G. Gao, H. Tanaka, X. C. Zeng, *Nature* **412**, 802 (2001).

[5] H. Yoshida, V. Kaiser, B. Rotenberg, L. Bocquet, *Nature communications* **9**, 1496 (2018).

[6] G. Algara-Siller, *et al.*, *Nature* **519**, 443 (2015).

[7] Jiao, Shuping and Xu, Zhiping, *ACS nano* **11**, 11152 (2017).

[8] H. Mosaddeghi, S. Alavi, M. Kowsari, B. Najafi, *The Journal of chemical physics* **137**, 184703 (2012).

[9] P. Demontis, J. Gulín-González, M. Masia, G. B. Suffritti, *Journal of Physics: Condensed Matter* **22**, 284106 (2010).

[10] P. A. Bonnaud, *et al.*, *Nanotechnology (IEEE-NANO), 2016 IEEE 16th International Conference on* (IEEE, 2016), pp. 270–272.

[11] Předota, M and Bandura, AV and Cummings, PT and Kubicki, JD and Wesolowski, DJ and Chialvo, AA and Machesky, Michael L, *The Journal of Physical Chemistry B* **108**, 12049 (2004).

[12] Koparde, Vishal N and Cummings, Peter T, *The Journal of Physical Chemistry C* **111**, 6920 (2007).

[13] Kavathekar, Ritwik S and Dev, Pratibha and English, Niall J and MacElroy, JMD, *Molecular Physics* **109**, 1649 (2011).

[14] M. Srivastava, *et al.*, *Nanoscale* **7**, 4820 (2015).

[15] D. H. Nagaraju, Q. Wang, P. Beaujuge, H. N. Alshareef, *Journal of Materials Chemistry A* **2**, 17146 (2014).

[16] N. Zhang, Y. Zhang, Y.-J. Xu, *Nanoscale* **4**, 5792 (2012).

[17] J. Azadmanjiri, V. K. Srivastava, P. Kumar, J. Wang, A. Yu, *Journal of Materials Chemistry A* **6**, 13509 (2018).

[18] S. Saha, *et al.*, *Scientific reports* **4**, 6173 (2014).

[19] A. Sahoo, *et al.*, *npj 2D Materials and Applications* **2**, 9 (2018).

[20] Y. Hu, *et al.*, *Nanoscale* **7**, 19885 (2015).

[21] T. Bui, A. Phan, D. R. Cole, A. Striolo, *The Journal of Physical Chemistry C* **121**, 15675 (2017).

[22] G. Bruno, *et al.*, *Nature communications* **9**, 1682 (2018).

[23] A. Pertsin, M. Grunze, *The Journal of Physical Chemistry B* **108**, 16533 (2004).

[24] F. Leoni, G. Franzese, *Physical Review E* **94**, 062604 (2016).

[25] S. S. Pannir Sivajothi, S.-T. Lin, P. K. Maiti, *The Journal of Physical Chemistry B* **123**, 180 (2018).

[26] G. Kamath, S. A. Deshmukh, S. K. Sankaranarayanan, *Journal of Physics: Condensed Matter* **25**, 305003 (2013).

[27] H. Berendsen, J. Grigera, T. Straatsma, *Journal of Physical Chemistry* **91**, 6269 (1987).

[28] W. L. Jorgensen, J. Chandrasekhar, J. D. Madura, R. W. Impey, M. L. Klein, *The Journal of chemical physics* **79**, 926 (1983).

[29] V. Molinero, E. B. Moore, *The Journal of Physical Chemistry B* **113**, 4008 (2009).

[30] H. W. Horn, *et al.*, *The Journal of chemical physics* **120**, 9665 (2004).

[31] S. W. Rick, *The Journal of chemical physics* **120**, 6085 (2004).

[32] V. Vinš, *et al.*, *EPJ Web of Conferences* (EDP Sciences, 2016), vol. 114, p. 02136.

[33] I. Leontyev, A. Stuchebrukhov, *Physical Chemistry Chemical Physics* **13**, 2613 (2011).

[34] C. Vega, J. L. Abascal, *Physical Chemistry Chemical Physics* **13**, 19663 (2011).

[35] H. W. Horn, *et al.*, *The Journal of chemical physics* **120**, 9665 (2004).

[36] R. Elber, A. P. Ruymgaart, B. Hess, *The European Physical Journal Special Topics* **200**, 211 (2011).

[37] H. W. Horn, W. C. Swope, J. W. Pitera, *The Journal of chemical physics* **123**, 194504 (2005).

[38] S. Lukyanov, A. Bandura, R. Evarestov, *Surface Science* **611**, 10 (2013).

[39] E. Holmström, P. Spijker, A. Foster, *Proceedings of the Royal Society A: Mathematical, Physical and Engineering Sciences* **472**, 20160293 (2016).

[40] A. Buckingham, *Quarterly Reviews, Chemical Society* **13**, 183 (1959).

[41] T. Werder, J. Walther, R. Jaffe, T. Halicioglu, P. Koumoutsakos, *The Journal of Physical Chemistry B* **107**, 1345 (2003).

[42] D. Van Der Spoel, *et al.*, *Journal of computational chemistry* **26**, 1701 (2005).

[43] J. J. Janke, W. D. Bennett, D. P. Tieleman, *Langmuir* **30**, 10661 (2014).

[44] N. Schmid, *et al.*, *European biophysics journal* **40**, 843 (2011).

[45] T. Fehr, H. Löwen, *Physical Review E* **52**, 4016 (1995).

[46] J.-P. Hansen, I. R. McDonald, *Theory of simple liquids* (Elsevier, 1990).

[47] M. G. Mazza, N. Giovambattista, F. W. Starr, H. E. Stanley, *Physical review letters* **96**, 057803 (2006).

[48] D. T. Limmer, A. P. Willard, P. Madden, D. Chandler, *Proceedings of the National Academy of Sciences* **110**, 4200 (2013).

[49] E. Gonzalez Solveyra, E. de la Llave, V. Molinero, G. J. Soler-Illia, D. A. Scherlis, *The Journal of Physical Chemistry C* **117**, 3330 (2013).

[50] A. Shekhar, *et al.*, *Applied Physics Letters* **105**, 161907 (2014).

[51] J. Phillips, *Reports on Progress in Physics* **59**, 1133 (1996).

[52] D. Laage, G. Stirnemann, F. Sterpone, R. Rey, J. T. Hynes, *Annual review of physical chemistry* **62**, 395 (2011).

[53] N. Choudhury, *The Journal of chemical physics* **133**, 154515 (2010).

[54] D. Laage, W. H. Thompson, *The Journal of chemical physics* **136**, 044513 (2012).

[55] P. A. Pieniazek, Y.-S. Lin, J. Chowdhary, B. M. Ladanyi, J. Skinner, *The Journal of Physical Chemistry B* **113**, 15017 (2009).

[56] J. Helfferich, *et al.*, *The European Physical Journal E* **41**, 71 (2018).

[57] B. Wang, J. Kuo, S. C. Bae, S. Granick, *Nature materials* **11**, 481 (2012).

[58] Chaudhuri, Pinaki and Berthier, Ludovic and Kob, Walter, *Physical review letters* **99**, 060604 (2007).

[59] S. Dutta, J. Chakrabarti, *Soft matter* **14**, 4477 (2018).

[60] M. Heyden, *The Journal of chemical physics* **150**, 094701 (2019).

[61] D. Argyris, T. Ho, D. R. Cole, A. Striolo, *The Journal of Physical Chemistry C* **115**, 2038 (2011).

[62] A. P. Willard, D. T. Limmer, P. A. Madden, D. Chandler, *The Journal of chemical physics* **138**, 184702 (2013).

[63] F. López-Huerta, *et al.*, *Materials* **7**, 4105 (2014).

[64] Kolakovic, Ruzica and Peltonen, Leena and Laukkanen, Antti and Hirvonen, Jouni and Laaksonen, Timo, *European Journal of Pharmaceutics and Biopharmaceutics* **82**, 308 (2012).

[65] S. Park, U. Han, D. Choi, J. Hong, *Biomaterials research* **22**, 29 (2018).

Chapter 5 Surface specific ligand adsorption by $CsPbBr_3$ nano-particles

5.1 Introduction

Colloidal nanoparticles possess size dependent optoelectronic, chemical and mechanical properties that differ from those found in bulk solids. With tuneable size, morphology and composition, they hold promise for several novel applications in the fields of electronics [1], photonics [2], therapeutics [3], catalysis and sensing [4, 5] etc. Their ability to self-aggregate has also made them appealing building blocks for bottom-up fabrication of complex and robust nano-materials [6, 7, 8].

In particular, colloidal cesium-lead-halide peroveskite nanoparticles with general formula $CsPbX_3$, where X = (Br, Cl, I), have attracted significant attention, owing to their simple and highly controllable synthesis process, unique photoluminescent and photovoltaic properties, and ability to self-aggregate into nanostructures with different morphologies [9]. The most widely studied among these is $CsPbBr_3$ [10], which has been observed to form self-assembled superlattices with high defect tolerance, enhanced fluorescence and tuneable photo-luminescent quantum yield. Various self-assembled nano-structures of $CsPbBr_3$ with tuneable composition and morphology, such as one-dimensional

nanowires, and two dimensional nanoplates, have been successfully fabricated [11, 12, 13, 14].

Bulk $CsPbBr_3$ has an orthorhombic crystal structure at ambient conditions and transitions to cubic polymorphs at higher temperatures [15]. Each Pb atom of the crystal is at the center of an octahedral cage formed by 6 Br atoms, with the octahedra sharing coners infinitely in all 3 spatial directions, as shown in Figure 5.1(a). The cavities left by the octahedra are occupied by the Cs atoms. This gives the Cs atoms a 12-fold Br coordination, while the Pb atoms have a 6-fold Br coordination. Along the [001] direction, there are alternating CsBr and $PbBr_2$ planes as shown in Figure 5.1(b).

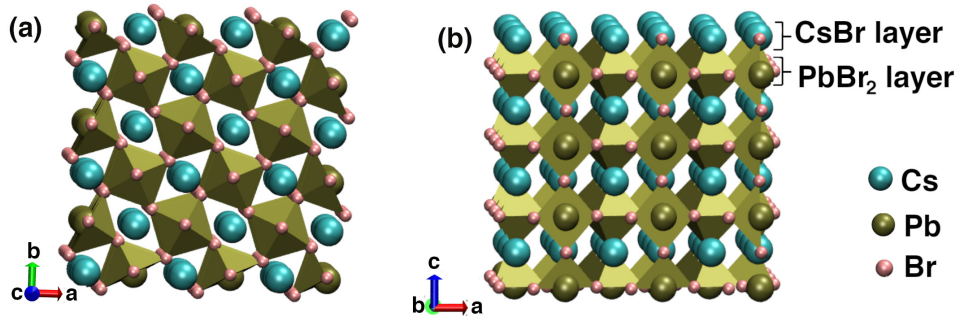

Figure 5.1: Optimized $CsPbBr_3$ crystal structure. (a) shows a top view with Pb atoms caged in edge sharing octahedra formed by Br atoms. Cs atoms fill interstitials between the octahedra. (b) shows a side view, with alternating CsBr and $PbBr_2$ planes along the [001] direction.

The crystal symmetry of $CsPbBr_3$ nanoparticles is identical to that of the bulk [16]. However, the surface termination of the nanoparticles remains unclear [17]. Their crystal structure allows for different surface terminations, including termination at the CsBr layer or $PbBr_2$ layer along the [001] directions, and termination in mixed Cs-Pb-Br along the [010] directions. Theoretical calculations and NMR experiments [18, 17], have reported that the nanoparticles have structure $[CsPbBr_3](PbBr_2)\{Cs^+Br^-\}$, with $CsPbBr_3$ core, $PbBr_2$ inner shell and an outer shell composed of Br^- anions and monovalent Cs^+ cations. Density functional

theory calculations have shown that for both CsBr and $PbBr_2$ terminations, the total electronic density of states retains features similar to those of the bulk. This is an indication that both kinds of termination do not induce any deep trap states at the surface [19]. Transmission electron microscopy studies [9] of as-synthesized $CsPbBr_3$ nano-particles reveal that the nanoparticles have Cs:Pb:Br elemental composition in a ratio of about 1.1:1:2.8, close to the stoichiometric values for bulk $CsPbBr_3$. This suggests that the nanoparticles surface termination involves both CsBr and $PbBr_2$ layers, as this yields nanoparticles with composition ratio similar to that observed from experiments.

Defects at the surface, such as vacancy sites, play an important role in surface chemistry and optoelectronic properties of $CsPbBr_3$ nanoparticles [20, 21]. Vacancies can act as trap sites for electrons [22], altering charge transport and reducing the photo-luminescent quantum yield. Vacancies can also induce directed self-assembly of nanoparticle [23]. It has been observed that $CsPbBr_3$ show a high defect tolerance, with the defect sites being passivated by surface ligands [24].

Traditionally, a mixture of organic ligands, namely oleic acid and oleylamine, are employed in the synthesis of colloidal $CsPbBr_3$ nanoparticle. These ligands passivate the surface and control the growth, stability, aggregation, and interactions of the nanoparticles. NMR spectroscopy experiments [25, 26], suggest that both ligand types bind to the nanoparticle surface in the form of charged and neutral species. These include oleylamine binding as oleylammonium bromide, and oleic acid as cesium-oleate [9]. The binding has been shown to be highly dynamic [9], with the solvent playing a crucial role in dynamic equilibrium of adsorbed and desorbed species [9]. Solvents with higher polarity have been observed to favor desorption of ligands, leading to instability of nanocrystals [27, 28] and vice versa. It has been shown that different ligand combinations as well as solvent choices can result in the formation of different self-assembled nanoparticle super-lattices. However, successful manipulation of interfacial

processes through surface ligands to yield desired superlatices with specific functionality, has remained a challenging task. This requires detailed knowledge of different competing interactions at the nanoparticle interface, including defects, surface-ligand, ligand-ligand, and ligand-solvent interactions.

In this study, we use all-atom molecular dynamics simulations, assisted by inputs from DFT calculations, to investigate ligand adsorption on colloidal lead-halide perovskite nanoparticles in the presence of different solvents, using $CsPbBr_3$ nanoparticles as a representative case. Two models of ligand dressed nano-particles suspended in solvent is considered; one having Br vacancies, and another with no Br vacancies at its surface. We carry out molecular dynamics simulations to understand ligand adsorption and ligand shell structure at different surface terminations of the nanoparticle. We evaluate, using the metadynamics technique, the free energy profile for interaction between different facets of two nanoparticles in the presence of different solvents, and probe how the free energy profile is affected by the facet termination, ligand shell structure, and type of solvent.

We find that ligand adsorption at different facets is driven by electrostatic interactions. More ligands are adsorbed on nanoparticles having Br vacancies at their surface, compared to nanoparticles without Br vacancies. Calculation of the ligand coverage at each facet in the presence of different solvents reveals that the Pb-terminated surface is more favorable for ligand adsorption compared to the Cs-terminated surface. The ligand coverage as well as ligand shell ordering at each facet decay with increasing solvent polarity, following a power law with exponent ~ 0.8. The free energy profile of interaction between two nanoparticles is found to be closely dependent on ligand adsorption at the interacting facets. We find that the preferential ligand binding to the Pb-terminated facets results in strong attractive interactions with other Pb-terminated facets, evidence of directed interactions. The strong attraction is driven by ligand interdigitation.

As solvent polarity increases, more ligands get desorbed from the nanoparticle surface, and the interactions are observed to become repulsive.

5.2 Computational details

5.2.1 $CsPbBr_3$ nanoparticle model

A model of the $CsPbBr_3$ nanoparticle should mimic the experimental situation in the sense that the nanoparticle surface termination, size, and atom ratio should be similar to experimentally observed one. The effects of surface defects/vacancies should be considered, and the nanoparticle surface should be passivated by organic ligands. We attempt to satisfy these requirements when creating the nonoparticle model for our studies.

To obtain a starting structure for the nanoparticle, we carry out optimization of bulk $CsPbBr_3$within the framework of density functional theory as introduced in chapter 2. Using the initial crystal structure as reported in reference [29], the bulk relaxation calculations are carried out using the plane wave pseudo potential method implemented within the Vienna Ab Initio software Package (VASP) [30, 31]. Projector Augmented Wave pseudo-potentials [32, 33] with the generalized gradient approximation as parameterized by Perdew, Burke and Ernzheroff [34] are considered for the exchange correlations. The geometry is considered to be relaxed when the maximum force on the atoms converges to a value less than 0.01 eV/Å. The lattice parameters of the relaxed bulk structure are **a** = 8.21 Å, **b** = 8.28 Å, and **c** = 11.28 Å, in agreement with reported values [29].

We construct two nanoparticle models from the relaxed bulk crystal lattice as follows: (i) A charge neutral, stoichiometric $CsPbBr_3$ nanocube of sides $\sim$ 2.12 nm, is cut from the bulk lattice. The cube is terminated at the CsBr layer along [001] and $PbBr_2$ layer along the $[00\bar{1}]$ direction, while other facets taken along the

[100] direction, have mixed termination with all 3 atom types. The nanoparticle has a total of 72 Cs, 72 Pb, and 216 Br atoms. (ii) A nanoparticle similar to (i), but having Br vacancies (denoted V_{Br}) randomly distributed at its surface. Schematic representations of the nanoparticle models with and without Br vacancies at the surface are shown in Figures 5.2 (a) and (b), respectively. The choice and density of the vacancies is elaborated in the subsequent section. These models allow us to simultaneously investigate surface - ligand interactions for different possible nanoparticle surface terminations under the same solvent environment.

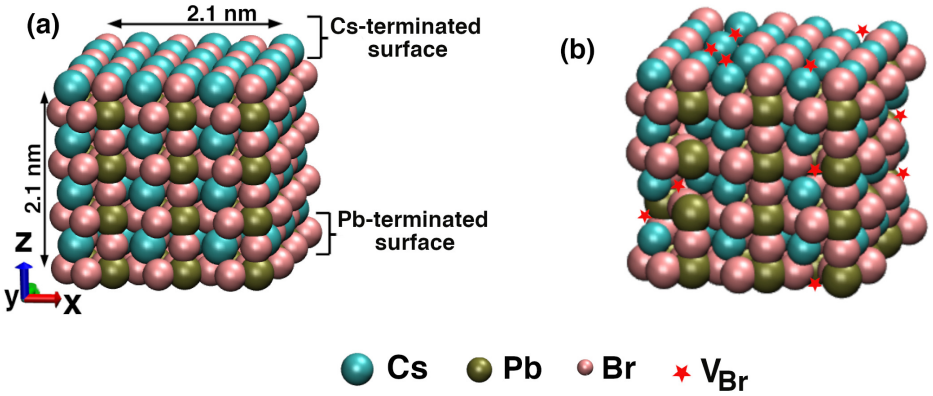

Figure 5.2: (a) $CsPbBr_3$ nanoparticle model with no Br vacancies. The nanocube has size 2.12 nm with 72 Cs atoms, 72 Pb atoms and 216 Br atoms. The nanoparticle is terminated at the Pb-layer and Cs-layer along the z-diction. (b) Nanoparticle model with V_{Br} sites at the surface. The vacancies have a density of $1/nm^2$.

5.2.2 Quantum mechanical calculation of vacancy formation energies

To probe the dominant defects at the surface of $CsPbBr_3$ nanoparticles, we perform density functional theory based calculations to determine cation and anion vacancy formation energies on different facets of $CsPbBr_3$ in slab like geometry. The vacancy formation energy is defined as [35]

$$\Delta E^f(\alpha, q) = E(\alpha, q) - E(\text{cell}) + \mu_\alpha + q(E_F + E_{VBM}), \tag{5.1}$$

where $\Delta E^f(\alpha, q)$ is the formation energy of a vacancy α of charge q, $E(\alpha, q)$ is the total energy of the supercell containing the vacancy α with the charge q compensated by adding an opposite homogeneous background charge density, $E(\text{cell})$ is the total energy of the pristine supercell, μ_α is the chemical potential of the vacancy atom in its pure elemental form, while E_F and E_{VBM} are the Fermi energy, and the energy of the valence band maximum respectively for the pristine system. This last term is added to account for the energy cost of exchanging electrons with an "electron reservoir", while the chemical potential term accounts for the energy cost of exchanging atoms with a reservoir.

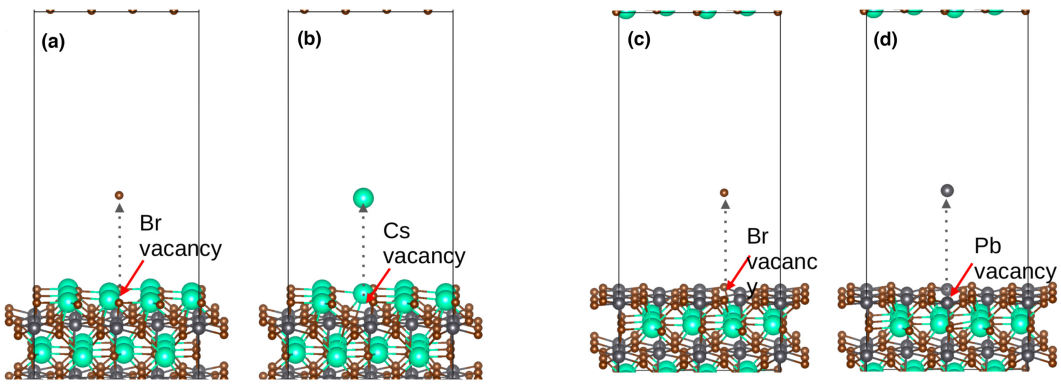

Figure 5.3: Formation of (a) Br vacancy at CsBr terminated surface (b) Cs vacancy at CsBr terminated surface (c) Br vacancy at $PbBr_2$ terminated surface (d) Pb vacancy at $PbBr_2$ terminated surface considered

.

Our calculations are performed using the plane-wave-basis projector augmented wave method as implemented in the Vienna ab-initio simulation package code (VASP) [30, 31]. For the exchange correlations, the generalized gradient approximation with Perdew-Burke-Ernzerhof exchange-correlation functional is applied. The wave functions are expanded by plane waves with a kinetic energy cutoff of 500 eV and all atoms in the supercell are allowed to relax using a conjugate gradient scheme until their residual forces converged to less than 0.2 eV/nm. A large supercell containing a 9-layer $CsPbBr_3$ slab, terminating in a CsBr or $PbBr_2$ layer along the [001] direction is used, with a vacuum space

of 15 Å incorporated at each surface to avoid interaction between adjacent slab surfaces. Figures 5.3 (a) and (b) show the top half of supercell used for calculating the formation energies of Br and Cs vacancies respectively at a CsBr-terminated slab surface, while Figures 5.3 (c) and (d) show the top half of supercell used for that of Br and Pb vacancies respectively at the $PbBr_2$ terminated surface.

Facet termination	**Vacancy Formation Energy**		
	Cs^+	Br^-	Pb^{2+}
CsBr terminated facet	3.26 eV	3.21 eV	
$PbBr_2$ terminated facet		3.05 eV	6.52 eV

Table 5.1: Formation energies for Cs^+, Br^-, and Pb^{2+} vacancies on different facets of $CsPbBr_3$

The calculated vacancy formation energies are shown in Table 5.1. It is observed that Br vacancies have lower formation energies compared to cation vacancies at both the CsBr and $PbBr_2$ terminated facets, indicating that Br vacancies are most likely to be formed at both surfaces. This result agrees with previous experimental findings which show that Br vacancies (V_{Br}) are the predominant defects at Cs-Pb-Br perovskite surfaces [14]. The formation energy of Cs vacancies, though slightly higher, is comparable to the V_{Br} formation energy. However, we do not consider Cs vacancies in our study. In order to incorporate effects of vacancies in our investigations, we have considered a nanoparticle model with 0.11% of the Br^- ions per nanoparticle randomly removed form surface sites as shown in Figure 5.2(b). to maintain charge neutrality, these Br^- are placed within the solvent. This creates a surface vacancy density of 1 /nm^2.

5.2.3 Surface ligands

For passivating the nanoparticle surface, we consider two combinations of oleic acid and oleylamine ligands interacting with the nanoparticle facets namely (i) a 1:1 combination of charged oleic acid denoted OLA^- and neutral oleylamine

denoted OAM and (ii) a 1:1 combination of neutral oleic acid denoted OLA and charged oleylamine denoted OAM^+. Figures 5.4(a) and (b) show representations of the molecular structures of the ligands considered. For each of the ligands, an optimized molecular geometry is obtained from the PubChem database [36]. Using the configuration builder tool PACKMOL [37], a total of 16 ligands, 8 of each ligand type are placed at each facet of the nanoparticle, with the centre of mass of the ligand head group at a distance of 5 Å away from the nanoparticle surface. This yields a ligand surface density of ~ 4 /nm^2. Similar surface ligand densities have been observed experimentally.

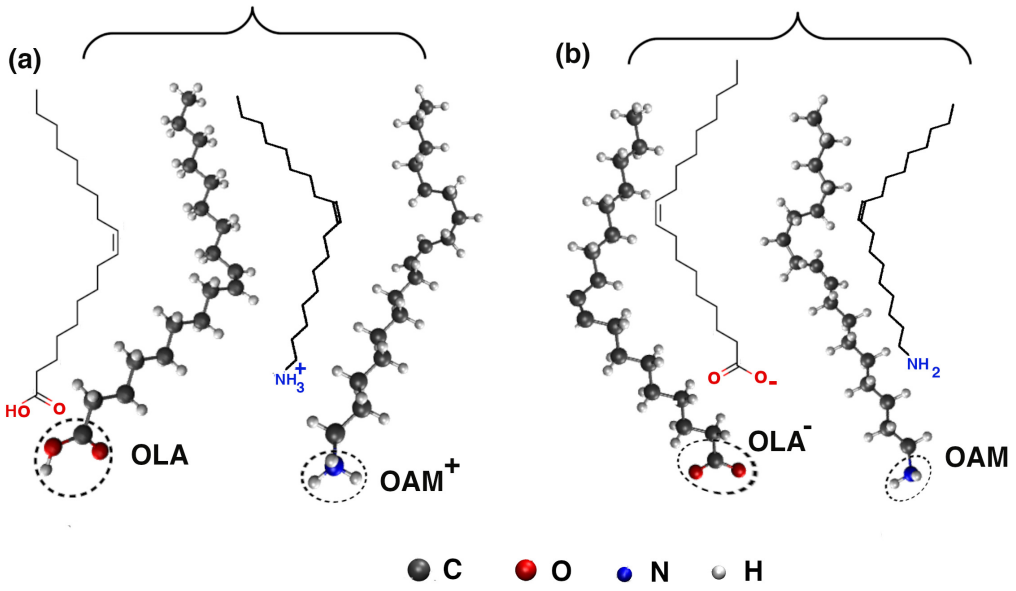

Figure 5.4: Optimized molecular geometry for (a) OLA and OAM^+ ligands (b) OLA^- and OAM ligands. The encircled regions indicate the ligand headgroups.

5.2.4 Solvents

We consider five different solvents with varying degree of polarity [38], as shown in Table 5.2. For each solvent, the optimized molecular geometry is obtained from the PubChem database [36], and replicated to generate a large solvent box of dimensions 5 nm $\times$ 5 nm $\times$ 5 nm. The solvent box is equilibrated by running a

10 ns MD simulation in NPT ensemble. The equilibrated solvent is eventually used for solvation of the nanoparticle - ligand system.

Solvent	Dielectric Constant
Hexane	1.88
Toluene	2.38
Chloroform	4.72
Ethanol	24.55
Water	80.00

Table 5.2: Solvents considered and their dielectric permittivity.

5.2.5 MD Simulation details

Having constructed a model which mimics experimentally observed nanoparticles, we then proceed to investigate ligand adsorption at the nanoparticle surface, using molecular dynamics simulations. We consider a nanoparticle with and without V_{Br}, in a cubic simulation box of sides 15 nm, for different ligand combinations and solvents outlined above. We perform all atom Molecular dynamics simulations at constant pressure, constant particle number and temperature of 300K (NPT ensemble). The temperature and pressure are kept fixed using the Nose-Hoover thermostat and Parrinello-Rahman Barostat respectively, details of which have been presented in chapter 2. Interactions between atoms are modeled using the optimized potentials for liquid simulations (OPLS-aa) all atom forcefield. This forcefield models van der Waal interactions between atoms via the Lennard-Jones potential, electrostatic interactions by the Coulomb potential, while bond stretching, bond bending as well as dihedral interactions are considered to be harmonic as described in Chapter 2. We consider a cutoff length of 1.2 nm for van der Waal interactions, while long range coulombic interactions are treated using the Ewald summation approach. Periodic boundary conditions are applied in all three spatial directions. All simulations are performed using

the Desmond Molecular dynamics module of the Schrodinger software suit, with a time step of 2 fs, and a total production run length of 50 ns with particle positions and velocities recorded every 1 ps. The final 40 ns of each trajectory are used for performing the analysis.

5.2.6 Metadynamics simulation

To obtain the interaction free energy profile between two interacting nanoparticle, we employ the approach of well-tempered metadynamics. As introduced in chapter 2 well-tempered metadynamics allows efficient sampling of the free energy profile for a given collective variable, by periodically depositing Gaussian potentials along the trajectory in collective variable space during a normal MD simulation. These Gaussians help the system to rapidly escape local minima in the free energy. To improve convergence of the scheme, the height of the Gaussians is progressively reduced by a biasing factor in the course of the simulation as has been elaborated in chapter 2.

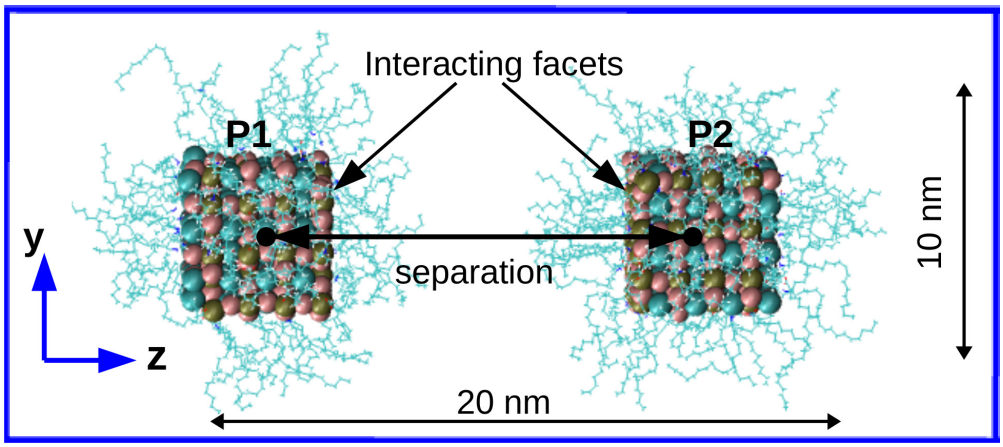

Figure 5.5: Setup for well-tempered metadynamics showing the two ligand covered nanoparticles. For clarity solvent is not shown. The two nanoparticles are constrained to move only along the z direction, and their separation is used as the collective variable.

We choose the distance between the centers of mass of the two nanoparticles as collective variable. To set up our metadynamics calculation, two ligand dressed

nanoparticles $P1$ and $P2$, each of which is modeled in a similar manner as in the MD simulations, are placed adjacent to each other along the z direction such that their centers of mass are separated by an initial distance of 10 nm, and the relevant facets are facing each other as illustrated in Figure 5.5. The simulation box of dimensions 10 nm$\times$10 nm$\times$20 nm is then solvated with the relevant solvent. The system is the equilibrated by running a 5 ns MD simulation in the NVT ensemble, with the two nanoparticles frozen in place. For the production runs, $P1$ is restrained in fixed position, while $P2$ is restrained such that it can only move along the z direction. The ligand and solvent molecules are free to move in all 3 spatial directions. Also the maximum allowed separation between the nanoparticles is set to 10 nm, to improve sampling of the collective variable space. The width of the Gaussian potentials is set to 0.1 nm, and the simulation time step 2 fs. Gaussians are deposited after every 100 steps with a bias factor of 50 and a starting Gaussian height of 0.3 kcal/mol. This corresponds to an initial energy deposition rate of 1.5 cal mol^{-1}fs^{-1}. Each production run is of length 100 ns. The chosen facets face each other throughout the simulation, and the free energy profile for their interaction is obtained from the sum of deposited Gaussians.

5.3 Results

5.3.1 Nanoparticle structure and ligand coverage from MD simulations.

(a) **Nanoparticle effective size:-** We begin by probing the effective size and structure of the ligand grafted nanoparticles. An estimate of the nanoparticle effective diameter can be obtained as $\sigma_o = \sigma_{\text{core}} + 4R_G$, where σ_{core} is the diameter of the nanoparticle crystalline core, and R_G is the radius of gyration of the ligands at the nanoparticle surface given by $R_G^2 = \frac{1}{N}\left\langle \sum_{k=1}^{N} \left(\mathbf{r}_k - \mathbf{r}_{\text{cm}}\right)^2 \right\rangle$. Here $\mathbf{r}_k$ is the

position of the k*th* atom belonging to a ligand molecule with $r_{\rm cm}$ as its center of mass. $\langle \cdots \rangle$ represents the ensemble average. Fig 5.6 shows fluctuation of the radius of gyration as a function of simulation time, for the different ligand types in presence of hexane solvent. We observe that fluctuations of R_G with time are small ($\sim$ 0.02 nm), indicating that the ligands have a stable configuration. The mean R_G for all the ligand is 0.53 nm, thus mean diameter of the nanoparticle is $\sigma_o = 4.2$ nm, where the nanoparticle has a crystalline core of diameter 2.1 nm.

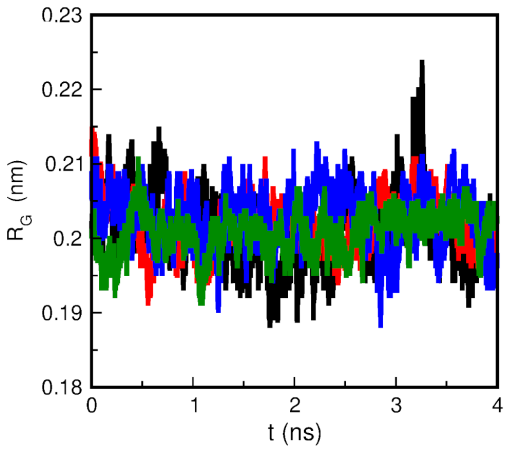

Figure 5.6: R_G as a function of simulation time, for the different ligand types : OLA (black), OAM (red) OLA^- (blue), OAM^+ (green) in presence of hexane solvent.

(b) **Solvent density profile:-** Figure 5.7(a) shows normalized number density profiles of solvent around the nanoparticle with Br vacancies, for non-polar hexane and polar water solvent. It is observed that solvent density close to the nanoparticle surface is lower in non-polar solvent than that in the polar solvent. This indicates that the polar solvent better penetrates the ligand shell and competes with the ligand for adsorption at the nanoparticle surface. The non-polar hexane solvent on the other hand does not displace the ligand. A similar distribution of solvent and ligands is observed for the case of a nanoparticle without V_{Br} sites at the surface, as shown in Figure 5.7(b).

(c) Ligand coverage:- We examine the details of ligand distribution on different facets of the nanoparticle in presence of hexane solvent. This is done by

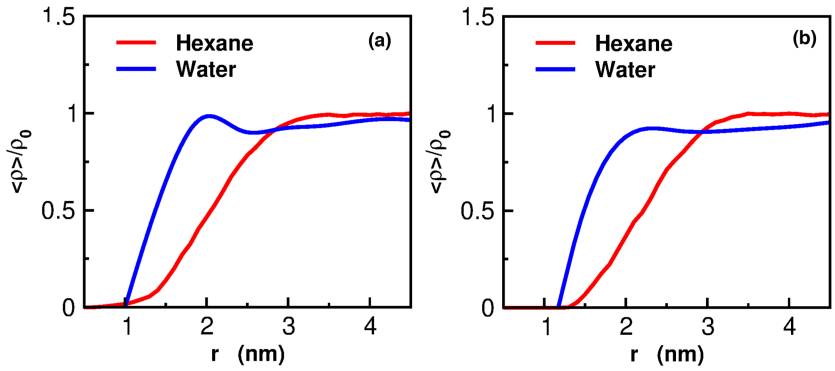

Figure 5.7: Normalized solvent density as a function of distance from the center of mass of a nanoparticle (a) with Br vacancies and (b) without Br vacancies.

calculating the pair correlation functions of the ligands with different adsorption sites. The pair correlation function for two distinct particle groups (A, B) is given by $g^{\alpha}_{A,B}(r) = \frac{1}{4\pi r^2 \langle \rho_B \rangle} \frac{1}{N_A} \sum_{i \in A}^{N_A} \sum_{j \in B}^{N_B} \delta(r - |r_{ij}|)$, where N_A and N_B are the number of particles of type A and B respectively, and $\langle \rho_B \rangle$ the particle density of type B averaged over a spherical shells of radius r and thickness Δr around particles of type A. $g^{\alpha}_{A,B}(r)$ measures the probability of finding a particle of type B at a distance r from a particle of type A. Type A represents one of the adsorption sites:- Cs^+, Pb^{2+},Br^- and V_{Br}, while B is the center of mass of the head group for OLA, OLA^-, OAM, OAM^+ ligands. The index α = (Cs, Pb) is used to denote the pair distribution function for ligands at sites on the Cs-terminated surface and Pb-terminated surface respectively. Ligand are considered to be adsorbed on a site, if the distance between the ligand headgroup center of mass and the adsorption site r < 0.35 nm. This distance is comparable to the hydrogen bond length in polymeric systems [39].

We examine the details of ligand adsorption when a combination of OLA^- and OAM ligands is used in presence of hexane solvent. Figure 5.8 shows pair correlation functions for ligands at Cs-terminated (left panel) and Pb-terminated (right panel) surfaces of the nanoparticle, with and without V_{Br} at the surface (red and blue curves respectively). As seen from Figure 5.8(a) the first peak in

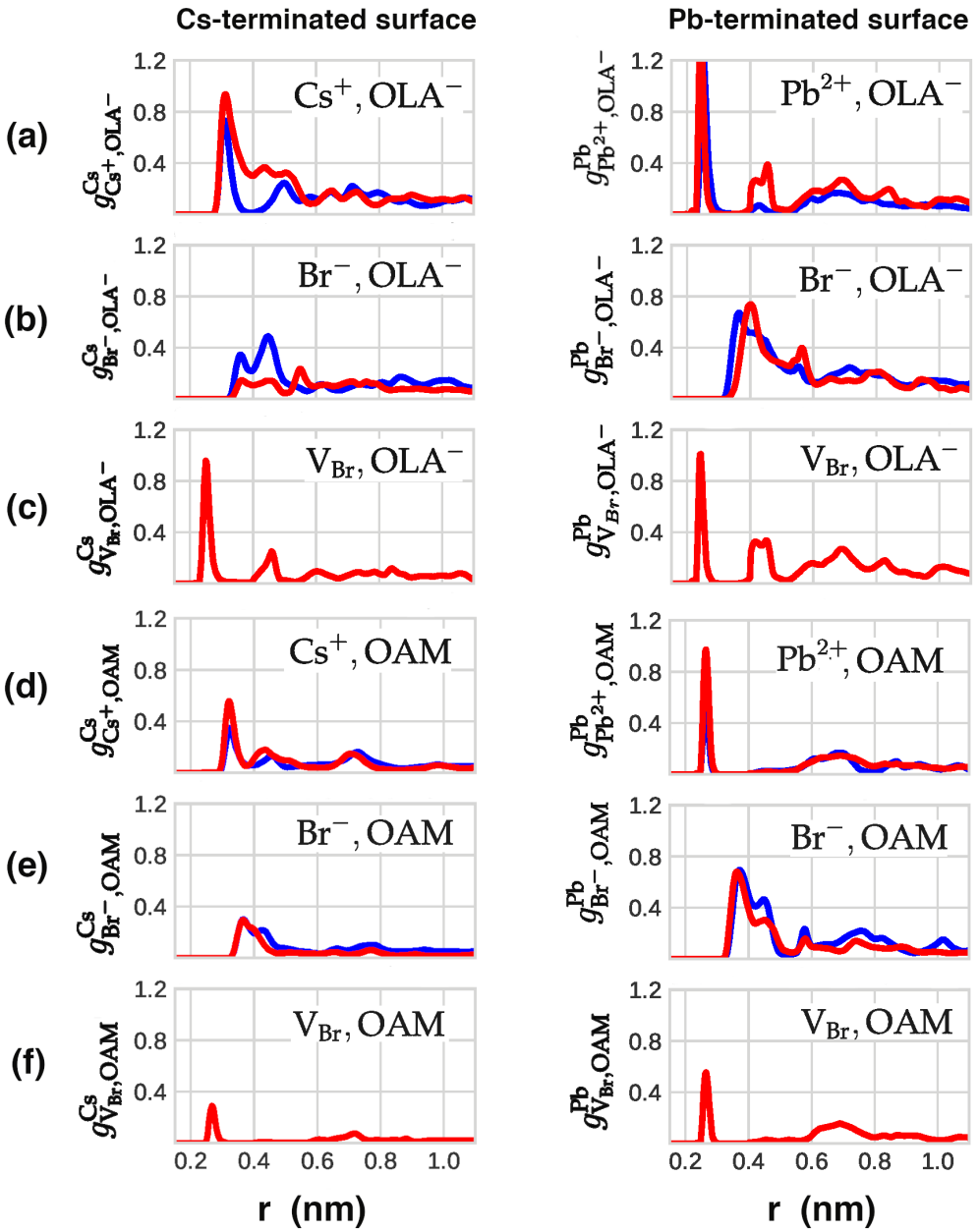

Figure 5.8: Pair correlation of OLA^- and OAM ligands around different adsorption sites at Cs-terminated surface and Pb-terminated surfaces. The red curves are for nanoparticle with Br vacancies while the blue lines are for nanoparticle with no vacancies.

the pair correlation of OLA^- at Cs^+ and Pb^{2+} sites, occurs at a distance r < 0.35 nm. This indicates that OLA^- ligands are adsorbed at Cs^+ and Pb^{2+} sites on the Cs-terminated and Pb terminated surfaces respectively. Also the red curve lies above the blue curve in both cases, indicating that more ligands are adsorbed when the nanoparticle surface has V_{Br} sites. In Figure 5.8(b), it is observed that

the first peak lies beyond 0.35 nm, indicating that OLA^- ligands are not adsorbed at Br^- sites both at the Cs-terminated and Pb-terminated surfaces. It is also observed from Figure 5.8(c) that OLA^- ligands are adsorbed at V_{Br} sites at the Cs-terminated and Pb-terminated surfaces. Figure 5.8(d) shows the adsorption of OAM ligands at Cs^+ and Pb^{2+} sites on the Cs-terminated and Pb-terminated surfaces respectively. The fist peak of the pair correlation is observed to lie beyond 0.35 nm for the Cs^+ sites and below 0.35 nm for the Pb^{2+}. This indicates that OAM ligands are adsorbed at Pb^{2+} sites of the Pb-terminated surface but not at Cs^+ sites of the Cs-terminated surface. Pb^{2+} sites have higher charge and hence, stronger electrostatic interactions with the ligands. From Figure 5.8(e), it is seen that OAM ligand are not adsorbed at Br^- sites, both for Cs-terminated and Pb-terminated surfaces. Finally, Figure 5.8(f) indicates that OAM ligand are adsorbed at V_{Br} both at the Cs-terminated and Pb-terminated surfaces.

We also examine details of ligand adsorption, when a combination of OLA and OAM^+ ligands is used in presence of hexane solvent. Figure 5.9 shows pair correlation functions for OLA and OAM^+ ligands at various sites on the Cs-terminated (left panel) and Pb-terminated (right panel) surfaces respectively. Here we observe from Figure 5.9(a) that OLA ligands are adsorbed at Cs^+ and Pb^{2+} sites on the Cs-terminated and Pb-terminated surfaces respectively. The peak observed for OLA at Pb^{2+} is higher than that for Cs^+ site. This indicates greater adsorption of OLA ligands at Pb^{2+} sites compared to Cs^+ sites. In Figure 5.9(b), the first peak of the pair correlation function lies beyond 0.35 nm, indicating that OLA ligands are not adsorbed at Br^- sites, both for the Cs-terminated and Pb-terminated surfaces. As seen from Figure 5.9(c), OLA ligands are also adsorbed at V_{Br} sites on the Cs-terminated and Pb-terminated facets. For the adsorption of OAM^+ ligands, it is observed from Figure 5.9(d) that the first peak of the pair correlation lies beyond 0.35 nm for both Cs^+ and Pb^{2+} sites. Thus, OAM^+ is not adsorbed at these sites as expected due to their similar charge. A

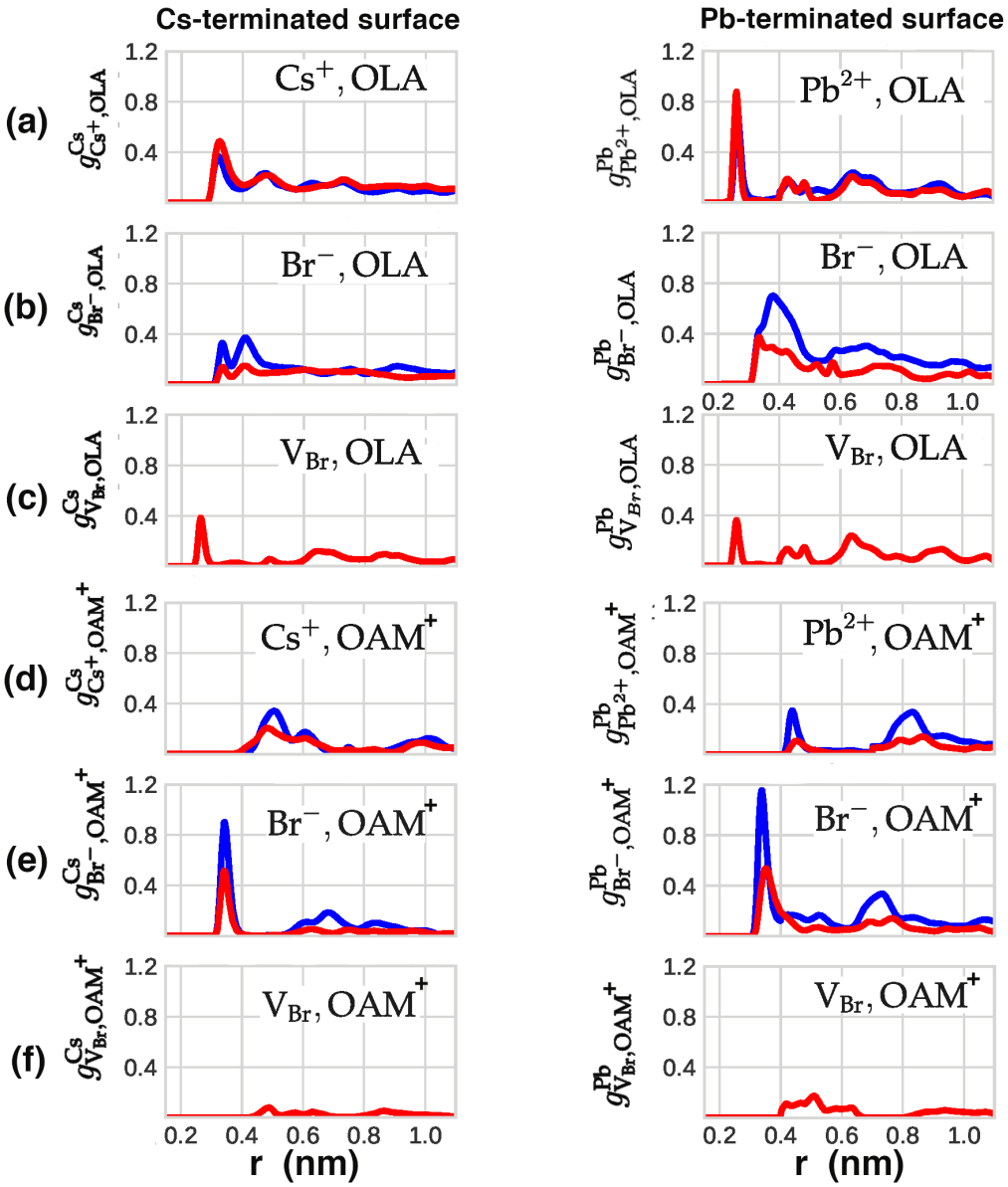

Figure 5.9: Pair correlation of OLA and OAM^+ ligands around different adsorption sites at Cs-terminated surface (left panel) and Pb-terminated surfaces (right panel). The red curves are for nanoparticle with Br vacancies while the blue lines are for nanoparticle with no vacancies.

strong first peak is observed within 0.35 nm separation for OAM^+ at Br^- sites for Cs-terminated and Pb-terminated surfaces as seen from Figure 5.9(e), indicating that OAM^+ ligands are adsorbed at Br^- sites on both surfaces. Also the blue curve is seen to lie above the red one, with a higher peak at the Pb-terminated surface compared to Cs-terminated surface. This indicates that OAM^+ adsorption

is favored at both terminations in the absence of V_{Br} sites, and the adsorption is greater for the Pb-terminated surface which has more Br^- sites compared to the Cs-terminated surface. Figure 5.9(f) shows no peaks for separation less than 0.35 nm, indicating that OAM^+ ligands are not adsorbed at V_{Br} sites for both the Cs-terminated and Pb-terminated surfaces.

For a more quantitative picture we calculate the ligand coverage given by the number of adsorbed ligands per nm^2 at each facet of the nanoparticle. The number of adsorbed ligand at each face is calculated by integrating the pair correlation from zero up to 0.35 nm as follows: $L_c^\alpha = \frac{1}{\text{Area}} \sum_A \int_0^{0.35} g_{A,B}^\alpha(r)dr$, where α = {Cs,Pb} specifies the facet termination, A = { Cs^+,Pb^{2+} ,Br^-,V_{Br} } is the adsorption site and and B = { OLA, OLA^-, OAM, OAM^+ } are ligand types. Table 5.3 shows the ligand coverage at various nanoparticle facets when the combination of OLA^- and OAM ligands is used in presence of hexane solvent. It is observed that for all facets the coverage by OLA^- ligands is greater than that of OAM ligands. This is due to the strong electrostatic interactions between OLA^- ligands and the metal cations at the surface. It is also observed that coverage at surfaces with V_{Br} is greater than that at surfaces with no V_{Br}. This is because vacancy sites have a net positive charge and tend to adsorb both OLA^- and OAM ligands, thereby increasing the overall ligand coverage. As expected the ligand coverage is maximum for the Pb terminated surface with Br vacancies due to the large charge of Pb^{2+} ions and the added contribution of the V_{Br}.

	L_c^α (ligands / nm^2)			
	Cs-surface with no V_{Br}	Cs-surface with V_{Br}	Pb-surface with no V_{Br}	Pb-surface with V_{Br}
OLA^- Ligands	1.06	1.95	1.74	2.20
OAM Ligands	0.49	0.81	1.22	1.76
Total	**1.55**	**2.76**	**2.96**	**3.97**

Table 5.3: Ligand coverage at different nanoparticle facets when OLA^- and OAM ligand combination is used in presence of hexane solvent.

	L_c^α (ligands / nm^2)			
	Cs-surface with no V_{Br}	Cs-surface with V_{Br}	Pb-surface with no V_{Br}	Pb-surface with V_{Br}
OLA Ligands	0.89	0.93	1.55	1.59
OAM^+ Ligands	0.59	0.36	1.48	0.32
Total	**1.48**	**1.28**	**3.03**	**1.91**

Table 5.4: Ligand coverage at different nanoparticle facets when OLA and OAM^+ ligand combination is used with hexane solvent.

When the ligand combination OLA and OAM^+ is used, the overall ligand coverage decreases compared to the OLA^-/OAM case (cf. Tables 5.3 and 5.4), especially for the case of nanoparticles having V_{Br}, which is the situation of interesst. This is due to the fact that OAM^+ ligands are repelled by the surface metallic cations. The highest coverage here is attained for the Pb-terminated surface with no Br vacancies. This is because the Pb-terminated surface has a larger number of Br^- sites which act as adsorption sites for the OAM^+ ligands. These observations are in agreement with previous observations from Figures 5.9(d) and (f) which show that OAM^+ ligands do not adsorb at cation and V_{Br} sites. All the observations suggest that adsorption of ligands is dominated by electrostatic interactions.

(d) Effects of solvent polarity:- To investigate the effects of solvent polarity on nanoparticle passivation, we use the ligand combination OLA^- and OAM. We carry out simulations of the nanoparticle with different solvents as shown in Table 5.2, and calculate the total ligand coverage at each facet. Figure 5.10(a) shows ligand coverage for the Cs-terminated and Pb-terminated facets of nanoparticle with and without V_{Br}, as a function of the solvent dielectric permittivity. It is observed that the ligand coverage at each facet decays as the solvent dielectric permittivity increases. This decay follows a power law with exponent $\sim$ -0.82. This exponent is close to linear dependence physically. The higher dielectric permittivity, reduces the strength of electrostatic interactions, which are known to

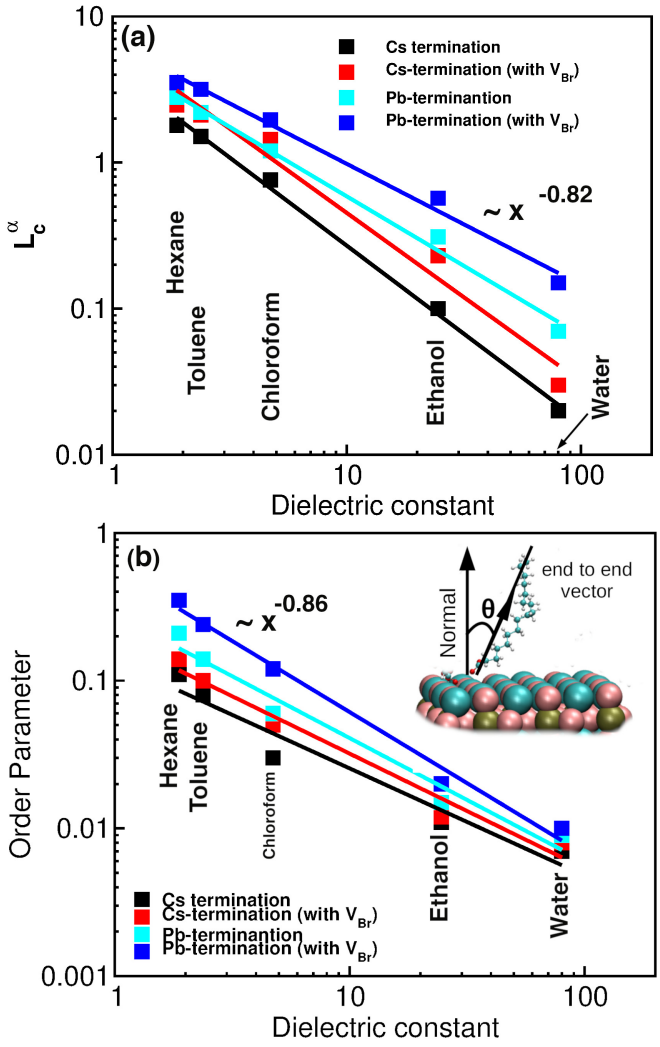

Figure 5.10: (a) Ligand coverage and at Cs-terminated and Pb-terminated facets for nanoparticle with and without Br vacancies, as a function of solvent dielectric permittivity. (b) Ligand orientation order parameter as a function of solvent dielectric permittivity. The inset shows how the ligand orientation angle with respect to the nanoparticle surface is determined.

be proportional to $\frac{1}{\epsilon_0}$, where ϵ_0 is the dielectric permittivity. This further confirms the role of electrostatics in ligand adsorption.

(e) Ligand orientation order:- We also examine the ordering of ligands at each of the nanoparticle facets, in different solvents via the nematic order parameter. $S = \frac{1}{2}\langle 3\cos^2(\theta) - 1\rangle$, where θ is the angle between the end-to-end vector of an adsorbed ligand molecule and the surface normal. The angled braces $\langle \cdots \rangle$ denote the average over all ligands adsorbed at the surface and over

multiple simulation frames in the equilibrated part of the trajectory. Figure 5.10(b) the order parameter of ligands at different nanoparticle surfaces as a function of solvent polarity. The ligand orientation is determined as shown in the inset. The order parameter is observed to decrease sharply with increasing solvent polarity. This decay is also observed to follow a power law with exponent ~ -0.86. This dependence is also close to a linear one, similar to that obtained for the ligand coverage. This similarity can be attributed to the fact that as the ligand coverage reduces with increasing solvent polarity, the adsorbed ligand molecules have more room for orientational fluctuations and hence become more disordered.

(f) Surface specificity: As remarked above, the adsorption of ligands on the nanoparticle is dominated by electrostatic interactions. A comparison of the ligand coverage at the Cs-terminated and Pb-terminated facets (see Table (5.3) and (5.4)), reveals that almost twice as much ligand is present at the Pb-terminated facet, compared to the Cs-termination, for all ligand combinations. We note that the Pb-terminated facet has double the number of Br^- adsorption sites compared to the Cs-termination. In addition, the larger charge of the Pb^{2+} ions at the Pb-terminated facet leads to stronger electrostatic interaction with the ligands compared to the Cs^+ ions at the Cs-terminated surface. Thus, the surface specific adsorption ligands at the Pb-terminated surface, can be attributed to these compositional differences of the facets.

5.3.2 Free energy profile of nanoparticle interaction from meta-dynamics

Next we investigate interactions between ligand dressed nanoparticles and attempt to rationalize the free energy profile of interaction between different facets, using knowledge of the ligand shell structure. We begin by looking at the free energy profiles for interaction between different facets of the nanoparticle

in hexane solvent, obtained via the metadynamics approach outlined in section 5.2.6. We denote by Cs – Pb, the interaction between the Cs terminated facet of one particle with the Pb terminated facet of the second particle, and likewise, Cs – Cs and Pb – Pb.

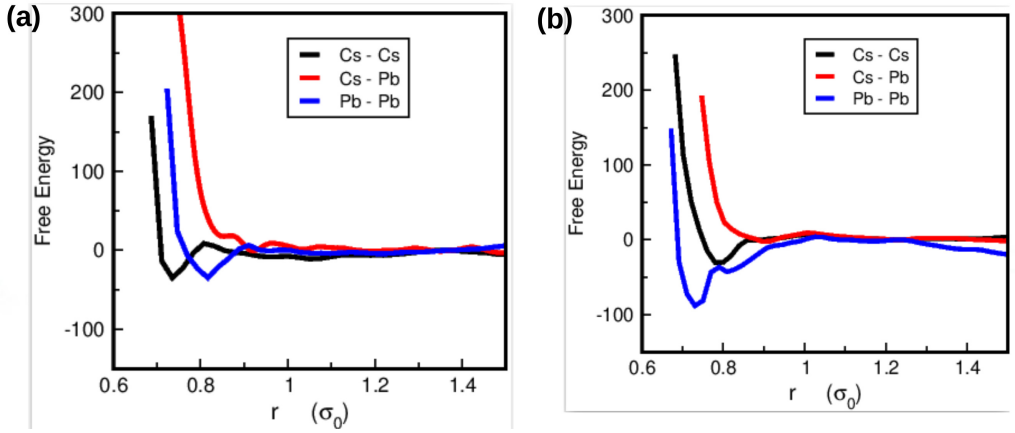

Figure 5.11: Free energy of interaction between different facets of nanoparticles (a) without Br vacancies and (b) with Br vacancies, in hexane solvent.

Figures 5.11 (a) and (b) show the free energy profile for Cs – Cs, Cs – Pb and Pb –Pb interactions, for nanoparticles with and without V_{Br} respectively. As observed from Figures 5.11 (a), for a nanoparticle with no vacancies, the Cs – Cs interactions become attractive for separations of $\sim 0.8\sigma_0$. Here, σ_0 is the diameter of the nanoparticle. Pb – Pb interactions also become attractive at separations of $\sim 0.9\sigma_0$, meanwhile Cs – Pb interactions do not show any such minima for all separations. For nanoparticle with Br vacancies at the surface, as shown in Figure 5.11(b), a minima is observed in the Cs – Cs interaction profile at a separation $\sim 0.8\sigma_0$, comparable to that observed for the no vacancy case. Likewise, a minima is also observed for the Pb – Pb interaction profile, at a smaller separation of $\sim 0.7\sigma_0$. The observed minima is deeper compared to the no-vacancy case indicating that the interaction between the facets becomes stronger. No minima is observed for the case of Cs – Pb interactions.

As observed from Figure 5.11(a) and (b), interactions between Pb-terminated

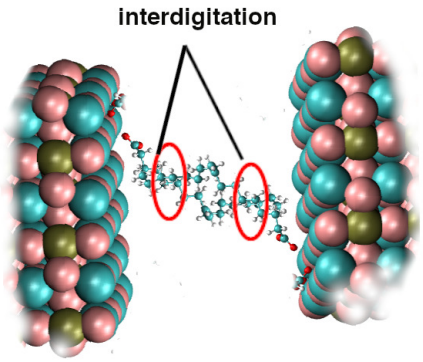

Figure 5.12: Ligand interdigitattion. The two ligand chains cross at a minimum of two points.

facets are the strongest. From single nanoparticle simulations, it has been observed that ligand coverage is also maximum at the Pb-terminated surface. This suggests that attractive interactions between the nanoparticle facets are mediated and stabilized by the ligands. To verify this, we investigated the interdigitation between ligands of the two nanoparticles when the separation between them is small. Two ligands adsorbed at separate surfaces are said to interdigitate if beads from one ligand chain lie at a separation of less than 0.3 nm from beads of the second ligand chain, for at least two points. This means that the two ligand chains cross each other at least twice, as illustrated in Figure 5.12. The fraction of interdigitated ligands between two interacting Pb – Pb facets at a separation of $0.8\sigma_0$ is found to be 0.87 for Pb –Pb interactions, 0.61 for the Cs – Cs interactions and 0.32 for Cs – Pb interaction. This is further confirmed by a contour plots of the normalized density for adsorbed ligands for Cs –Cs, Cs – Pb and Pb – Pb interacting facets, shown in Figure 5.13(a), (b) and (c) respectively. As expected, the ligand density in the region between the two nanoparticles is maximal when the Pb-terminated facets are facing each other. Thus, the stronger interaction between Pb – Pb facets can be attributed to the higher ligand density and interdigitation.

To investigate the influence of solvent polarity on the interaction of nanoparti-

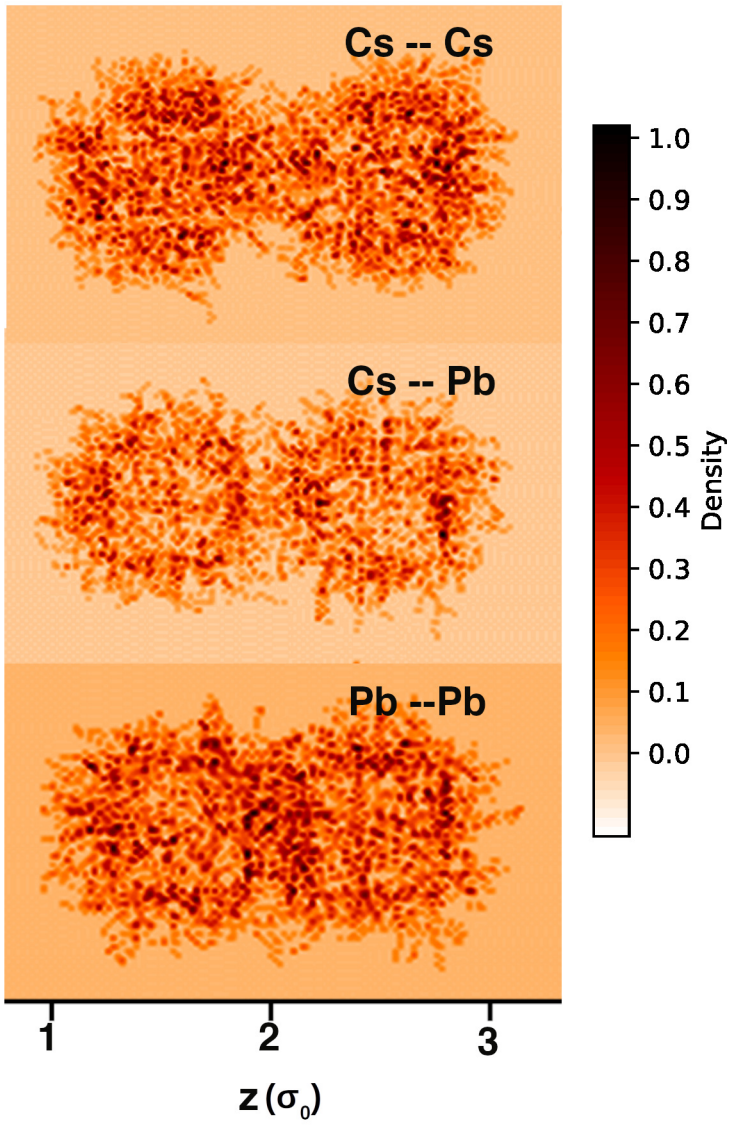

Figure 5.13: Contour plots of the normalized density of adsorbed ligands for interaction between (a) Cs–Cs, (b) Cs–Pb and (c) Pb–Pb facets, for nanoparticles with Br vacancies in presence of hexane, with the nanopartiles at a separation of $0.8\sigma_0$.

cles, we calculate the free energy profiles for interaction between the Pb vs Pb facets of nanoparticles in different solvents. Figure 5.14, shows the Pb – Pb interaction free energy profile for nanoparticles in different solvents. It is observed that the interactions are attractive in hexane solvent, and become repulsive as solvent polarity increases. This can be understood from earlier observations that increasing solvent polarity leads to a reduction in ligand adsorption and hence repulsive interaction between nanoparticles. This is in agreement with

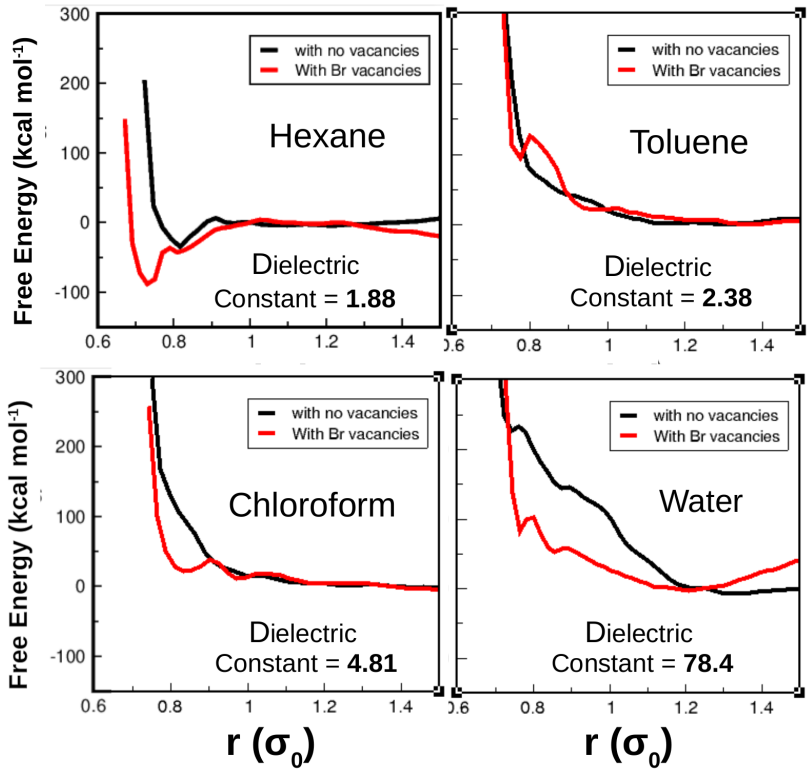

Figure 5.14: Free energy of interaction between two $PbBr_2$ terminated facets of nanoparticles in presence of different solvent with increasing polarity. The black curves are for nanoparticles without Br vacancies and and the red are for nanoparticles with Br vacancies at their surface.

our suggestion that the attractive interactions between NP facets are mediated by ligand interdigitation. In polar solvents competing interactions between ligands and solvent lead to desorption of ligand and repulsive interactions between the nanoparticles; meanwhile, in non-polar solvents a higher fraction of ligands is adsorbed at the nanoparticle surface, and interactions between nanoparticles are attractive.

5.4 Summary

We have presented all-atom MD simulation results for the adsorption of oleic acid and oleylamine ligands at the surfaces of $CsPbBr_3$ nanoparticles, in the presence of solvents with varying degrees of polarity. We have considered two nanoparticle

models, viz, one with and the other without Br vacancies at the surface. We find that the ligand adsorption process is dominated by electrostatic interactions. The total amount of adsorbed ligand when the OLA^-/OAM ligand combination is used, is greater compared to the OLA/OAM^+ combination. For both ligand combinations, we find that more ligands are adsorbed on nanoparticles having Br vacancies, compared to nanoparticles without Br vacancies. Calculation of the ligand coverage at each nanoparticle surface in the presence of different solvents also reveals that more ligands are adsorbed on the Pb-terminated surface, compared to the Cs-terminated surface, resulting in an asymmetric ligand shell. Such asymmetry of the ligand shell may be at the origin of directed interactions in colloidal nanoparticle suspensions, as has been suggested in Ref. [40]. The ligand coverage as well as ligand ordering at each facet decays with increasing solvent polarity, following a power law of exponent ~ 0.8, due to increased electrostatic shielding by the solvent. We also examine the free energy profile for interactions between different facets of two nanoparticles and its connection to ligand adsorption. It is found that for nanoparticles with Br vacancies and in the presence of hexane, the interaction between Pb-terminated facets, which have the highest number of bound ligands, is attractive. The interactions become repulsive as solvent polarity increases. For Cs – Cs facets, a similar trend is observed, meanwhile for Cs – Pb in hexane as well as in other solvents.

This study provides a microscopic picture and theoretical understanding of facet specific ligand adsorption that can give rise to directed self-assembly of colloidal $CsPbBr_3$ nanoparticles. From the calculated free energy profile, a coarse grained model which takes into account the asymmetric distribution of ligands on different nanoparticle facets, can be developed and used for probing directed self-assembly of nanoparticles.

References

[1] D. V. Talapin, J.-S. Lee, M. V. Kovalenko, E. V. Shevchenko, *Chemical reviews* **110**, 389 (2010).

[2] A. Hensley, W. M. Jacobs, W. B. Rogers, *Proceedings of the National Academy of Sciences* **119**, e2114050118 (2022).

[3] G. M. Barratt, *Pharmaceutical Science & Technology Today* **3**, 163 (2000).

[4] N. Tahsini, *et al.*, *Journal of the American Chemical Society* **144**, 1612 (2022).

[5] A. E. Salih, M. Elsherif, F. Alam, M. Chiesa, H. Butt, *Nanomaterials* **12**, 1486 (2022).

[6] S.-C. Chien, *et al.*, *The Journal of Physical Chemistry C* **121**, 4564 (2017).

[7] M. Imran, *et al.*, *Chemistry of Materials* **28**, 6450 (2016).

[8] R. Qu, *et al.*, *CrystEngComm* **22**, 1853 (2020).

[9] R. Grisorio, *et al.*, *Nanoscale* **11**, 986 (2019).

[10] S. Ullah, *et al.*, *Materials Advances* **2**, 646 (2021).

[11] Z. Peng, *et al.*, *Science China Materials* **64**, 2261 (2021).

[12] Y. Gao, *et al.*, *Advanced Materials* **30**, 1801805 (2018).

[13] X. Xiao, Y. Li, R.-J. Xie, *Nanoscale* **12**, 9231 (2020).

[14] M. Do, *et al.*, *Nanoscale* **11**, 17262 (2019).

[15] L. Protesescu, *et al.*, *Nano letters* **15**, 3692 (2015).

[16] C. Zhou, H. Lin, S. Lee, M. Chaaban, B. Ma, *Materials Research Letters* **6**, 552 (2018).

[17] Y. Chen, *et al.*, *Journal of the American Chemical Society* **142**, 6117 (2020).

[18] M. I. Bodnarchuk, *et al.*, *ACS energy letters* **4**, 63 (2018).

[19] J. Yin, *et al.*, *ACS nano* **15**, 17998 (2021).

[20] J. Kang, L.-W. Wang, *The journal of physical chemistry letters* **8**, 489 (2017).

[21] R.-I. Biega, L. Leppert, *Journal of Physics: Energy* **3**, 034017 (2021).

[22] S. Ten Brinck, F. Zaccaria, I. Infante, *ACS Energy Letters* **4**, 2739 (2019).

[23] J. Pan, *et al.*, *Angewandte Chemie International Edition* **58**, 16077 (2019).

[24] J. Qiu, W. Xue, W. Wang, Y. Li, *Dyes and Pigments* **198**, 109806 (2022).

[25] J. De Roo, *et al.*, *ACS nano* **10**, 2071 (2016).

[26] D. Quarta, *et al.*, *The journal of physical chemistry letters* **10**, 3715 (2019).

[27] S. Sun, D. Yuan, Y. Xu, A. Wang, Z. Deng, *ACS nano* **10**, 3648 (2016).

[28] X. Li, *et al.*, *Advanced Functional Materials* **26**, 2435 (2016).

[29] F. Bertolotti, *et al.*, *ACS nano* **11**, 3819 (2017).

[30] G. Kresse, J. Furthmüller, *Physical review B* **54**, 11169 (1996).

[31] G. Kresse, *Journal of Non-Crystalline Solids* **192**, 222 (1995).

[32] P. E. Blöchl, *Physical review B* **50**, 17953 (1994).

[33] G. Kresse, D. Joubert, *Physical review b* **59**, 1758 (1999).

[34] J. P. Perdew, K. Burke, M. Ernzerhof, *Physical review letters* **77**, 3865 (1996).

[35] J. Shim, E.-K. Lee, Y. Lee, R. M. Nieminen, *Physical Review B* **71**, 035206 (2005).

[36] S. Kim, *et al.*, *Nucleic acids research* **44**, D1202 (2016).

[37] L. Martínez, R. Andrade, E. G. Birgin, J. M. Martínez, *Journal of computational chemistry* **30**, 2157 (2009).

[38] M. Mirbagheri, D. Mohebbi-Kalhori, N. Jirofti, *International Journal of Basic Science in Medicine* **2**, 58 (2017).

[39] G. A. Jeffrey, G. A. Jeffrey, *An introduction to hydrogen bonding*, vol. 12 (Oxford university press New York, 1997).

[40] H. O. Yadav, *Soft Matter* **16**, 9262 (2020).

Chapter 6 Outlook

In this thesis, employing primarily different classical simulation techniques, we have provided an understanding of the microscopic interactions and their impact on various properties at the interfaces of nano-confined fluids and the confining surfaces, as well as nanoparticle interfaces with ligands and solvent.

In this chapter, we present the possible outlook of our work considering the three topics studied in this thesis:

(a) Nonlinear rheology of asymmetrically nanoconfined fluid films

As shown in chapter 3, fluids confined in asymmetric nano-channels exhibit a rich phase behavior and viscoelastic response which is driven by channel asymmetry. The extension of this study to include non-linear transport behavior under strong external perturbations naturally arises. Non-linear responses such as shear thinning and shear thickening are prevalent in nanoscale systems [1], as microscopic fluctuations typically become stronger. Understanding the origin of nonlinear effects is, therefore, important for the design and manipulation of nanofluidic devices, and for other nanofluidic applications such as nano-lubrication etc. Recent experiments, notably [1] and [2] have probed the non-linear rheological properties of fluids in symmetric nano-confinement, while very few studies [3] exist for asymmetrically confined fluids.

Nonlinear transport coefficients may be computed via direct none-equilibrium molecular simulations in which the boundary conditions or the equations of motion are altered, in order to drive a current through the system [4, 5]. However, connecting the computed responses to molecular degrees of freedom is challenging. For example, expressing local stress values in terms of density, shear rate and other quantities remains an open problem for confined fluids. Non-equilibrium molecular dynamics studies on such systems may contribute insights to solving some of these open problems associated with confined fluids on the nanoscale.

(b) Asymmetric nanochannels for drug delivery

In chapter 4 of this thesis we have shown that asymmetric confinement of water between hydrophobic and hydrophilic surfaces results in dynamics heterogeneity of confined water, and enhanced diffusion of guest molecules in the confined water. We have also demonstrated that this behavior is not specific to the STO-graphene system, but is true for any hydrophobic-hydrophilic nanochannel. Based on these observations, we have suggested that such hydrophobic-hydrophilic nanochannels can be exploited in the design of implantable drug delivery devices. We remark that while TiO_2 is bio-compatible, graphene is not and so cannot be used for drug delivery. However, any bio-compatible membrane can be used in place. Recently, layer-by-layer assembled thin films of nanocrystalline cellulose have been proposed for use in drug delivery applications [6]. It will therefore be interesting to study the dynamics of small drug molecules such as cisplatin [7] in nanochannels formed by formed by cellulose film and metal oxide surface.

(c) Self assembly of colloidal $CsPbBr_3$ nanoparticles

As discussed in Chapter 5, self-assembly of colloidal nanoparticles in solution provides an efficient route for achieving complex and robust nanoparticle superlattices like nanowires and nanoplates. From our study, we have presented evidence of preferential adsorption of ligands to the Pb-terminated facet of $CsPbBr_3$

nanoparticles. We find that this results in stronger attractive interactions of the Pb-terminated facet with the Pb-terminated facet of other nanoparticles, driven by ligand interdigitation. This kind of preferential interactions can give rise to directed self-assembly of the nanoparticles. So far we have obtained free energy profiles for the interaction between different facets of the nanoparticles. These show that the interaction potential for the nanoparticles is highly anisotropic. As a continuation of the present study, the investigation of the possibility of directed self-assembly in this system should be carried out.

Modeling the interaction between many nanoparticles is computationally demanding. Hence, in order to improve computational efficiency and times scales of the simulation, a coarse-grained model of the system may be useful. An example of a coarse grained model with anisotropic interaction potential that has been used for modeling interactions of faceted nanoparticles, is the patchy colloid model. In this model, the nanoparticle is represented by a sphere with attractive or "sticky" patches on it [8, 9], with each patch representing a facet of the nanoparticle. Our model can provide both the the size of the patches and their interaction energy to achieve the desired interaction profile of the patchy colloidal model.

References

[1] B. Kim, *et al.*, *Proceedings of the National Academy of Sciences* **112**, 15619 (2015).

[2] E. Riedo, *et al.*, *Physical review letters* **100**, 106102 (2008).

[3] X. Zhang, Y. Zhu, S. Granick, *Science* **295**, 663 (2002).

[4] Y. Kang, S. Lü, P. Ren, B. Huo, M. Long, *Biophysical journal* **102**, 112 (2012).

[5] W. G. Hoover, C. G. Hoover, *Condensed Matter Physics* (2005).

[6] V. Mohanta, G. Madras, S. Patil, *ACS Applied Materials & Interfaces* **6**, 20093 (2014).

[7] E. E. Trimmer, J. M. Essigmann, *Essays in biochemistry* **34**, 191 (1999).

[8] E. Bianchi, R. Blaak, C. N. Likos, *Physical Chemistry Chemical Physics* **13**, 6397 (2011).

[9] N. Kern, D. Frenkel, *The Journal of chemical physics* **118**, 9882 (2003).